THESIS

EVALUATING COVARIANCE-BASED GEOSTATISTICAL METHODS WITH BED-SCALE OUTCROP STATISTICS CONDITIONING FOR REPRODUCTION OF INTRA-POINT BAR FACIES ARCHITECTURE, CRETACEOUS HORSESHOE CANYON FORMATION, ALBERTA, CANADA

Submitted by

Andrew Louis McCarthy

Department of Geosciences

In partial fulfillment of requirements

For the Degree of Master of Science

Colorado State University

Fort Collins, Colorado

Summer 2022

Master's Committee:

Advisor: Lisa Stright

Michael Ronayne
Ryan Bailey

ABSTRACT

EVALUATING COVARIANCE-BASED GEOSTATISTICAL METHODS WITH BED-SCALE OUTCROP STATISTICS CONDITIONING FOR REPRODUCTION OF INTRA-POINT BAR FACIES ARCHITECTURE, CRETACEOUS HORSESHOE CANYON FORMATION, ALBERTA, CANADA

Geostatistical characterization of petroleum reservoirs typically suffers from problems of sparse data, and modelers often draw key parameters from analogous outcrop, numerical, and experimental studies to improve predictions. While quantitative information (bed-scale statistical distributions) from outcrop studies is available, translating the data from outcrop to models and generating geologically-realistic realizations with available geostatistical algorithms is often problematic. The overarching goal of this thesis is to test the capacity of covariance-based geostatistical methods to reproduce intra-point bar facies architecture while guiding those algorithms with bed-scale outcrop statistics from the Late Cretaceous Horseshoe Canyon Formation in southeastern Alberta. First, general facies architecture reproduction is tested with 2- and 3-facies synthetic and outcrop-based experiments with variable hard data, soft data weight, and soft data reliability. Next, 3-D sector models compare performance of different geostatistical simulation methods: sequential / co-sequential indicator, plurigaussian, and nested truncated gaussian. Findings show that despite integration of outcrop statistics, all conventional covariance-based geostatistical algorithms struggle to reproduce complex facies architecture that is observed in outcrop. Specifically, problems arise with: 1) low-proportion facies and 2) a weak

statistical relationship between hard data (measured sections) and soft data (probability models). Nested modeling partially mitigates low-proportion issues and performs better as a result.

ACKNOWLEDGEMENTS

This study would not have been possible without the foundation of sedimentological work by Paul Durkin. I thank him, along with his advisor Stephen Hubbard, for collecting the data. My advisor, Lisa Stright, contributed heavily to the initial modeling. I thank her for the opportunity to continue on with this work. I would like to thank my committee members, Mike Ronayne and Ryan Bailey for their time, edits, and invaluable guidance.

Schlumberger and Geovariances were generous to supply software to facilitate this modeling effort. My fellow Geomodeling Research Group students, Adam Nielson, Casey Meirovitz, Noah Vento, Andrew Ruetten, and Theresa Langenkamp were generous to supply their insight, feedback, and support throughout this process. My research time at Colorado State University was funded by the Edward M. Warner Graduate Research Assistant Fund Scholarship, a Geoscience Department teaching assistantship, and research assistantships supported in part by the Rocks2Models consortium. Support for Rocks2Models projects comes from ConocoPhillips Corporation, Royal Dutch Shell PLC, and Hess Corporation. Additionally, fieldwork for this study was supported by ConocoPhillips Canada and CNOOC Nexen Inc. Field assistance was provided by Dustin Bauer, Ross Kukulski, Sean Fletcher, Ben Daniels, Aaron Reimchen and Tore Klausen.

I made so many good and strong friends along the way here; this is truly the thing I value most from my time in Colorado. Finally, I would like to thank my family. Thank you, to my parents and brothers for guiding and cheering me from afar. Thank you, to my wife, Annie, for following me here, and then seeing it all the way through with me.

TABLE OF CONTENTS

CHAPTER 1: INTRODUCTION

Geostatistical models of petroleum reservoirs guide well planning and risk assessment decisions in hydrocarbon exploration and development (Keogh et al., 2007). These models integrate disparate data types of varying resolution, sampling, and error into one framework and are used to explore reservoir uncertainty (Deutsch, 2006b; Pyrcz and Deutsch, 2014). Furthermore, they are easily visualized as three-dimensional (3-D) numerical representations of reservoir properties and quickly modified, which makes them suitable to cross-disciplinary and team work.

Geostatistical characterization of petroleum reservoirs typically suffers from problems of sparse data, and modelers often draw key parameters from analogous outcrop, numerical, and experimental studies to improve predictions (Dubrule and Damsleth, 2001; Pyrcz and Deutsch, 2014). Historically, reservoir characterization and modeling focused on larger, seismically-resolvable architectural elements (i.e., geobody- to reservoir-scale) with only limited regard for bed-scale heterogeneities (Keogh et al., 2007; Colombera et al., 2013; Hassanpour et al., 2013; Yin, 2013). Bed-scale facies heterogeneity can impact fluid flow and, in many cases, it is critical to include this impact in flow simulations used for prediction of fluid flow pathways and flow performance especially for heterolithic and / or high-viscosity reservoirs (Deschamps et al., 2012; Martinius et al., 2017; Meirovitz et al., 2021). However, flow simulation is generally performed on more coarsely-gridded (i.e., upscaled) models without regard for this bed-scale heterogeneity, so the impact is often unknown (Deschamps et al., 2012; Martinius et al., 2017; Meirovitz et al., 2021). More studies incorporating bed-scale outcrop data into bed- to geobody-scale models are needed to characterize flow behavior so that its impact can be accounted for in

coarsely-gridded flow models (Howell et al., 2014). Unfortunately, incorporating bed-scale heterogeneity in models is challenging, and, although quantitative information (bed-scale statistical distributions) from outcrop studies is available (See: 2A.2 Geostatistical Modeling from Outcrops), the efficacy of translating the data from outcrop to models and generating geologically-realistic models with available geostatistical algorithms is problematic (Ma, 2009).

The focus of this study is a fluvial point bar deposits of the Late Cretaceous Horseshoe Canyon Formation in southeastern Alberta (Durkin et al., 2015). Data from Durkin et al. (2015) are utilized in a quantitative outcrop modeling study to test the efficacy of incorporating bed-scale outcrop statistics in subsurface models. The overarching goal of this thesis is to test the capacity of covariance-based geostatistical methods to reproduce intra-point bar facies architecture by guiding those algorithms with outcrop statistics. The primary objectives are to:

1) evaluate the accuracy of facies reproduction for a 2-facies experiment (Part 1a) and 3-facies experiment (Part 1b) with variable hard data, soft data weight, and soft data reliability,
2) use a sector model to test sequential / co-sequential indicator simulation (Part 2a) and plurigaussian simulation (Part 2b) and compare results with nested TGS from Durkin (Durkin, 2016).

CHAPTER 2A: LITERATURE REVIEW

2A.1 Geostatistical Facies Modeling

Conventional covariance-based geostatistics is rooted in the intuitive idea that physical properties exhibit spatial correlation: closely spaced points will be more alike, while points spaced farther apart will be less alike. This spatial correlation is quantified through variography, and used to estimate properties at unsampled locations with kriging, a technique adapted from linear regression. Kriging was formalized as the "best unbiased linear estimator" of spatial data in the 1960s and 1970s via theory of spatially regionalized variables distributed by random functions (Krige, 1951; Matheron, 1963, 1973). Conditional stochastic simulation based around kriging estimates soon followed; modern methods were developed in the late 1980s and early 1990s, particularly sequential methods (Alabert, 1987; Journel and Alabert, 1989; Goovaerts, 1997; Deutsch and Journel, 1998) and related truncated gaussian field methods (Matheron et al., 1987; Galli et al., 1994).

All of these methods are easily conditioned to existing hard data (e.g., wireline logs and core data), readily incorporate soft data (e.g., seismic and production data) as secondary conditioning, and are adopted widely in reservoir facies modeling workflows (Xu et al., 1992; Journel, 1999; Dubrule and Damsleth, 2001; Yao, 2002; Keogh et al., 2007). However, covariance-based geostatistical methods (also referred to as variogram-based, kriging-based, or two-point) are only guaranteed to reproduce spatial correlations and input distributions or proportions, and, in cases, order of transition between categorical data types. These methods poorly reproduce complex patterns (e.g. curvilinear channel features or explicit stacking arrangements) due to the essential limitations of an underlying spatial correlation models based

on covariance between two points (Strebelle, 2002; Caers and Zhang, 2004; Klise et al., 2009). This problem is specifically addressed with multiple-point geostatistics (MPS). Instead of drawing on an underlying spatial correlation model, MPS leverages patterns from a training image (TI) and reproduces them in output realizations. The TI comprises geological properties in similar spatial arrangement to the model subject (Mirowski et al., 2009). While first theoretically addressed in the early 1990s (Guardino and Srivastava, 1993), computational challenges delayed practical adoption of MPS until the early 2000s (Strebelle, 2002).

MPS would appear better-suited for detailed outcrop modeling, where architectural reproduction is paramount. However, TIs exert strong character on realizations and must be selected carefully (Caers and Zhang, 2004). While there are methods to screen TIs for their statistical suitability for a given dataset, geologic expertise is still required for selection (Boisvert et al., 2007, 2010). In this sense multiple-point methods may require as much effort and experience to apply judiciously and effectively as covariance-based methods. Furthermore, while the limitations of covariance-based architectural reproduction are well-understood and easily observed, the appropriateness of a given TI is potentially quite subjective. Additionally, most TIs are developed for geobody and reservoir-scale applications and few examples exist at bed-scale (Pyrcz et al., 2008).

2A.2 Geostatistical Modeling from Outcrops

Outcrop studies may inform field-scale models with bed-scale information not observable in subsurface data. However, transforming outcrop observations into useful modeling data is hindered by limitations in geostatistical methods where interpolation or simulation with sparse data produces statistically correct, but unrealistic looking models.

A growing number of outcrop studies provide more quantitative data that can be incorporated into outcrop geostatistical models. These sedimentological and stratigraphic characterizations, often utilizing photogrammetry, differential Global Positioning System (dGPS), and / or light detection and ranging (LIDAR), precisely record the position and spatial extent of sedimentary data (e.g., facies, grainsize, and net:gross ratios) for both geobodies and bedding (Pringle et al., 2004; Bellian et al., 2005; Enge et al., 2007; Pranter et al., 2007; Deschamps et al., 2012; Purkis et al., 2012). This quantitative sedimentologic and stratigraphic information is increasingly incorporated directly into outcrop modeling studies. However, integrating quantitative outcrop data into subsurface modeling workflows remains challenging, especially when trying to capture geological complexity and realism at the bed-scale.

Modeling heterogeneous deposits at bed-scale introduces additional challenges in both honoring input statistics and generating a realistic model that captures visual observations at the outcrop. Practical limitations prevent exhaustive measurements of 3-D volumes of rock at any scale comparable to oil and gas well-spacing, which, at the smallest, would be meters thick and hectares wide (Clark et al., 1944; Tucker et al., 1998; Pranter and Sommer, 2011). Even excellent outcrop exposures still amount to a series of two-dimensional slices through a reservoir analog (Howell et al., 2014). While outcrop data (e.g., measured sections, photopans, LIDAR, etc.) can be supplemented with outcrop cores and geophysical surveys (e.g., ground-penetrating radar (Pringle et al., 2004) or seismic), if that outcrop is to serve as a fully-representative 3-D analog, properties must be estimated or stimulated between measured data. Historically this is achieved with a combination of deterministic and stochastic methods depending on the research question at hand. Purely deterministic methods (i.e., not estimation, but deliberate and interpretive “geologic” placement of facies within the model) are employed to compare highly-

specific facies architecture scenarios (Pranter et al., 2007). For less restrictive cases, subsections of the model may be interpreted prematurely to guide stochastic realizations (Deschamps et al., 2012). Typically, key stratigraphic surfaces are deterministically emplaced to demarcate zones with similar parameters, and facies are simulated stochastically within those zones where outcrop is not preserved (Pringle et al., 2004; Bellian et al., 2005; Enge et al., 2007; Purkis et al., 2012).

Thus, outcrop models themselves carry a degree of uncertainty and / or assumption, which is controlled in part by the modeling algorithm. Algorithms can be ranked by their ability to reproduce outcrop characteristics in order to minimize the emergent impacts of inherent uncertainties and required assumptions. Model realizations accurate to their parent outcrops will serve as better reservoir analogs than inaccurate or imprecise ones. This holds whether there is a suite of outcrop statistics to reproduce, or more general depositional conceptual model.

2A.3 Fluvial Point Bar Depositional Environment

Observations from modern and ancient river systems reveal that point bar sediments categorically fine-upward; as the bar form grows it restricts channel flow over its top leading to successively lower-energy, finer-grained deposition (Allen, 1970; Thomas et al., 1987). However, this simple description belies architectural complexity: episodic changes to stream state may cause significant intra-point bar erosion and subsequent rotation of bar accretion direction (Brice, 1974).

Detailed outcrop study (Durkin et al., 2015) shows these intra-point bar erosional surfaces dominate overall point bar migration patterns, but that intra-package sedimentation is internally complex. Steeply dipping major erosional surfaces truncate prior deposition and often coincide with significant changes to the point bar migration direction (up to 50°). Sigmoidal lateral accretion packages (LAP) deposit between these erosional surfaces, where each LAP

contains conformable beds of comparable dip magnitude and dip direction. The new stream flow regime governs internal heterogeneity of each LAP. This tiered and manifold heterogeneity makes point bars ideal for evaluating a geostatistical method's capacity to reproduce complex facies architecture. The study supplies strong outcrop control, and major surfaces are well-defined. Investigative focus is constrained to modeling LAP internal architecture and inferring how that architecture impacts flow within and between LAPs.

CHAPTER 2B: GEOSTATISCAL MODELING METHODS REVIEW

A major objective of this study is to investigate the ability of geostatistical methods to incorporate statistics from outcrop analog data and to generate models that capture qualitative geologic character of those outcrops. Specifically, this research focuses on reproducing realistic internal point bar architecture. As such, some fundamental building blocks of geostatistics employed in this study are reviewed in this section: 1) variograms, 2) kriging, 3) soft data, and 4) simulation.

2B.1 Variograms

Variograms serve as the chief correlation function input for covariance-based geostatistics, where a variogram is defined as the series of expected differences of two values separated by some incremental distance (Isaaks and Srivastava, 1989). For a given random function Z of a known mean and variance, set of locations, $\mathbf{u}$, and incrementally-increasing distance vector, $\mathbf{h}$ ("lag"), the variogram is defined as:

$$2\gamma(\mathbf{h}) = Var[Y(\mathbf{u}) - Y(\mathbf{u} + \mathbf{h})] = E\{[Y(\mathbf{u}) - Y(\mathbf{u} + \mathbf{h})]^2\} \qquad (Eq. 2.1)$$

The variogram measures how data becomes more dissimilar as distance between points increases and can be related to changes in covariance over those same distances (Gringarten and Deutsch, 2001). The covariance at $\mathbf{h = 0}$, or $C(\mathbf{0})$, is the sample variance, which leads to the definition :

$$\gamma(\mathbf{h}) = C(\mathbf{0}) - C(\mathbf{h})$$
$$\text{or}$$
$$C(\mathbf{h}) = C(\mathbf{0}) - \gamma(\boldsymbol{h}) \qquad (Eq. 2.2)$$

For cases of dense data, variogram interpretation includes: (1) calculating an experimental variogram with a particular lag distance and specified search ellipse to consider

spatial anisotropy and (2) fitting a variogram model to the experimental variogram points. Licit variogram models comprise a series of positive definite functions, each composed of a sill (γ value where dissimilarity stops increasing; theoretically the variance) and range (lag distance where the function reaches the sill). They yield a γ for any lag distance and direction. Where data is sparse, sample experimental variograms may be noisy or unreliable, and variogram models may be inferred based on geologic knowledge.

2B.1.1 Indicator Formalism and Indicator Variograms

Variograms were initially developed to work with parametric data and thus continuous variables. Covariance-based geostatistics of non-parametric data (i.e., continuous variables divided by thresholds or, as relevant to this study, categorical variables) relies on indicator formalism: each category is binary-coded as present or absent at known data locations.

For K mutually exclusive (i.e., $\mathbf{u}$ belong to only one category at each location) categories z_k, k = 1, …, K:

$$I(\mathbf{u}_\alpha;\, z_k) = \begin{cases} 1, & \text{if indicator } k \text{ is present at } \mathbf{u}_\alpha \\ 0, & \text{otherwise} \end{cases} \qquad (Eq.\,2.3)$$

The mean of the indicators for each category is therefore the same as global proportion of hard data in that category. Indicator variograms are calculated normally with the indicator-transformed values: one variogram for each category. The indicator variogram shows the increasing probability that two locations do not belong to the same category as a function of distance (Beucher and Renard, 2016). It is worth noting that only two variogram models are mathematically licit as indicator variogram models: spherical and exponential (Dubrule, 2017).

2B.1.2 Cross Variograms

Variogram theory further extends to evaluate spatial "cross-covariance" between two different regionalized variables with cross-variograms. For a suite of categories, each category

can be evaluated in the context of each other category. Indicator cross-variograms capture the distance over which one indicator will transition to another particular indicator and whether that transition is abrupt or smooth (Beucher and Renard, 2016). While it is theoretically desirable to fit cross-variograms models from experimental data to model the joint spatial relationship (i.e. full co-regionalization modeling), it is extremely difficult with sparse data and requires significant interpretation (Goovaerts, 1997). Theoretical simplifications of the cross-spatial relationship were developed to handle this problem (e.g., Markov-Bayes models, Bayesian updating, locally varying means, etc.) (Hua Zhu and Journel, 1993; Doyen et al., 1994; Deutsch, 2006a). These methods make assumptions about the inherent proportionality of the hard data covariance and joint covariance to enables joint covariance modeling of the hard and soft data together.

2B.2 Kriging

All covariance-based geostatistics has kriging at its core. Kriging is a linear estimator that leverages spatial covariance from a variogram model to estimate values throughout a field such that error is minimized and unbiased. At each unknown location, **u**, the true value is estimated from the weighted linear combination of the sample data spatial covariance by solving a system of equations related to two-point covariances and inverting for weights. This matrix inversion step, in part, necessitates that licit variogram models are positive definite (See: 2B.1 Variograms). If they are not, the matrices may not invert.

Kriging comes in several variants, e.g.: Simple Kriging (SK; where the mean is assumed), Ordinary Kriging (OK; where the mean is unknown), and Universal Kriging (where a local trend is employed). Kriging works for parametric data and indicator-transformed non-parametric data (i.e., indicator kriging or IK). For IK, separate indicator variogram models for

each indicator are often supplied as inputs (full IK), but a simplified approach (median IK) reduces compute times assuming that each indicator variogram model is proportional to a single, common model (e.g., the weighted average of each indicator variogram). With ample computing power, full IK is preferred because it allows more specific variogram modeling for each indicator. Kriging can also incorporate secondary data, or soft data, in addition to hard data with a method called co-kriging (See: 2B.3 Soft Data and Probability Models).

Furthermore, estimates from kriging can be leveraged in stochastic simulation. Each estimated value is used to build a local probability distribution function. Simulation values are drawn randomly from these functions. Many equiprobable realizations that honor the input parameters can be generated in this fashion. Unlike estimated fields, which are locally accurate, simulated fields are globally accurate.

A full accounting of the benefits and downsides of different kriging styles is beyond the scope of this study, but some particular problems with OK are worth mentioning as they relate to co-kriging and sequential simulation algorithms. OK may be preferrable to SK because it does not require an assumed mean as input and does not hold that mean constant throughout the model. Instead, OK allows the unknown mean to vary locally. OK is also able to capture any trends in the data that exists by estimating a local varying mean. However, when co-kriging with indicators, OK necessitates that soft data weights sum to zero, which means some soft data weights are negative causing negative estimates (i.e., order relation deviations). Additionally, co-kriging with OK causes soft data weights to be small and exert limited influence (Goovaerts, 1994, 1997). For sequential simulations: (1) SK is theoretically necessary to reproduce the sample cumulative distribution function and variogram and (2) OK has a tendency to spread hard

data and previously-simulated values beyond their proper range of influence. (Deutsch and Journel, 1998; Deutsch, 2006a; Pyrcz and Deutsch, 2014).

2B.3 Soft Data and Probability Models

Sparse hard data can be supplemented with soft data to guide geostatistics in the form of prior local probability information that is incorporated into estimates. Soft data is often incorporated directly into the kriging step in a process called co-kriging. Remote sensing data (e.g., seismic reflection and ground penetrating radar surveys) is a common soft data source. While this information is generally lower-resolution than hard data and an indirect measure of the property of interest, it is generally areally extensive, if not exhaustive to the area of modeling interest. Far more accurate predictions are possible when sparse hard data is augmented with ubiquitous soft data.

For reservoir facies modeling, inverse methods are typically used to convert seismic reflectivity to acoustic impedance (Russell, 1988; Yilmaz, 2001). The resulting inverse model is calibrated to collocated wellbore facies data to generate local facies probabilities for the entire acoustic impedance volume. The strength of the calibration between probability volumes and true facies occurrence is never perfect due to the nature and resulting resolution of remotely sensed data; facies may be poorly distinguished in soft data. This leaves the practitioner with a modeling decision of how to favor soft data against hard data given their imperfect relationship. Practitioners often have several options for a given modeling algorithm (e.g., full co-regionalization modeling via cross-variograms, Markov-Bayes models, locally varying means, Bayesian updating, etc.) (Deutsch, 2006a).

2B.4 Sequential Indicator Simulation and Co-Sequential Indicator Simulation

Sequential Indicator Simulation (SIS) is a covariance-based sequential simulation method built to work with non-parametric data in indicator space. This makes it particularly suitable for facies simulation (Journel and Alabert, 1989; Deutsch and Journel, 1998). Spatial correlation is supplied with indicator variograms. Hard data is translated to the grid, and a random path through unknown locations is generated. At each location, the algorithm generates a local conditional indicator probability distribution based on surrounding hard data and previously simulated values with IK. Then it draws randomly from that distribution to assign a facies, moving to all locations until each has a facies value. Altering a random number seed changes both the random path and facies drawing. Many equiprobable results may be generated in this fashion.

It is worth noting that sequential indicator methods have an inherent realization noise problem. Realizations often exhibit geologically-unrealistic short-scale variations in the form of isolated facies clusters from one to a few cells in size. This is due to their categorical and sequential nature paired, and is compounded by statistical fluctuations found in stochastic simulation. As a result, smoothing (or "image cleaning") is so often incorporated directly into modeling workflows (Deutsch, 2006a). However, while smoothing may remove isolated, spurious pixels it also may smear out the very heterogeneities and details a modeler wishes to explore.

Co-Sequential Indicator Simulation (COSIS) expands SIS to incorporate soft data. The process is the same as with SIS, except that local conditional probability distributions are generated with indicator co-kriging. For each facies, in theory, the spatial covariance of the particular facies' soft data, hard data, and the cross-covariance of the hard data and soft data

together are each required to perform co-kriging at every unknown location. However, sparse data, especially for low-proportion facies, often precludes fitting of cross-covariance models from experimental cross-variograms. Therefore, the cross-covariance between soft and hard data is often generalized; one widely-implemented methods is the Markov-Bayes Model of Co-regionalization.

2B.4.1 Markov-Bayes Model of Co-regionalization

The Markov-Bayes Model of Co-regionalization assumes that, for a given indicator, spatial covariance of soft data is intrinsically related to that of the hard data. As such, their cross-covariance can be expressed in terms of the auto-covariance of both the soft and hard data (Hua Zhu and Journel, 1993; Almeida and Journel, 1994; Journel, 1999). For each indicator, k:

$$\begin{aligned} C_{\mathrm{IS}}(\mathbf{u};k) &= B \cdot C_{\mathrm{I}}(\mathbf{h};k) \\ C_{\mathrm{S}}(\mathbf{u};k) &= B^2 \cdot C_{\mathrm{I}}(\mathbf{h};k), \text{for all } \mathbf{h} > 0 \\ &= |B| \cdot C_{\mathrm{I}}(\mathbf{h};k), \text{for all } \mathbf{h} = 0 \end{aligned} \qquad (Eq.\,2.4)$$

where $C_{\mathrm{I}}(\mathbf{h}; k)$ is the hard data auto-covariance, $C_{\mathrm{S}}(\mathbf{h}; k)$ is the soft data auto-covariance, and $C_{\mathrm{IS}}(\mathbf{h}; k)$ is their cross-covariance. B are calibration coefficients between the hard data and soft data. B values are expressed as auto-covariance ratios by manipulating the above equations, or calculated from the indicator and soft sample data directly:

$$B = E\{P(k|soft(\mathbf{u})) \mid I(\mathbf{u};\, k) = 1\} - E\{P(k|soft(\mathbf{u})) \mid I(\mathbf{u};\, k) = 0\} \qquad (Eq.\,2.5)$$

where $k|soft(\mathbf{u})$ is the k, soft data value and $I(\mathbf{u}; k)$ is the k, indicator value. In other words, the expected value of soft data where indicator, k, occurs less the expected value of soft data where indicator, k, does not occur at estimation locations, $\mathbf{u}$ (Hua Zhu and Journel, 1993).

B values, which range from -1 to 1, indicate how well soft data probabilities differentiate their respective indicator (i.e., the reliability of the soft data in guiding indicator predictions). If B is close to 1, soft data values reliably predict their given indicator; the indicator is distinct in

the soft data. If B is close to 0, soft data values weakly predict their given indicator; the indicator is indistinct in the soft data. Negative B values indicate an inverse relationship between soft and hard data and, in all likelihood, user error. B values acting as algorithm inputs, which are differentiated in this study as B_i (where i denotes arbitrary user "input"), control COSIS soft data weight. Higher B_i values increase soft data influence on local estimations, while lower B_i values discount soft data.

One drawback of SIS / COSIS is that any indicator may occur next to any other. Sedimentary rocks comprise predictable successions at all scales, and a modeler may wish to specify which facies can occur adjacent to one another (i.e., facies stacking patterns). The following sections introduce methods that utilize truncated gaussian fields to build models with specified facies order.

2B.5 Truncated Gaussian Simulation

Truncated Gaussian Simulation (TGS) is a covariance-based sequential simulation method designed to conditionally "truncate" a random continuous gaussian field into spatially ordered categorical data (Matheron et al., 1987; Galli et al., 1994; Emery, 2007; Armstrong et al., 2011; Beucher and Renard, 2016). With this method, indicators are guaranteed to occur in a specified transition order. Consider, for example, a generic, 3-facies coastline succession: coastal-plain facies occur adjacent to shoreface sandstone facies, which is successively bounded by offshore muddy facies (Fig. 2.1A). There is 0% probability that coastal plain will transition to offshore and 100% probability that shoreface will occur in between. This specified order of transition is mathematically defined with a gaussian random function (GRF) of the cumulative facies probabilities (Fig. 2.1B) and may be visualized with a block diagram called a lithotype

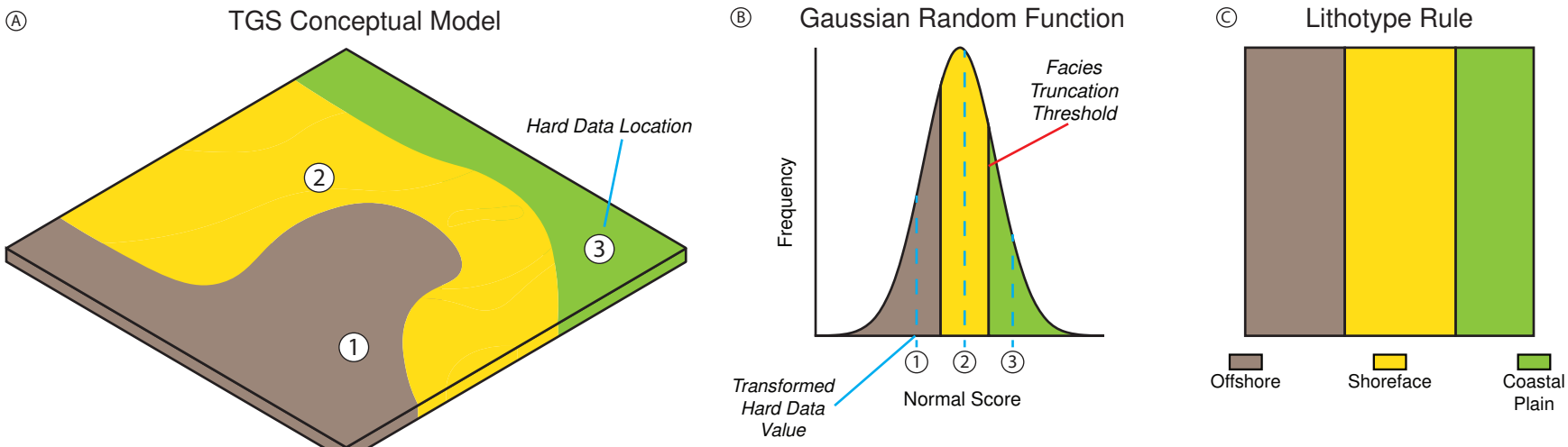

Figure 2.1: Example model of a hypothetical coastal succession with the truncated gaussian method. A) Truncated gaussian simulation of three facies with example hard data locations. B) Gaussian random function describing facies proportions and facies truncation thresholds. Hard data transformation normal scores at the center of each facies are marked. C) Truncated gaussian lithotype rule.

rule (LTR) (Fig. 2.1C) (Beucher and Renard, 2016). The relative area of each facies within the LTR square corresponds to their respective proportions.

First, cumulative facies proportion data at each cell is converted to a GRF, where spatially adjacent facies are also next to each other under the curve (Fig. 2.1B). Proportion data may not be the same everywhere in the model, but if there is variability, it becomes fixed at this step. Next categorical facies hard data is transformed into continuous data based on the GRF: generally, the normal score at the center of the facies area on the GRF is assigned for that facies (Fig. 2.1B) (Pyrcz and Deutsch, 2014). These normal-score values are used to condition a continuous gaussian simulation in the model grid. Various techniques may be used (e.g., sequential gaussian simulation or turning bands). Finally, the gaussian simulation values are converted back to their corresponding facies based on the previously-determined thresholds at each cell. This truncation is described as:

$$\text{facies at } \mathbf{u} = k \text{ if } y_{k-1}^{t}(\mathbf{u}) < y(\mathbf{u}) \leq y_{k}^{t}(\mathbf{u}) \qquad (Eq.\ 2.6)$$

where $y(\mathbf{u})$ are the gaussian simulation values and $y^{t}_{k}(\mathbf{u})$, k = 1, …, K – 1 are the thresholds. Multiple equiprobable realizations are achieved by iterating the seed, generating a new gaussian realization, and applying the previously calculated thresholds.

Fitting the variogram for TGS is not straightforward. Unlike indicator simulation, where a variogram can be fit for each facies if desired, for TGS, only one variogram can be used to describe the spatial continuity of the underlying GRF, and by extension, the joint behavior of all facies at once. Furthermore, while there is a simple relationship between the facies indicator variogram and requisite normal-scores gaussian variogram for 2-facies modeling, it does not hold for larger numbers of facies (Journel and Isaaks, 1984; Pyrcz and Deutsch, 2014). For models with more than two facies, either the most important indicator variogram, or a weighted

average of all the indicator variograms is inverted to produce the underlying gaussian variogram (Kyriakidis et al., 1999).

2B.5.1 Nested Modeling

TGS variogram limitations can be circumvented by using a nested modeling approach. Consider facies A, B, and C. First A is modeled with a temporary combined category: *B and C*. The realization is then segregated into A and non-A zones, and B and C are modeled only in the reserved non-A zone. This nested procedure can be expanded to any number of facies, allowing specified variography at each step.

Nested modeling of this sort is especially advantageous for TGS because, unlike SIS, which has only two licit variogram models, TGS can use any licit variogram model because the assumed underlying gaussian variable is continuous, not categorical.

2B.6 Plurigaussian Simulation

As a natural extension of TGS, Plurigaussian Simulation (PGS) expands the LTR concept from one-to-one facies transitions to one-to-many facies transitions. Each sequence of possible transitions is represented by a separate underlying GRF, and all GRFs are simulated at once. Most implementations of PGS are limited to two GRFs, but more are theoretically possible (Armstrong et al., 2011). Complex, but ordered, arrangements of facies can be achieved in this way. For instance, consider the 3-facies coastal succession from the previous section, but the modeler wishes to include an altered facies within the shoreface (Fig. 2.2A). The first GRF (Fig. 2.2B) describes two successions on the LTR "x-axis": 1) the original; offshore, shoreface, and coastal plain, and 2) the new; offshore, altered shoreface, and coastal plain. The second GRF describes transitions between the original shoreface and altered shoreface facies on the LTR "y-axis" (Fig. 2.2C). The LTR visualizes all facies proportions and transition behavior (Fig. 2.2D).

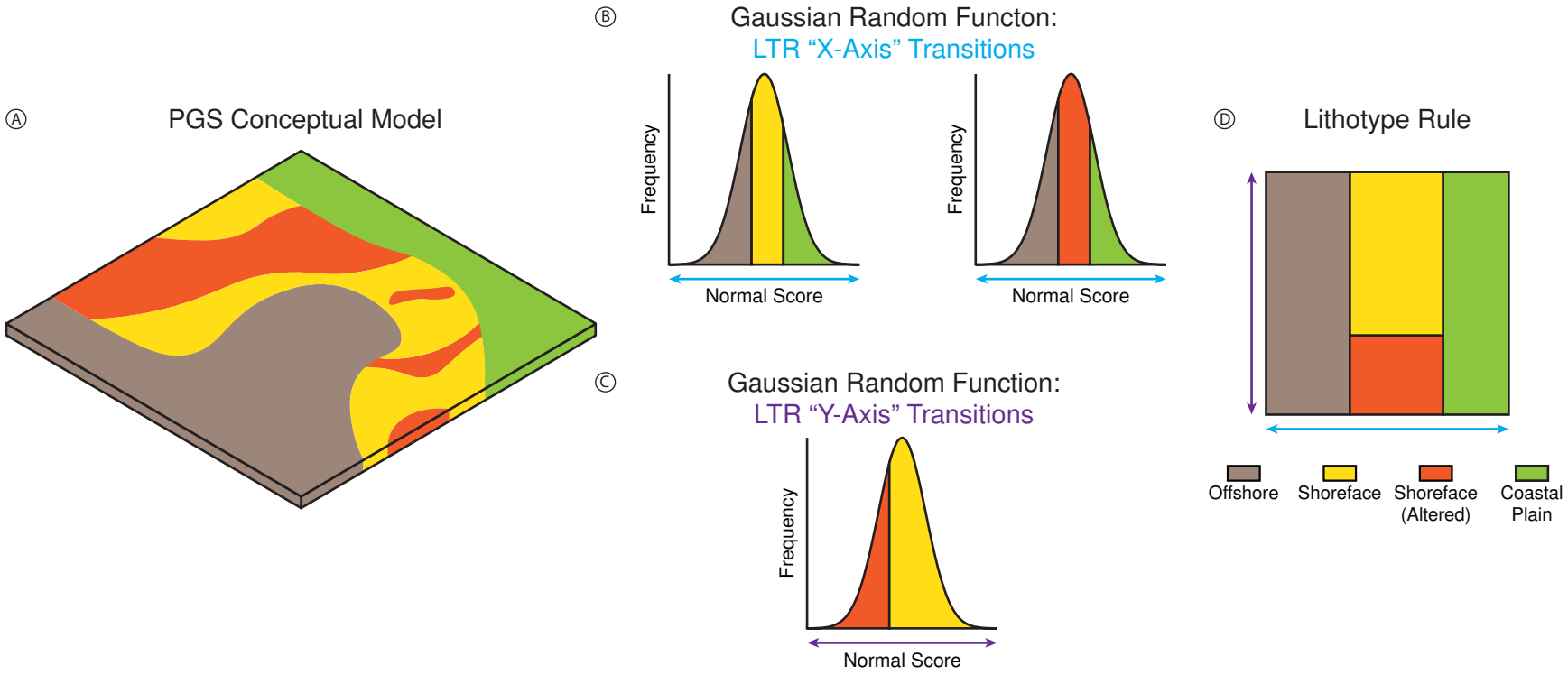

Figure 2.2: Example model of a hypothetical coastal succession with additional altered shoreface facies. A) Plurigaussian simulation of four facies. B) Gaussian random function describing facies proportions and facies truncation thresholds for coastal succession with both shoreface and altered shorface facies on LTR "x-axis." C) Gaussian random function describing facies proportions and facies truncation for transition between shoreface and altered shoreface on LTR "y-axis." D) Plurigaussian lithotype rule expanded to four facies with two GRFs.

For such "2-axis" LTR blocks, facies transitions may occur along either axis. For instance, the shoreface may transition to offshore or coastal plain on the "x-axis," or it can transition to altered shoreface on the "y-axis."

Combining multiple GRFs into one field requires non-unique inversion (Pyrcz and Deutsch, 2014). Hard and soft facies data are converted to gaussian space using iterative algorithms (e.g., Gibbs sampler) that ensure the final distributions of transformed values are truly gaussian (Emery, 2007; Armstrong et al., 2011). PGS variography is subject to the same advantages and limitations of TGS: each underlying gaussian field is controlled by a single variogram model, which limits control over individual facies, but the number of licit models is high compared to SIS.

2B.7 Proportion vs. Probability and Other Soft Data Considerations

Probability and proportion are related but distinct concepts in facies modeling. Generally, modeling proportions are derived from indicator hard data, while soft data brings indicator probability information into play. Judiciously incorporating both into a facies model is often subjective. A probability is a hypothetical model, while proportions summarize observations at a specific volume support (Stright et al., 2009). Many descriptions of methods and algorithms appear to use the terms interchangeably. For instance, when a method inspects "local facies proportion" information at a single cell, it is evaluating the probability of facies occurrence for the entire cell, not determining what percentage of that cell should be assigned to a given facies. The cell is the representative elemental volume the modeler has decided on and not subdivided. This concept of "local proportion" at a cell is framed as a deviation from the global proportions; it should be treated and understood as facies probability.

Many soft data integration methods trust soft data as implicitly reliable local proportion information or correct facies probabilities in a standardized way prior to simulation (e.g. Bayesian updating or locally varying means (Doyen et al., 1994; Goovaerts, 1997)). From the perspective of the reservoir modeler as practitioner, differences among the most robust of these soft data integration methods are relatively minor (Deutsch, 2006a). Assumptions and uncertainty about real-world input data are likely to have an outsize effect relative to soft data integration procedures. As such, modeling software packages often make the soft data integration decision for the user. For COSIS, different, widely-implemented software packages employ different co-kriging methods, and full co-regionalization modeling is often not an option. For instance, SGeMs (Remy et al., 2002) makes use of the Markov-Bayes Model, while Petrel (Schlumberger, 2016) uses a form of locally varying means. TGS (in Petrel (Schlumberger, 2016) and PGS (in Isatis (Geovariances, 2016)) incorporate soft data prior to simulation into the underlying gaussian fields. Certain implementations will make additional standardized corrections to the soft data volume prior to simulation based on the global target facies proportions.

However, if soft and hard data are poorly matched or the soft data is known to be unreliable, inherent trust in soft data may pose problems. One of the benefits of the Markov-Bayes Model for COSIS is explicit control over the weight given to soft data. This proves useful when soft data calibration is suspect, or a variable to test.

CHAPTER 3: GEOLOGIC BACKGROUND

The Western Canada Sedimentary Basin (WCSB) is a retro-arc foreland basin that formed in response to the eastward advance and crustal loading of the Sevier Orogeny in western North America (Leckie and Smith, 1992). The Horseshoe Canyon Formation was deposited into the WCSB during the Late Cretaceous (~73-67 Ma; Campanian-Maastrichtian) (Hamblin, 2004). These fluvial and estuarine sediments form part of an eastward -prograding and -thinning clastic sedimentary package that deposited into the intracratonic Western Interior Seaway (WIS) (Shepheard and Hills, 1970) (Fig. 3.1A). East-flowing tributaries, which sourced sediment from the northwest-southeast-oriented mountain belt, combined into a major orogen-parallel river that discharged southeast into the ocean (Eisbacher et al., 1974; Rahmani, 1988; Leckie and Smith, 1992; Michaelsen and Henderson, 2000; Hamblin, 2004; Eberth et al., 2012) (Fig. 3.1B).

The focus of this research is the Horseshoe Canyon Formation, which outcrops southeast of Drumheller, Alberta in the Red Deer River Valley. At this locale, the 12-16 m thick fluvial point bar section erosionally overlies Bearpaw shoreface deposits and conformably underlies a regional coal seam (Shepheard and Hills, 1970; Ainsworth and Walker, 1994; Vakarelov et al., 2012; Ainsworth et al., 2015). The Red Deer River exposes the fluvial point bar Horseshoe Canyon deposits subparallel to depositional strike, and a tributary, Willow Creek, exposes the deposits subparallel to dispositional dip (Durkin et al., 2015) (Fig. 3.2). The study interval comprises a single point bar and its associated abandonment-channel fill, where major erosional surfaces define the internal stratigraphic architecture of the point bar into a series of LAPs (See: 2A.3 Fluvial Point Bar Depositional Environment) (Durkin et al., 2015) (Fig. 3.3). While point bar migration direction was variable through time, trough-cross stratification indicates paleoflow

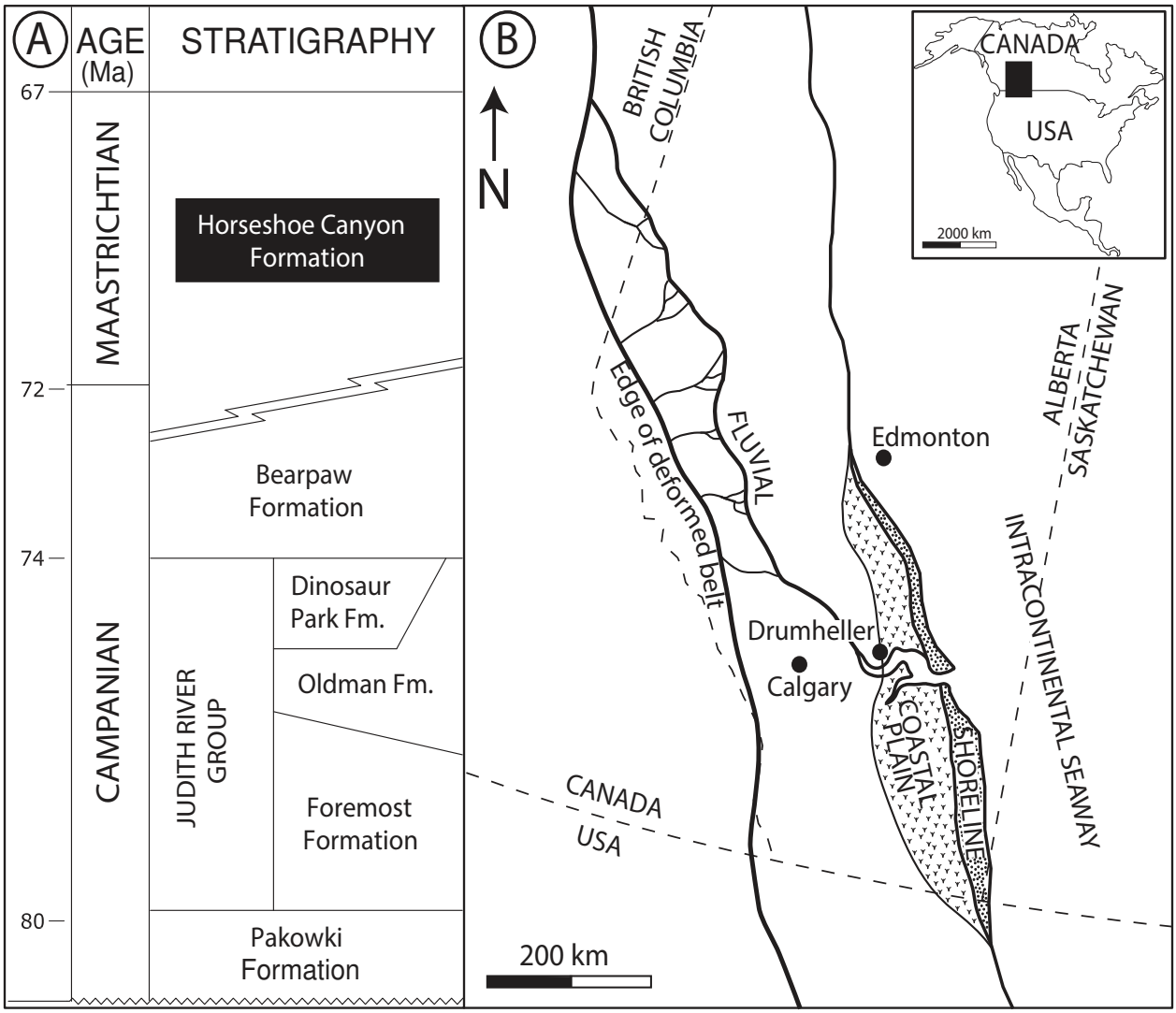

Figure 3.1: A) Stratigraphic Column for Horseshoe Canyon Formation. B) Paleogeographic reconstruction of WCSB for Horseshoe Canyon Formation time (modified from Hamblin, 2004); modfied from Durkin et al., 2015. Inset map shows location in North America (modified from Rahmani 1988; Leckie and Smith, 1992; Hamblin, 2004; modfied from Durkin et al., 2015).

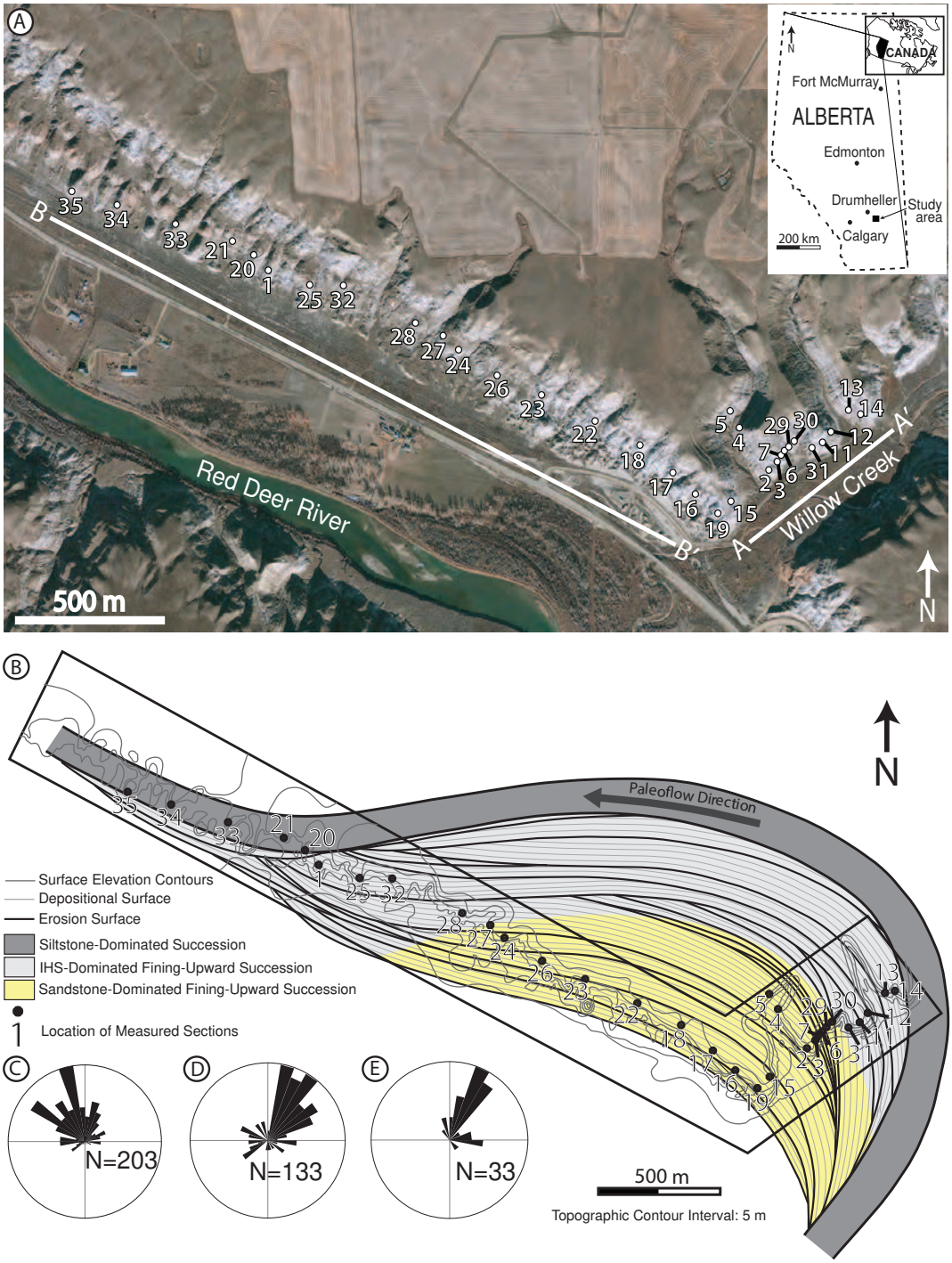

Figure 3.2: A) Satellite image (Google, 2016 - DigitalGlobe) of outcrops in the Red Deer River valley with measured sections locations. Study location shown on inset. B) Map-view interpretation of the point bar and associated abandoned channel deposits. Lateral accretion package migration direction varies through time, and deposits become more fine-grained from upstream to downstream. C) Paleoflow measurements (trough-cross stratification and clast imbrication) D) Depositional surfaces dip direction. E) Erosion surfaces dip direction. (Modfied from Durkin et al., 2015)

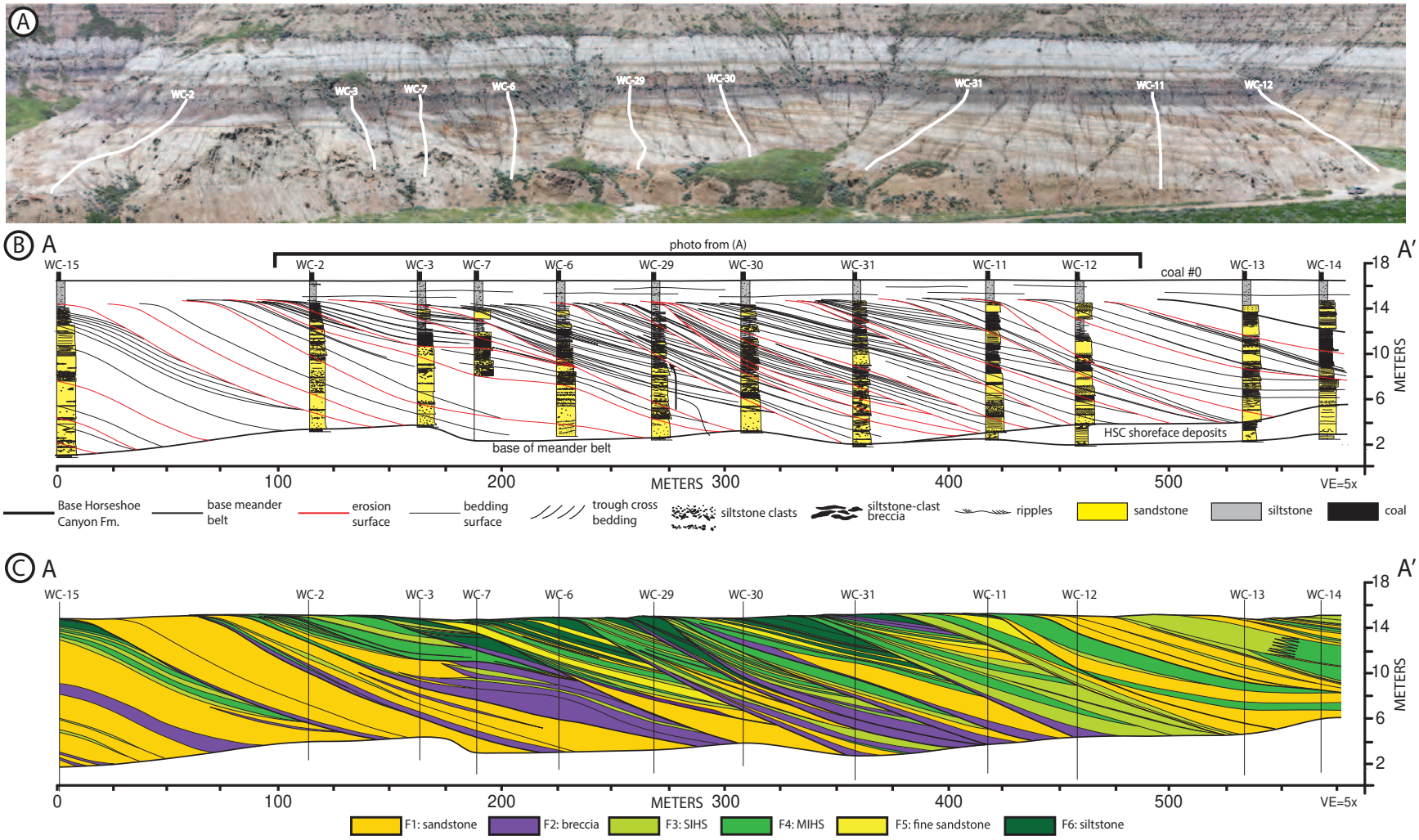

Figure 3.3: A) Willow Creek outcrop photomosaic with indicated section locations. B) Cross-sections of all Willow Creek measured sections oriented in the depositional dip direction. Includes field observations and photomosaic analysis. C) Corresponding facies correlation of B) (Modified from Durkin, 2016).

directions generally to the northwest, while erosional and depositional surface dips are roughly orthogonal, to the northeast (Fig. 3.2C-E).

Six facies are defined in the point bar deposits (Table 3.1). High-energy facies include: sandstone (F1), siltstone-clast erosional breccia (F2), and sandstone with siltstone and organic interbeds (sandy inclined heterolithic strata) (SIHS; F3). Moderate-energy facies include: siltstone with sand and organic interbeds (muddy inclined heterolithic strata) (MIHS; F4), and very fine to fine-grained sandstone with ripples (F5). Low-energy suspension settling deposition represented by one facies: siltstone (F6).

Sandstone-dominated successions are high-energy accumulations of cross-stratified sandstones (F1), associated with breccias (F2), and laterally discontinuous siltstone interbeds (F3) interpreted as high-energy point bar growth and lateral migration (Allen, 1970; Jackson, 1976). Breccias derived from erosion of previously-deposited material pervade at the base, where they are associated with LAP-bounding erosional surfaces, while sporadic SIHS indicates lower-energy flows and sedimentation. IHS-dominated successions record oscillation between high-energy, unidirectional flow (F3) and low-energy suspension settling (F4) depositional regimes. The alternation of finer and coarser beds of IHS are likely governed by seasonal changes in sedimentation rate. Breccias (F2) persist locally, indicating lesser bank slumps and erosional events. Siltstone-dominated successions record slow channel flow or standing water deposition. Laminated siltstones (F6) predominate, but are punctuated with minor fine sandstones (F5) indicating sporadic periods of faster flow.

Overall, the study interval is dominated by sandstone. While breccias are most common at the erosive bases of LAPs, they can occur as minor slumps throughout the deposit. IHS facies become increasingly prevalent up-section and eventually transition into siltstones. The deposit

Table 3.1: Facies of the Horseshoe Canyon Formation in the study area

Lithofacies	Grain Size / Sorting	Sedimentary Structures	Color	Bedding	Upper / Lower Contacts	Process Interpretation	Depositional Setting
F1: Sandstone Massive and cross-stratified sandstone with siltstone clasts	vfU to mL; organic detritus; silt clasts pebble to cobble; sand moderately well-sorted	Trough crossstratification, cross-set thickness ranges from 5 cm – 40 cm; organics on foresets; graded and massive beds; coarser lags at base of beds	Sand = light gray to white; silt = reddish brown and gray	Cross-set thickness = 5 – 40 cm; bed thickness = 10 - 100 cm; unit thickness ≤ 8 m	Sharp, erosional base; sharp and gradational upper	Unidirectional current flow; Traction-dominated bedload; erosion of previously deposited silt beds with moderate transport distance	Channel thalweg 3D dunes; Lateral-accreting lower-point-bar IHS
F2: Breccia Siltstone-clast breccia	vfU to mL sand; silt clasts 10 - 200 cm blocks; subangular to angular; sand moderately well-sorted	Imbrication of silt clasts; massive sand	Sand = light gray to white; silt = reddish brown and gray	Bed thickness = 20 - 150 cm; unit thickness ≤ 4 m	Sharp base; gradational upper contact from breccia to sandstone	Traction-dominated bedload; unidirectional current flow; erosion of previously deposited silt beds with short transport distance	Channel thalweg adjacent to cut-bank; Lower to middle point bar
F3: SIHS Sandstone with siltstone and organic interbeds	vfL to fU sand; organic detritus; silt; sand moderately well-sorted	Horizontal lamination; current ripples; wavy and discontinuous silt and organic lamination; organics on ripple foresets, double mud drapes	Sand = light gray to white; silt = reddish brown and gray; organics = black	Bed thickness = sand 1 - 5 cm, silt 1 - 5 mm, oranics 1 - 3 mm; unit thickness ≤ 8 m	Gradational lower; sharp and gradational upper	Low-energy unidirectional current flow; fluctuations in discharge	Laterally accreting lower to middle point-bar IHS; periodic tidal fluctuation
F4: MIHS Siltstone with sandstone and organic interbeds	vfL to fU sand; organic detritus; silt; sand moderately well-sorted	Planar to wavy lamination; rare ripples in sandstone beds; wavy lenticular sand lenses	Sand = light gray to white; silt = reddish brown and grey; organics = black	Bed thickness = silt 1 - 3 cm, discontinuous sand 1 - 5 mm, organics 1 - 3 mm; unit thickness ≤ 8 m	Gradational and sharp	Low-energy unidirectional current flow; fluctuations in discharge	Upper point-bar IHS; periodic tidal fluctuation
F5: Fine Sandstone Very fine to fine sandstone with ripples	vfL to fU sand; organic detritus; sand moderately sorted	Current riiples with organic detritus on foresets; massive; faint planar lamination	Sand = light gray to white; silt = reddish brown and gray; organics = black	Bed thickness = sand 10 - 100 cm; unit thickness ≤ 4 m	Gradational lower from massive sandstone; sharp upper with finegrained	Low-energy unidirectional current flow; fluctuations in discharge	Upper point-bar IHS; tidal channels and drainage creeks outside of channels in tidal flats or overbank deposits
F6: Siltstone Laminated Siltstone	Clay to silt	Planar lamination; rare and discontinuous sandstone interlamination; massive; fissile	silt = light brown and gray; organics = black	Bed thickness = 1 - 3 cm ; unit thickness ≤ 8 m	Sharp or gradational at base; sharp upper	Low-energy deposition from suspension	Abandoned channel or upper point bar

(Modified from Durkin et al., 2015)

becomes increasingly finer-grained up-section and downstream, but successively-deposited LAPs also become finer-grained through time (Fig. 3.3C).

CHAPTER 4: DATA REVIEW

This study relies on previous: 1) outcrop field work and 2) architectural statistical and modeling work based on that outcrop work, which is used as a base framework and comparison case. Measured section data and interpreted stratal surfaces come from a detailed stratigraphic study of the Horseshoe Canyon Formation (Durkin et al., 2015). Previous statistical and modeling work developed architectural statistics calculated within stratal packages as a function of position within the package (Durkin, 2016). These include transition probabilities and facies proportion curves. Soft data was derived from interpolated facies proportion curves and variography was inferred from outcrop hard data. A nested TGS model was generated with this data to evaluate facies architecture reproduction.

4.1 Previous Outcrop Work

4.1 1 Measured Sections

35 measured sections taken along the outcrop record grainsize, bedding contacts, facies, and various sedimentary structures (Fig. 3.2A and B). Trough-cross-stratification measurements indicate paleo current directions for the growing point bar, and inform paleo-channel interpretations (Fig. 3.2C-E).

4.1.2 Stratigraphic Framework

Major stratigraphic surfaces were walked out and recorded with dGPS. These surfaces were then linked to measured section data locations and outcrop photographs to build a georeferenced, 3-D representation of the outcrop data (Fig. 3.3B and C). Measured section locations were imported into Petrel 2016 (Schlumberger, 2016) as wellbores, and digitized facies interpretations were assigned to wellbore tracks. LAPs that intersect the wellbores were added

as well tops and combined with dGPS points to constrain 3-D LAP surface construction. Paleo dip and azimuth data at measured sections aided accurate surface projection. The resulting 21 major surfaces define the framework for a point bar comprised of 20 LAPs (Zones 1-20, Fig. 4.1). Zones are numbered from youngest (zone = 1) to oldest (zone = 20) and correspondingly from most southwestward to northeastward, advancing in the direction of point bar migration.

At most, the model grid area spans roughly 3.7 km on its long axis (NW-SE) and 0.9 km on its short axis (SW-NE), with an approximate modeled area of 2 km^2 covering approximately 68 m of vertical section. The grid comprises 430 x 457 x 1,111 (i,j, and k respectively) truncating cornerpoint-gridded cells that are 5 m x 5 m across and 0.3 m thick. Cells are layered such that they follow their lower bounding surface and are truncated by the overlying erosional surface (i.e. follow-base gridding paradigm). After trunctation, the model contains 2,601,027 active cells. Where wellbores intersected cells, facies were assigned to the grid by upscaling. That is, the cell was assigned the most abundant wellbore facies within its volume. Every cell with hard data was assigned to a depositional sub-zone: top, top-middle, middle, middle-bottom, and bottom, each referring to an interpreted relative position within the point bar (Fig. 4.2). With measured section hard data deterministically emplaced and encoded into a stratigraphic architectural framework, outcrop statistics were developed in four spatial categories: zone (LAP), sub-zone, true spatial coordinates (x, y, z), and cellular coordinates (i, j, k).

4.2 Previous Architectural Statistics and Modeling Work

4.2.1 Transition Probabilities

Transition probabilities for each facies (to each other facies) were calculated using Markov-chain analysis. Vertical transition probabilities were assessed using an embedded Markov analysis, which has no spatial dependency. For each facies, the number of transitions to each

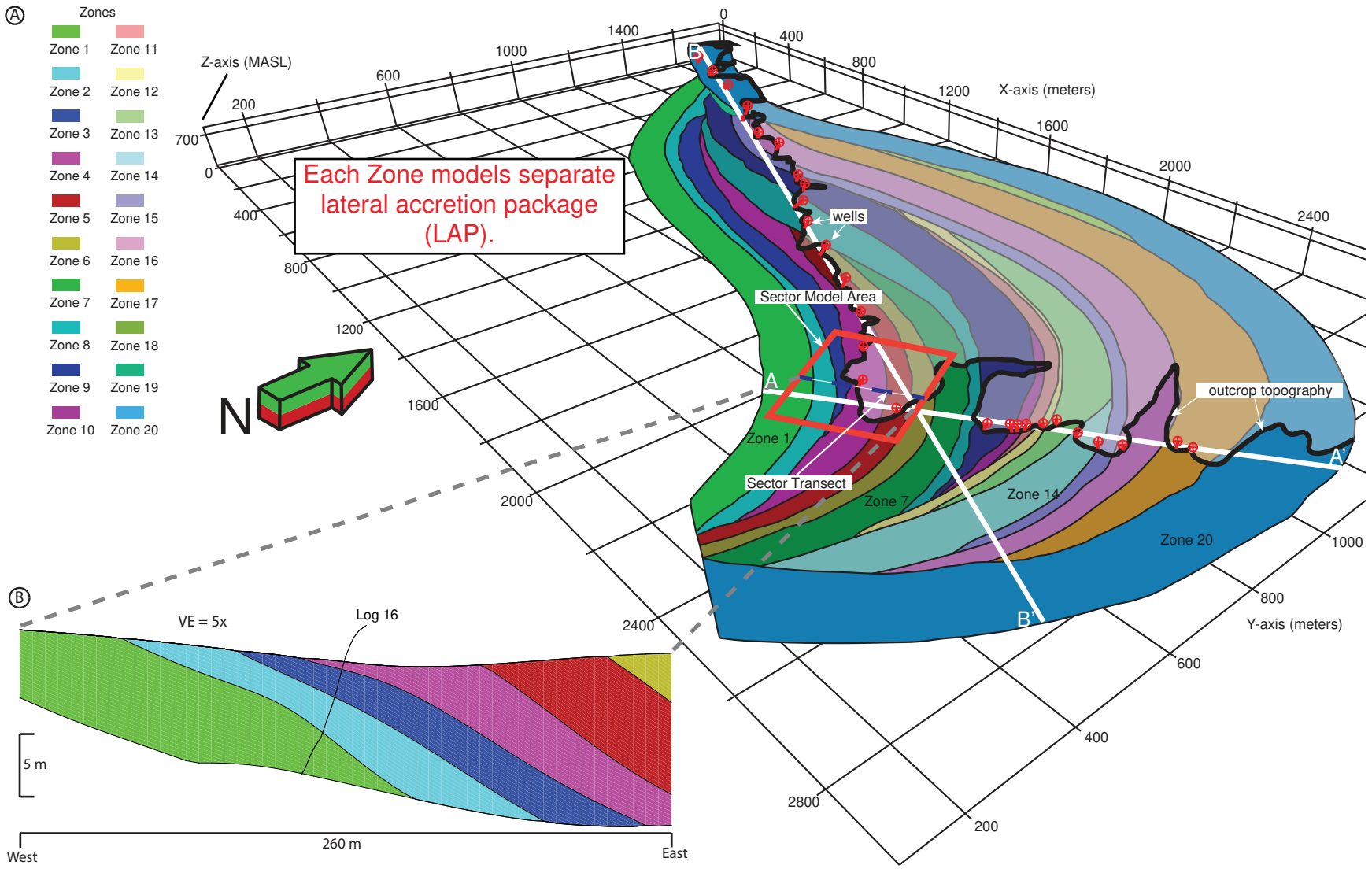

Figure 4.1: A) Zone architecture of the geocellular model. Locations of the Willow Creek cross-section and measured-section "pseudo-wells" are indicated. A small sector model taken for testing and transect for visualization are also labeled. B) The sector transect inspects six LAP Zones. (Modified from Durkin, 2016).

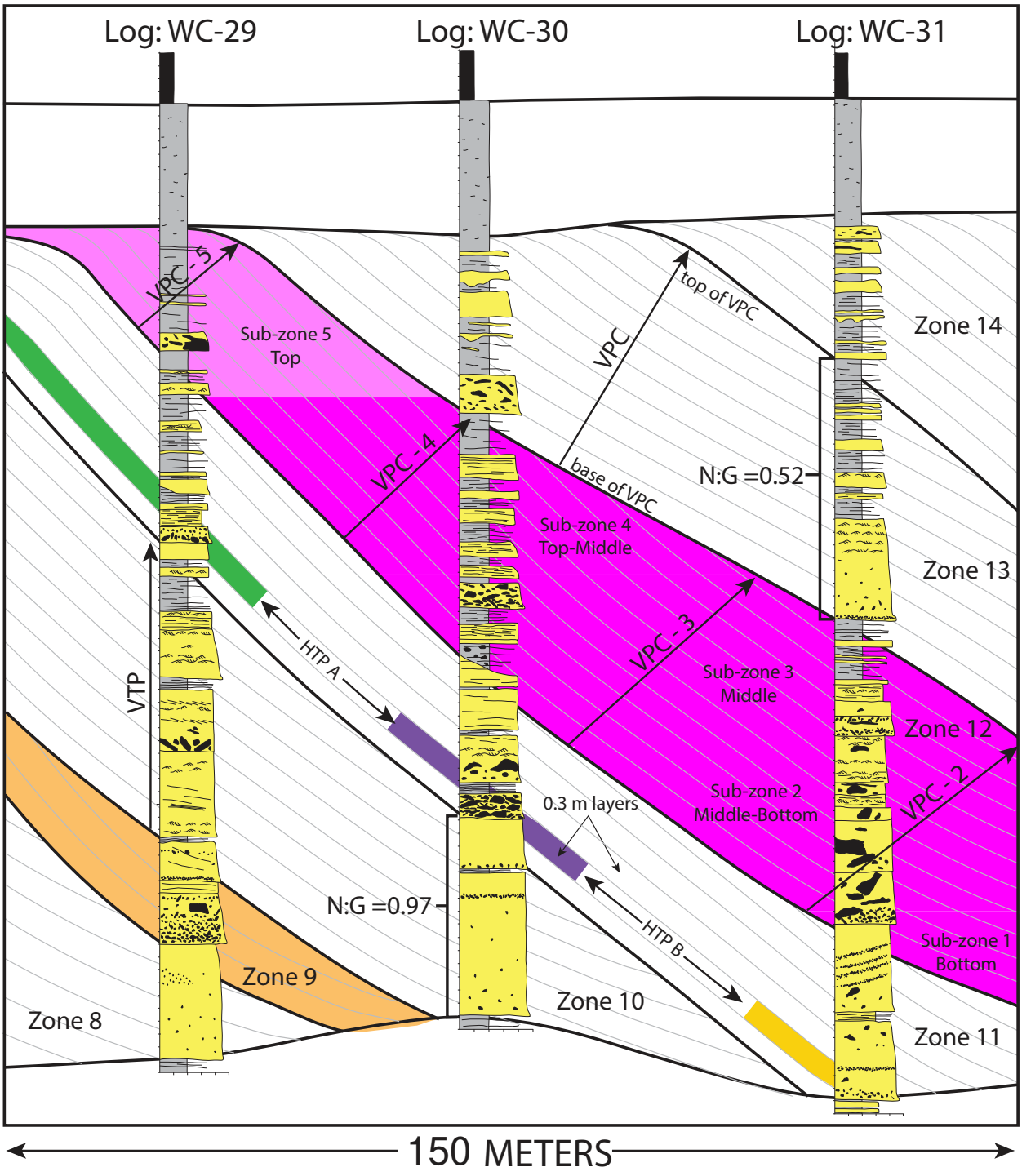

Figure 4.2: Willow Creek measured sections indicating key statistical parameters and stratigraphic architecture. (Modfied from Durkin, 2016)

other facies (up-section, along well logs) was divided by the total number of transitions to build a matrix of vertical transition probabilities (Table 4.1, Fig. 4.3) (Miall, 1973; Ethier, 1975; Burgess, 2016).

Table 4.1: Vertical Transition Probabilities

	Sandstone	Breccia	SIHS	MIHS	Fine Sand	Siltstone
Sandstone	-	0.37	0.17	0.39	0.02	0.05
Breccia	0.76	-	0.06	0.15	-	0.03
SIHS	0.13	0.07	-	0.67	0.02	0.12
MIHS	0.41	0.11	0.36	-	0.07	0.05
Fine Sand	0.08	-	0.08	0.29	-	0.54
Siltstone	0.21	0.12	0.33	0.07	0.28	-

Without spatial dependence, facies self-transitions are unobservable and recorded as nulls. Horizontal transition probabilities were assessed with using a spatial Markov analysis, which considers transitions at a fixed sampling interval (Miall, 1973; Ethier, 1975; Burgess, 2016). For each facies, the number of transitions to each other facies (including itself) along model layers was divided by the total number of transition intervals to build a matrix of horizontal transition probabilities (Table 4.2, Fig. 4.4) (Schwarzacher, 1969; Ethier, 1975).

Table 4.2: Horizontal Transition Probabilities

	Sandstone	Breccia	SIHS	MIHS	Fine Sand	Siltstone
Sandstone	0.65	0.16	0.05	0.13	0.01	0.00
Breccia	0.37	0.45	0.06	0.13	-	-
SIHS	0.32	0.20	0.18	0.25	0.01	0.04
MIHS	0.41	0.19	0.11	0.26	0.02	0.02
Fine Sand	0.24	0.06	0.19	0.28	0.18	0.06
Siltstone	0.14	0.12	0.20	0.35	0.01	0.18

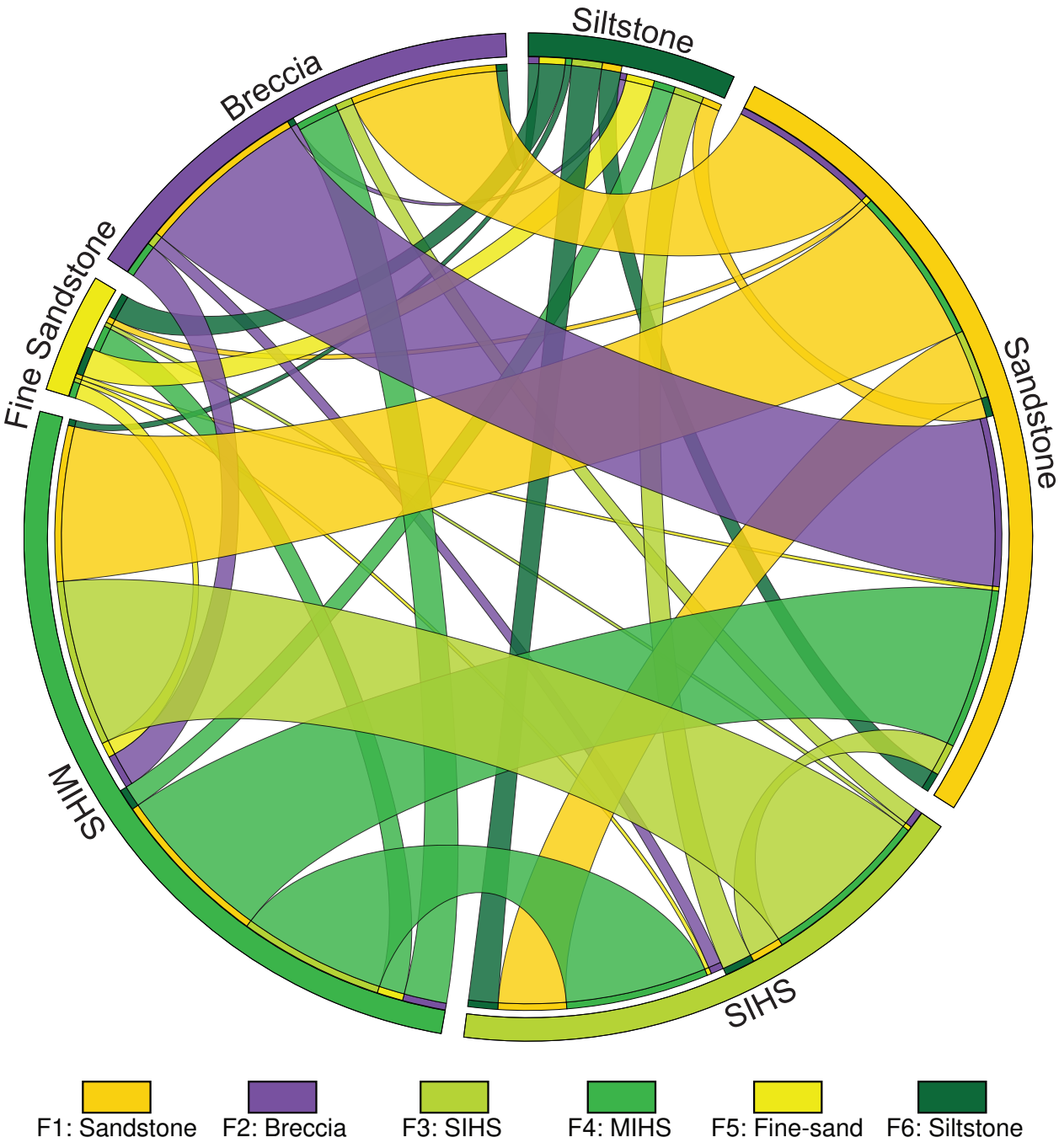

Figure 4.3: Vertical transition probabilities visualized as Circos diagrams (Circos Table Viewer, 2017) where colored bands represent probability of transition between given facies. Tabulated transition probabilities (transitions from a given facies) are reflected in the attached series, while the detached series represent tranitions to a given facies.

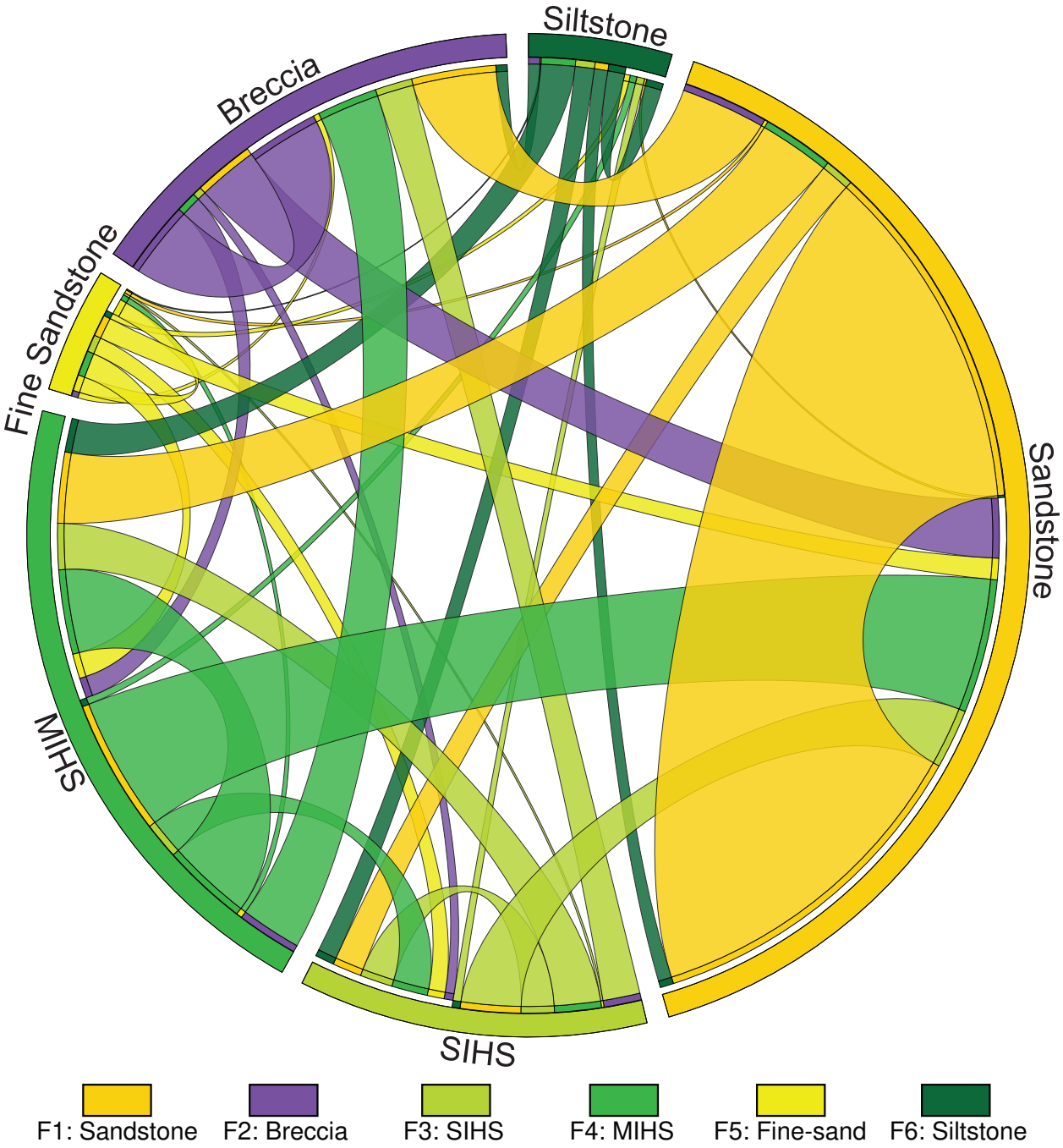

Figure 4.4: Horizontal transition probabilities visualized as Circos diagrams (Circos Table Viewer, 2017) where colored bands represent probability of transition between given facies. Tabulated transition probabilities (transitions from a given facies) are reflected in the attached series, while the detached series represent tranitions to a given facies.

Due to the geometry of the outcrops, transitions at distances greater than 200 m were not considered. For both vertical and horizontal analyses, if a facies never transitions to a particular facies (e.g., F2 never transitions to F5 in the horizontal analysis), the transitions are recorded as null.

4.2.2 Horizontal and Vertical Facies Proportion Curves

Proportion curves show spatial changes in facies proportion throughout the model hard data: in this case horizontally by sub-zone and vertically by model layers (Ravenne et al., 2002). Vertical proportion curves (VPC) were calculated for each model layer at all zones: one in aggregate and five by sub-zone (Fig. 4.5, 4.6). Starting with the bottom layer, each facies occurrence on that layer is tallied and plotted as a cumulative percentage. This process is repeated for each layer and the resulting curve visualizes facies proportion trends up-section. The aggregate VPC considers all measured sections at the same time while sub-zone VPCs only include cells coded for a particular sub-zone. Sub-zone analyses may reveal important architectural trend information while aggregate analyses characterize the dataset as a whole. One horizontal proportion curve was collected by sub-zone for all sub-zones (Fig 4.5). Instead of inspecting layers, facies counts were collected for all cells in the sub-zone at once. This analysis captures depositional architectural quantitatively.

4.2.3 Probability Models (Soft Data)

Probability volumes based on sub-zone VPCs were developed as soft data to guide stochastic modeling. Recall that each cell of upscaled measured section data has a defined model layer (Fig. 4.2) and interpreted sub-zone (i.e., top, top-middle, middle, middle-bottom, and bottom) (Fig. 4.6) (See: 4.1.2 Stratigraphic Framework). Taken together, these values correspond to a VPC value for each facies (Fig. 4.6). Measured section locations were assigned

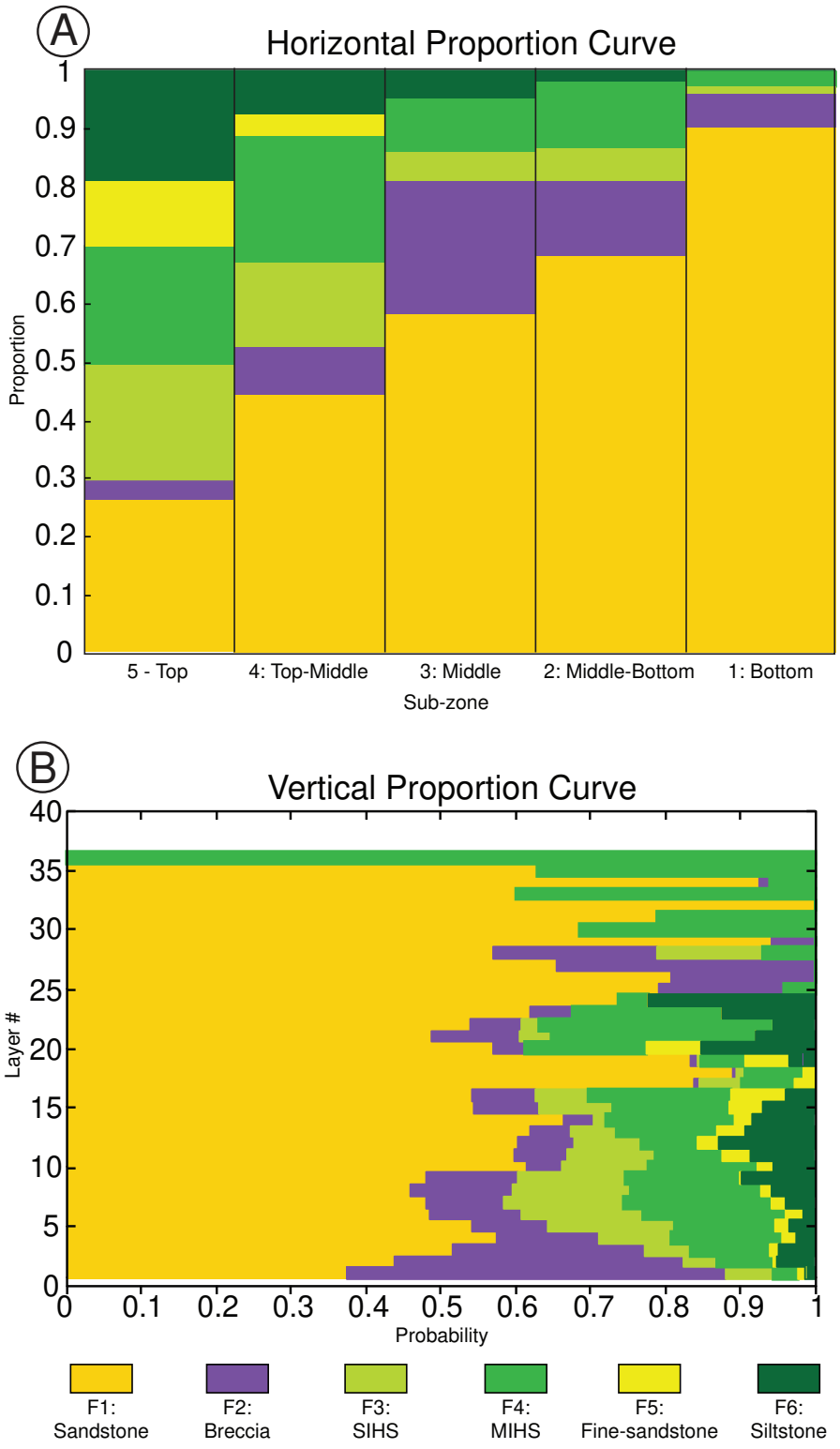

Figure 4.5: A) Global horizontal proportion curve (HPC) by sub-zone, for all zones in the geocellular model. B) Global vertical proportion curve (VPC) for all zones. Probability of each facies for each layer in a zone, starting at the base (layer #1) to the top of the zone (layer #36). (Modified from Durkin, 2016)

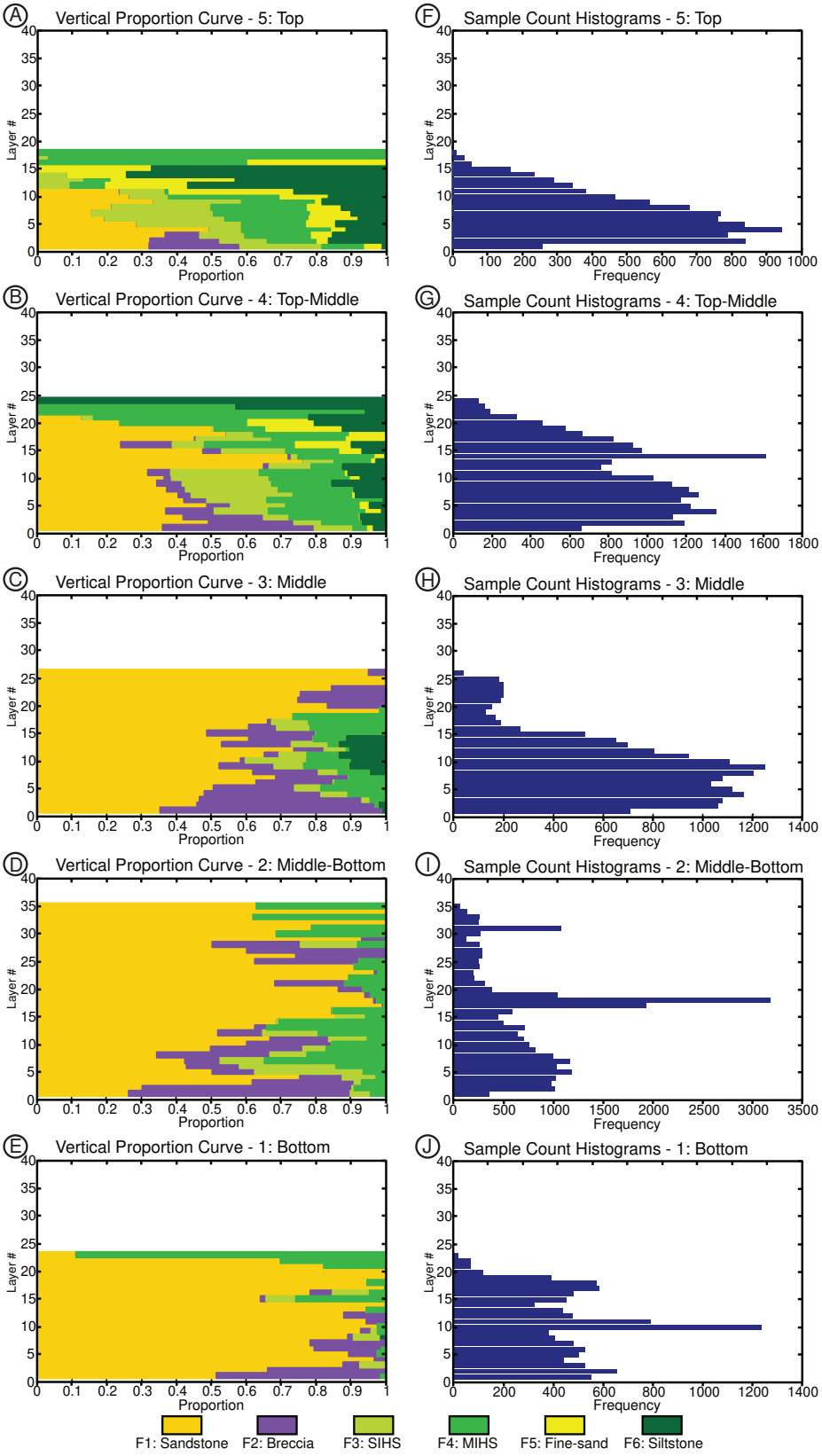

Figure 4.6: A)-E) Vertical proportion curves (VPC) by sub-zone, for all zones in the model. F)-J) with corresponding histograms. (Modified from Durkin, 2016)

VPC facies proportion values on this basis, and then linearly interpolated along layers between other measured section locations to fill the entire model volume with facies probability values (Fig. 4.7).

4.2.4 Variography and Nested TGS Model

Facies variogram models were inferred directly from outcrop character instead of noisy experimental data (Table 4.3) (See: 2B.5 Truncated Gaussian Simulation).

Table 4.3: Outcrop-Inferred Facies Variogram Parameters

Facies	Model	Hz. Range (m)	Vt. Range (m)	Sill (σ^2-Normalized)
Sandstone	Gaussian / Exponential	100	0.3	1
Breccia	Gaussian / Exponential	300	0.3	1
All Others	Gaussian / Exponential	600	0.3	1

The variogram model was derived from a combination of: 1) the observed visual continuity of facies bedding and thickness and 2) desired qualitative model results based on trial and error. Gaussian variogram models were selected because they form smoother, less noisy, more geologically realistic facies transitions than, e.g., spherical or exponential models. Please note, while gaussian variogram models were used in the previous work, exponential models are substituted for SIS and COSIS simulations with outcrop-inferred variography in this study, as indicated in Table 4.3 (See: 2B.1.1 Indicator Formalism and Indicator Variograms).

Finally, these variograms were used to build a nested TGS model (Fig. 4.8). The model was fully conditioned with outcrop hard data and the probability volumes for each facies. Facies were simulated in order of architectural importance: sandstone, breccia, SIHS, MIHS, fine sandstone, and siltstone, with the probability volumes supplying local proportions. In the final model, facies proportions are compared to proportions from logs in order to ensure consistency.

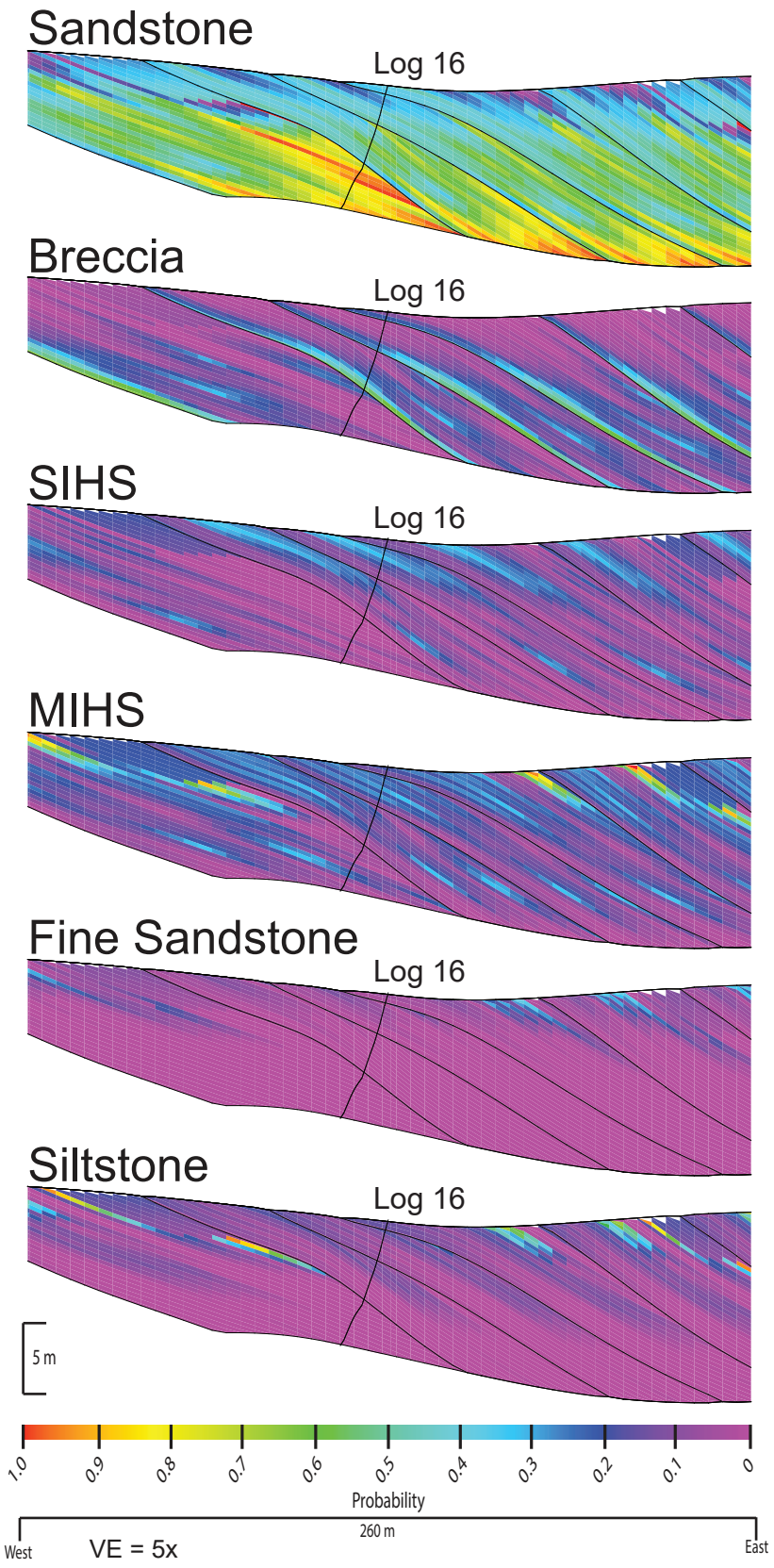

Figure 4.7: Probability volumes for all facies visualized at sector model transect.

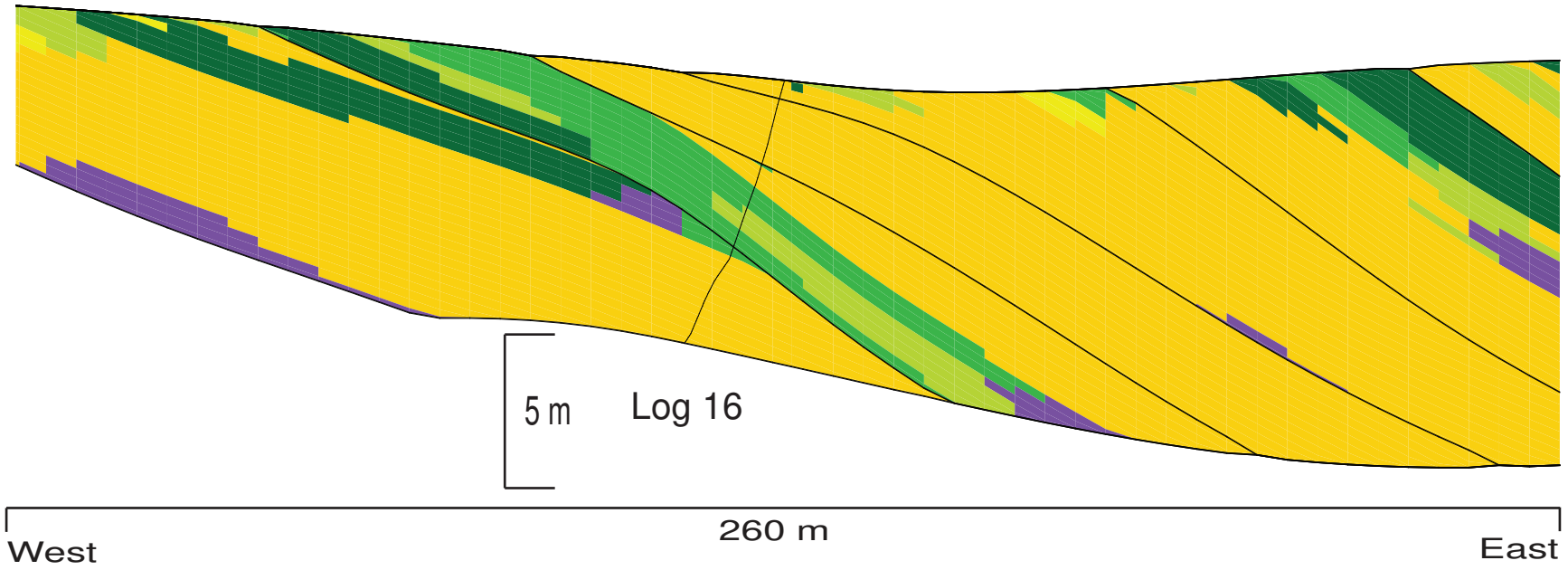

Variography

-Hz -- Sand : 100m, Breccia: 300m;
600m for all others

-Vt -- 0.3m for all facies

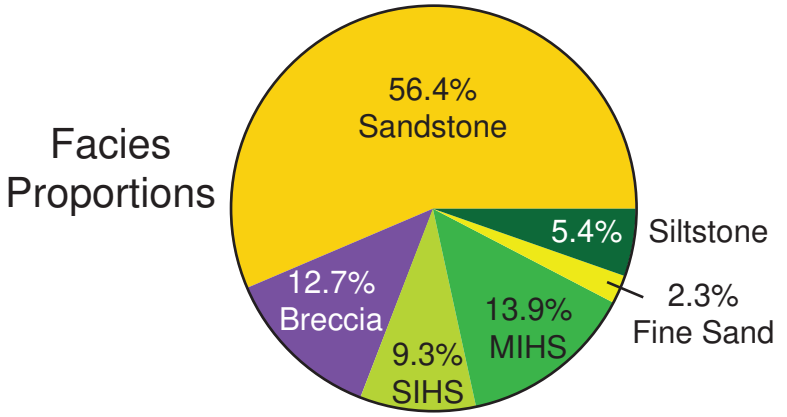

Figure 4.8: Cross-section slice of nested TGS Model from with input variography and facies proportions. Model is extracted from Durkin, 2016 data.

For this study, the nested TGS model is used as a base case to qualitatively compare other 3-D model results against.

CHAPTER 5: METHODS

Facies architecture reproduction is often difficult to quantify and historically relied on qualitative evaluations. One such approach to is to visually inspect map-view and cross-sections through model realizations and make general qualitative assessments for each algorithm or parameterization tested (Deveugle et al., 2014). The goals herein are to use simple 1-D experiments to better understand how covariance-based simulation methods: 1) honor input data and 2) quantitatively reproduce observed sedimentologic architecture. Finally, learnings are applied to 3-D problems. The overarching goal is to close the gap between statistics measured at the outcrop and use of those statistics in modeling to reproduce observed architecture. Measurements from the outcrop are distilled down into several quantitative data types: 1) facies at measured section locations, 2) probability models from interpolated VPC curves, 3) global facies proportions, 4) spatial correlation models from variograms, and 5) transition probabilities captured in facies LTR. Several sensitivity variables are considered: number of facies, facies proportions, variography, search parameters, kriging style, soft data-hard data calibration, and soft data weight for simple, exhaustively-understood cases. For 1-D experiments, COSIS with a Markov-Bayes Model of co-regionalization is used as a test algorithm because of its explicit control over soft data weight. 3-D experiments expand general findings of COSIS to PGS and nested TGS.

5.1 Part 1: 1-Dimensional Experiment Methods

A set of simple 1-D modeling tests were devised to: 1) quantify model accuracy as a function of varying soft data reliability (Part 1a) and weighting (Part 1b), 2) quantify model accuracy given varying hard data scenarios (i.e., changing abundance and configuration) (Part

1b), 3) evaluate variogram impacts (Part 1b), 4) evaluate search ellipse impacts (Part 1b), and 5) compare differences between a model with two facies (Part 1a) and three facies (Part 1b). These experiments aggressively test the limits of covariance-based algorithms with respect to facies architecture reproduction: realizations are evaluated on how well they reproduce a known spatial distribution of facies. This reaches far beyond the expectation that algorithms reproduce spatial correlation, Instead, it provides a quantitative gauge for algorithm performance with respect to facies architecture demonstrating how soft data is being utilized in facies reproduction and under which conditions soft data influences the results.

5.1.1 Part 1a: Synthetic 2-Facies Experiment - Soft Data Reliability

A simple, synthetic, 1-D modeling experiment with two facies ("shale" and "sand") was devised to illustrate and examine limits of soft data influence on facies architecture reproduction (Fig. 5.1). To test the impacts of facies prediction as a function of soft data reliability, or *B*, unconditional simulations (i.e., no hard data) were run with COSIS with soft data volumes of varying reliability (i.e., changing *B* value). SIS simulations serve as a control, as SIS cannot consider soft data.

First, an arbitrary 13-cell, 1-D model of a true facies distribution was developed (Fig. 5.1A). The model comprises three cells of sand placed at the top, bottom, and middle of a 1-D grid separated by beds of shale, each five cells thick. True facies distribution proportions of shale and sand are ~77% and ~23%, respectively (Fig. 5.1C). From this true facies distribution, 22 soft data scenarios were systematically developed to test facies prediction impacts of incrementally changing *B* from 1 to -1 (See: 2B.4.1 Markov-Bayes Model of Co-regionalization). Total results comprise: 1 SIS simulation (1 SK simulation) and 44 COSIS

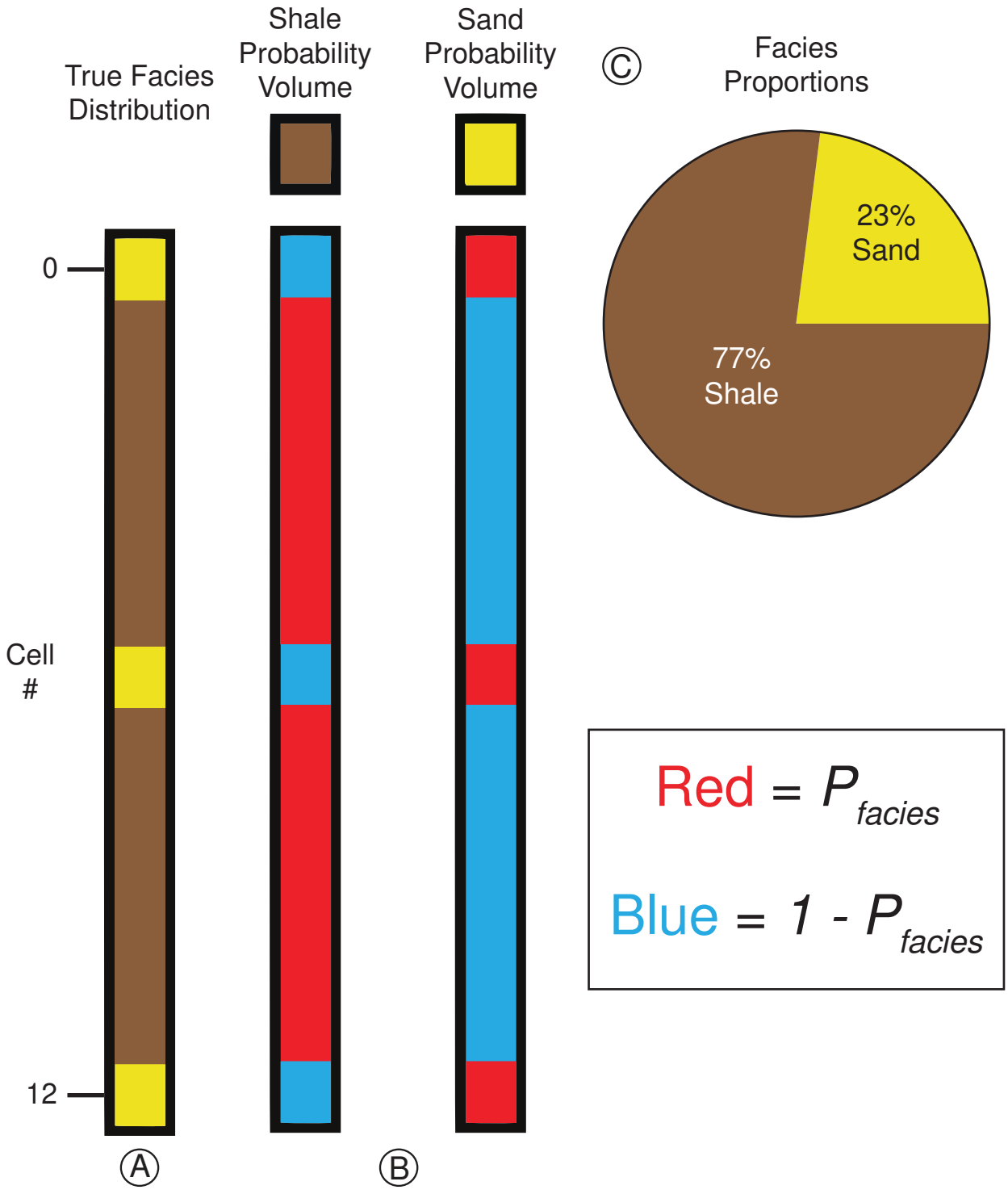

Figure 5.1: Part 1a: 2-Facies Synthetic Experiment to Test Soft Data Reliability. A) True facies distribution, B) soft data volumes, and C) facies proportions for synthetic 1-D experiment.

simulations (22 SK simulations and 22 OK simulations), each of 100 realizations. Facies indicator variograms were inferred from the true facies distribution hard data (Table 5.1).

Table 5.1: Part 1a: Synthetic 1-D Experiment Variography

Facies	Model	Range (units)	Sill (σ^2)
Sand	Exponential	2	0.18
Shale	Exponential	5	0.18

The search ellipse encompassed the entire grid. Input soft data weight, or B_i, was held at ~1, implying full confidence in soft data. The method is tested for its ability to predict the true facies distribution given fixed global proportions and variogram input across a range of soft data reliability scenarios.

Soft data scenarios for COSIS were set up in the following manner. First, a suite of 22 *B* values was selected ranging from ~ 1 to ~ -1, where each *B* value corresponds to a soft data scenario (Table 5.2). Probability volumes were then populated for each scenario. Given that facies probabilities must sum to 1 and there are only two facies in this system, a facies' average probability, P_{facies}, can be calculated from a given *B* value:

$$B = P_{facies} - \left(1 - P_{facies}\right)$$
$$or$$
$$P_{facies} = \frac{B + 1}{2} \qquad (Eq. 5.1)$$

The true facies distribution informs where P_{facies} is assigned in the soft data grids (Fig. 5.1B). For the sand probability volume, sand cells in the true facies distribution are assigned P_{facies}, while shale facies are necessarily assigned $1 - P_{facies}$. The shale probability volume is populated in the same fashion. With this procedure, the probability volumes for each scenario are homogenous and diametric, keeping the experiment simple.

Table 5.2: Part 1a: Synthetic 1-D Experiment Facies Probabilities and *B* Values

P_{facies}	1 - P_{facies}	*B*
0.99	0.01	0.98
0.95	0.05	0.90
0.90	0.10	0.80
0.85	0.15	0.70
0.80	0.20	0.60
0.75	0.25	0.50
0.70	0.30	0.40
0.65	0.35	0.30
0.60	0.40	0.20
0.55	0.45	0.10
0.49	0.51	-0.02
0.51	0.49	0.02
0.45	0.55	-0.10
0.40	0.60	-0.20
0.35	0.65	-0.30
0.30	0.70	-0.40
0.25	0.75	-0.50
0.20	0.80	-0.60
0.15	0.85	-0.70
0.10	0.90	-0.80
0.05	0.95	-0.90
0.01	0.99	-0.98

5.1.2 Part 1b: Outcrop-Data 3-Facies Experiments - Hard and Soft Data Conditioning

A 3-facies, 1-D example from a measured section in the Horseshoe Canyon dataset comprises the basis for a second set of 1-D tests (Fig. 5.2; Log 24 of the Horseshoe Canyon Outcrop. See: Fig. 3.2 for section location). These tests were devised to evaluate the impact of: 1) variable abundance and configuration of hard data and 2) variogram range, search ellipse, and soft data weight. These tests utilized both SIS and COSIS simulation.

To simplify the experiment, facies F3-F6 were aggregated to one category: fine-grained facies. A 31-cell, single-zone portion (only zone 8) of Log 24 was extracted to serve as an idealized 1-D vertical true facies distribution (Fig. 5.2C). This true facies distribution: 1) comprises one of the longest single-zone logs, 2) contains the best qualitative example of the idealized point bar depositional profile, and 3) exhibits comparable facies proportions to the global facies proportions from all measured sections (Table 5.3).

Table 5.3: Horseshoe Canyon Facies Modeling Proportions

Facies		**Global Proportions**		**Log 24 Proportions**		**Sector Model Probability Volume Avg.**	
Sandstone		0.56		0.71		0.53	
Breccia		0.13		0.06		0.13	
Fine-grained Facies	SIHS	0.31	0.09	0.23	-	0.34	0.09
	MIHS		0.14		0.19		0.15
	Fine Sandstone		0.02		-		0.03
	Siltstone		0.05		0.03		0.07

Facies target proportions are drawn only from Log 24 hard data, as opposed to all measured sections (Table 5.3). While providing a limited test case, Log 24 data has the advantage of being grounded in measured outcrop data, whereas the 2-facies experiments are entirely synthetic.

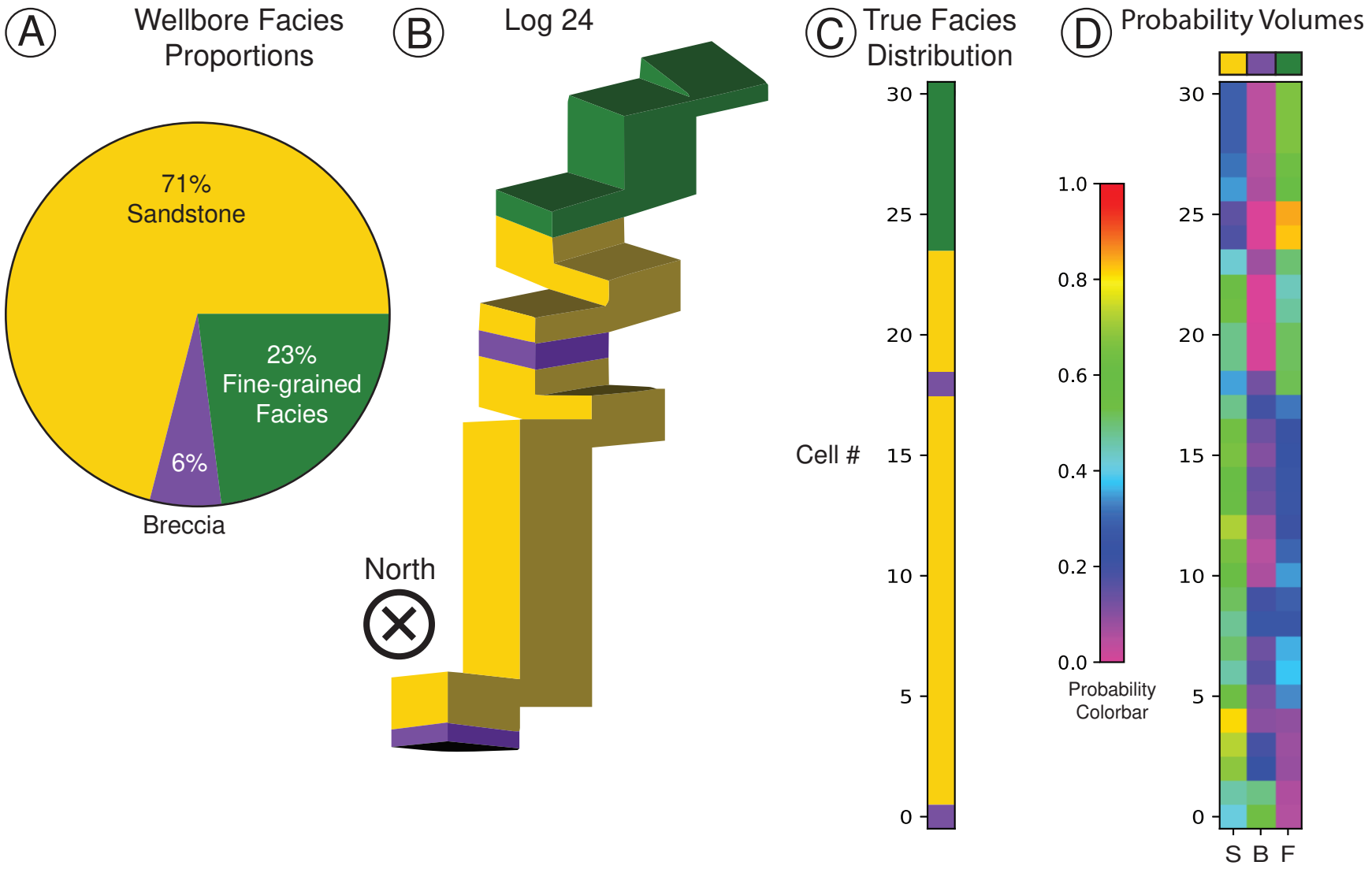

Figure 5.2: Part 1b: 3-Facies Outcrop-Based Experiments to Test Hard and Soft Data Conditioning. A) Facies proportions in well Log 24. B) Upscaled geocellular representation of Log 24 in 3-D model. C) Log 24 upscaled facies flattened to idealized 1-D vertical grid. D) Log 24 probability volumes for sandstone, breccia, and aggregated fine-grained facies.

Simulations were run with different degrees of hard data conditioning (hard data percentage) to test the relative impacts of hard and soft data on facies prediction. A suite of 156 hard data scenarios were extracted from Log 24 at six different hard data percentages: 1) 1 scenario at 0% hard data (i.e., unconditional) and 2) 31 scenarios each at ~3%, ~6%, 12.5%, 25% and 50% hard data (Fig 5.3). For each hard data percentage scenario, hard data was systematically spaced and positioned to ensure: 1) a manageable, explicit range and variety of data scenarios were tested (i.e., one for each cell in the grid) and 2) data was distributed evenly throughout the grid for each scenario. Given the small number of model cells, clustered adjacent hard data may unnecessarily bias experimental results. Unlike the 2-facies models, soft conditioning data (probabilities) were heterogeneous, derived from full-field probability models (Durkin, 2016), and held constant in the 3-facies cases (Fig. 5.2D).

Through automated processes (Appendix), each of these 156 scenarios was subjected to 42 parameter sets examining different configurations of variogram range, search ellipse, and soft data weight to evaluate impacts on 3-facies 1-D modeling (Fig. 5.4). This full suite of simulations comprises 6,552 different data and parameter configurations, each with 100 realizations. Indicator variograms were modeled from experimental data from all outcrop measured sections (Fig. 5.5, Fig. 5.6, Table 5.4).

Table 5.4: Part 1b: Outcrop-data 1-D Experimentally Fit Variography

Facies	Model	Vertical Range (m)	Sill (σ^2)
Sandstone	Exponential	2.1	0.25
Breccia	Exponential	2.7	0.11
Fine-grained Facies	Exponential	2.1	0.21

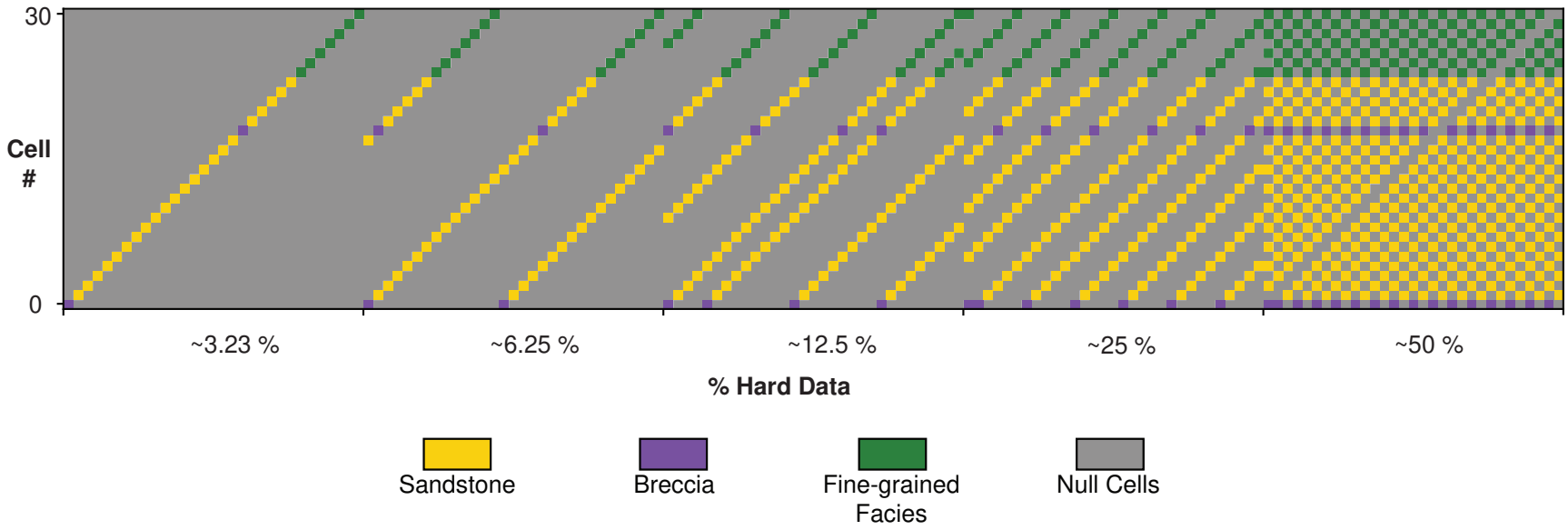

Figure 5.3: Part 1b: 3-Facies Outcrop-Based Experiments to Test Hard and Soft Data Conditioning. Hard Data Scenarios extracted from Log 24. 156 hard-data scenarios were tested: 31 at each of 5 different hard data percentages and one with no hard data (i.e., unconditional).

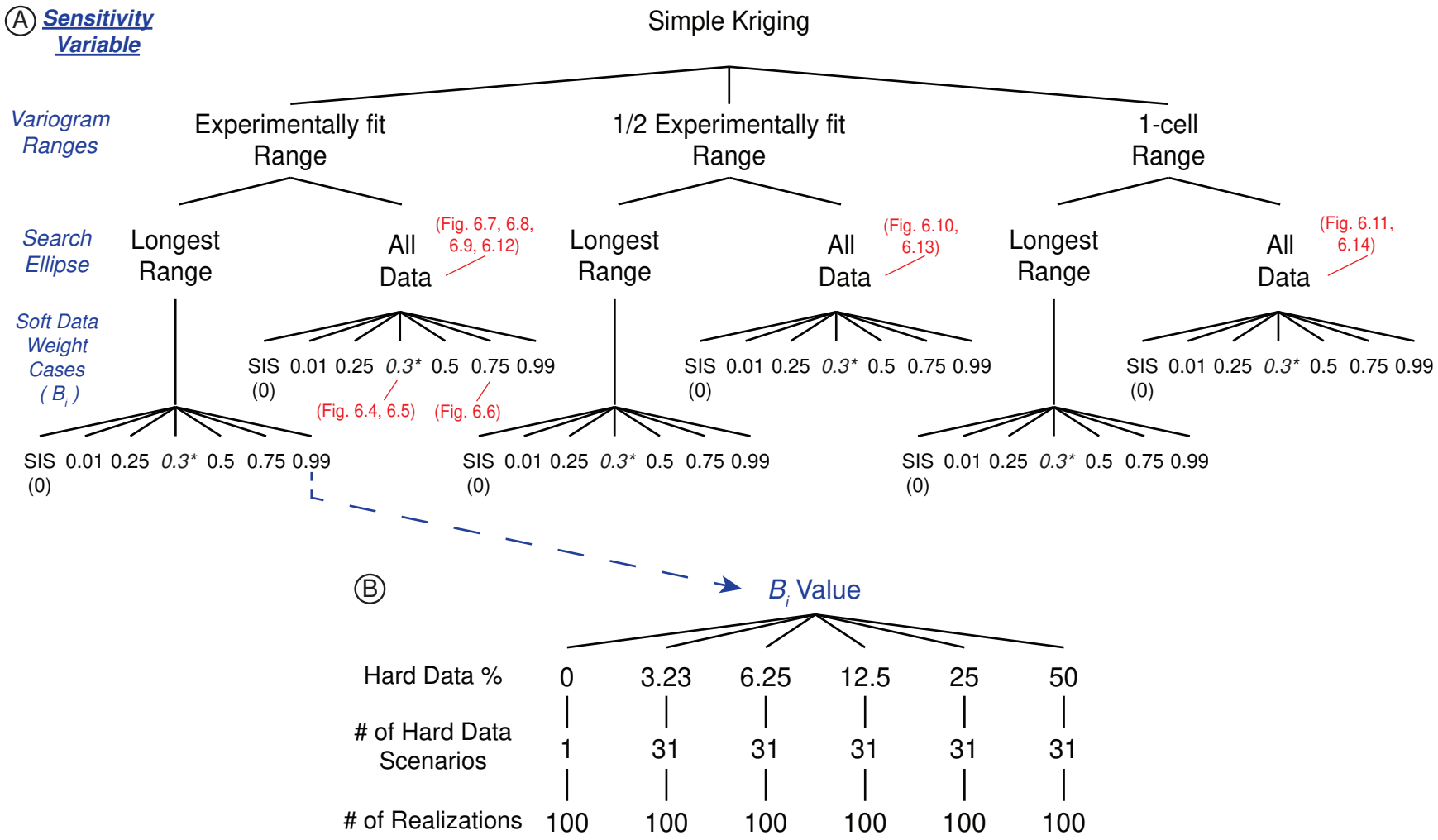

Figure 5.4: Part 1b: 3-Facies Outcrop-Based Experiments Sensitivity Variable Test Tree. A) Three variogram ranges, two search ellipses, and seven soft data weight cases were tested with simple kriging. **0.3* soft data weights are detailed in Table 5.6. B) 156 hard data scenarios were tested for each soft data weight case.

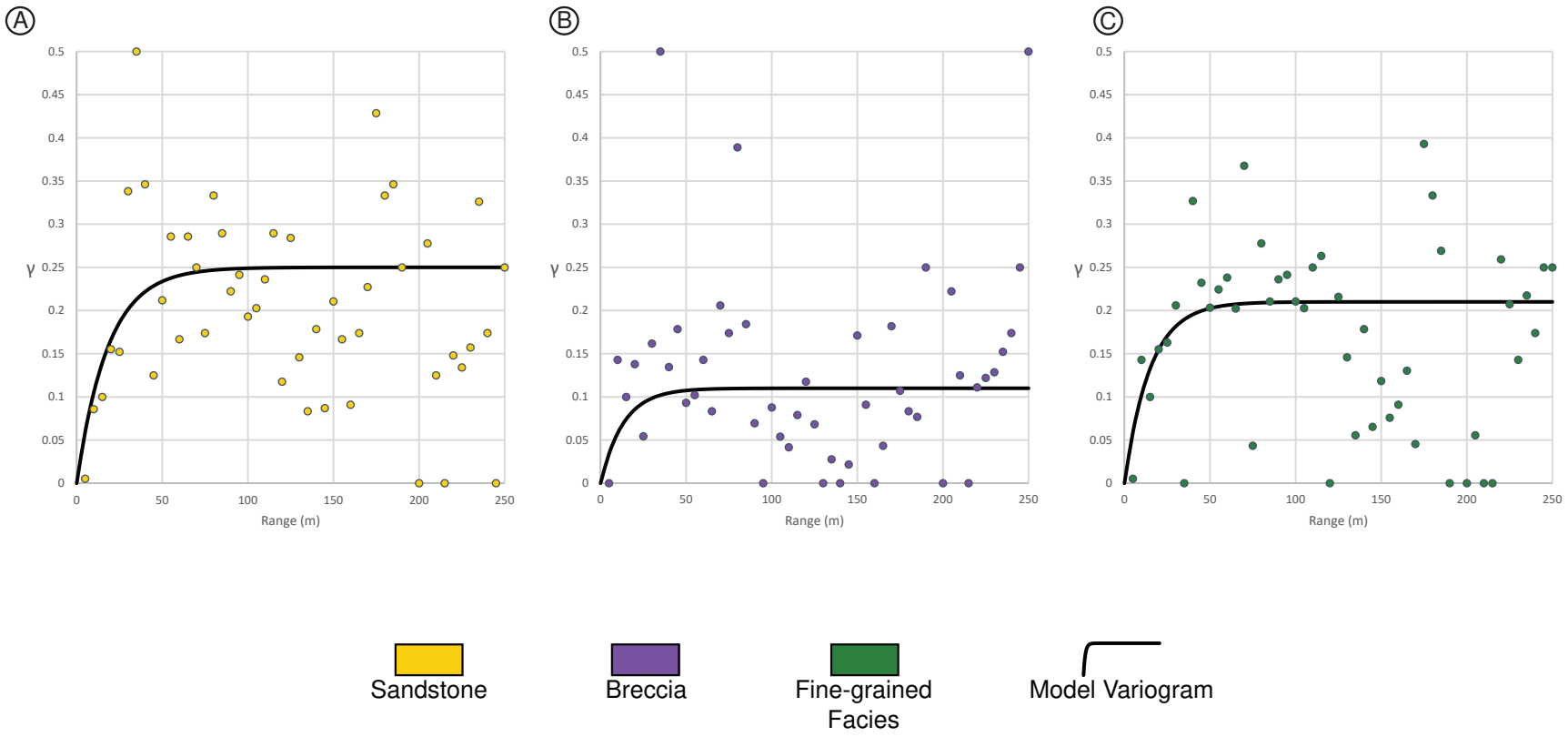

Figure 5.5: Horizontal direction experimentally-fit variograms and exponential models: A) sandstone experimental variogram and model, B) breccia experimental variogram and model, and C) fine-grained facies variogram and model. Experimental variograms were modeled for 500 lags (5 m separation, 2.5 m tolerance) with 0° azimuth, 0° dip, 90° tolerance, 0 m bandwidth. Exponential models are detailed in Table 5.7 for 3-D models (Part 2).

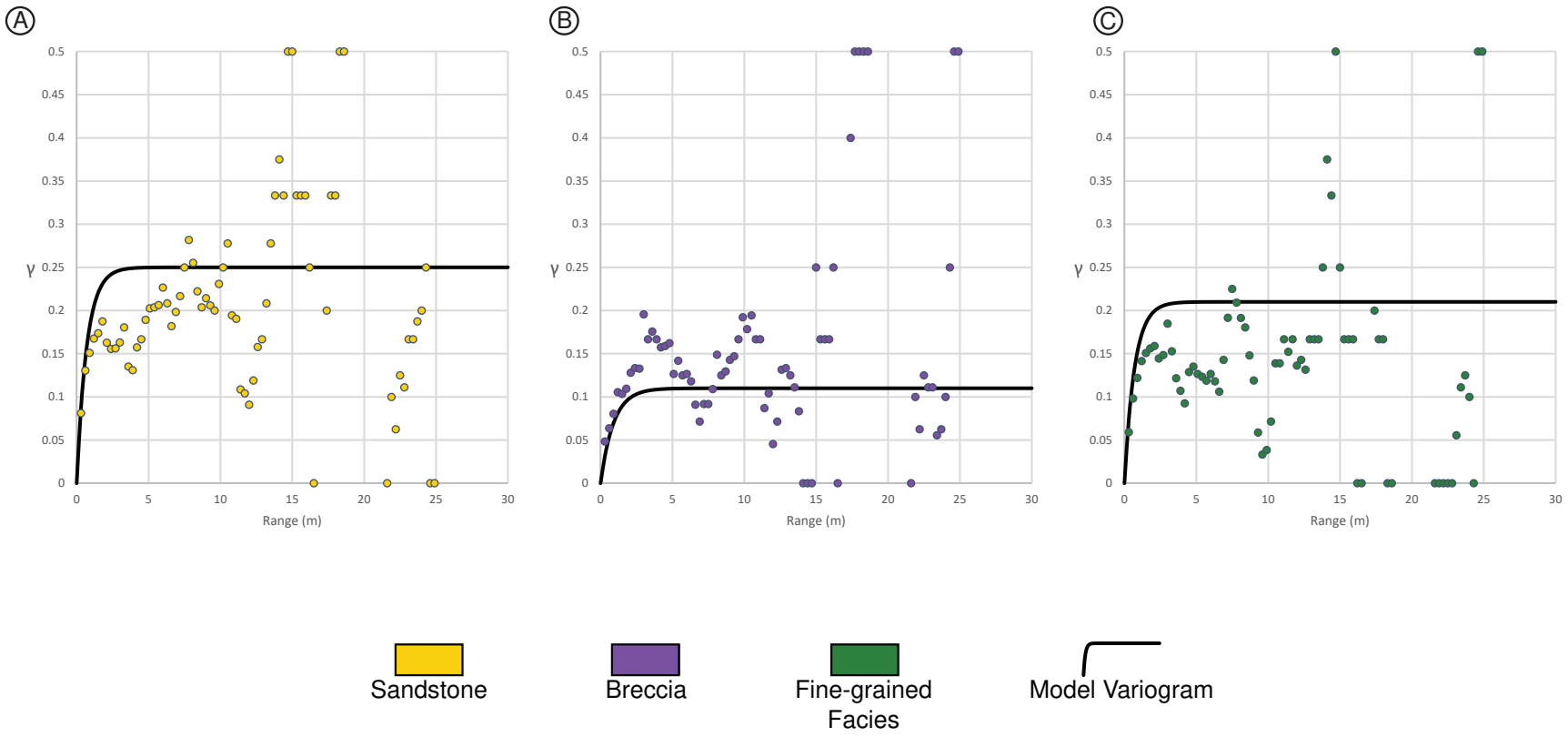

Figure 5.6: Vertical direction experimentally-fit variograms and exponential models: A.) sandstone experimental variogram and model B.) breccia experimental variogram and model, and C.) fine-grained facies variogram and model. Experimental variograms are modeled for 500 lags (0.3 m separation, 0.15 m tolerance) with 0° azimuth, 90° dip, 1° tolerance, 0.3 m bandwidth. Exponential models are detailed in Table 5.4 for 1-D experiments (Part 1b) and 5.7 for 3-D models (Part 2).

Only the vertical variograms models are considered in this 1-D experiment (Fig. 5.6, Table 5.4). Three vertical range cases test variogram range impacts: 1) the experimentally modeled range, 2) roughly half the experimentally modeled range, and 3) range of one cell (0.3 m thick) (Table 5.5).

Table 5.5: Part 1b: Outcrop-data 1-D Experiment Variogram Range Sensitivity Cases

Facies	Modeled Range	½ - Modeled Range	1-cell Range
Sandstone	2.1 m (7 cells)	1.2 m (4 cells)	0.3 m (1 cell)
Breccia	2.7 m (9 cells)	1.5 m (5 cells)	0.3 m (1 cell)
Fine-grained Facies	2.1 m (7 cells)	1.2 m (4 cells)	0.3 m (1 cell)

Two search ellipse cases test search neighborhood impacts: 1) a search ellipse equivalent to the longest facies variogram range in the test branch, and 2) a 9.3 m (i.e. 31-cell) search ellipse that encompasses the entire grid. Only SK was employed.

Seven different soft data cases test impacts of varying soft data weight, B_i. Recall that B_i is merely an input value and the modeler may use different values from the true B coefficient of the data set (See: 2B.4.1 Markov-Bayes Model of Co-regionalization). SIS, which does not consider soft data at all, was run as a base case. COSIS was run with five arbitrary B_i value sets and one B_i value set with the true B coefficients. The arbitrary cases employed the same B_i values for all facies incrementing from nearly 0 to nearly 1 at intervals of roughly 0.25 (Fig. 5.4). In other words, for cases labeled 0.99, each facies was run with $B_i = 0.99$, irrespective of the true B value. The true B coefficients for each facies were calculated as the difference in mean of correct classification vs. incorrect classification between the hard data and corresponding probability volumes (See: Stright, 2011) and simulations were parameterized with the facies-specific values (Table 5.6).

Table 5.6: Part 1b: Log 24 Facies Proportions and *B* Values

Facies	Facies Proportion	*B*
Sand	0.70	0.28
Breccia	0.06	0.22
Fine-grained Facies	0.23	0.40
Proportion-Weighted Average of *B* Values		*0.30*

For presentation purposes, this true *B* case is labeled as a single value, 0.3. This number is the facies proportion-weighted average of three *B* coefficients (Table 5.6).

5.1.3 Quantifying Results from 1-D Experiments

The ability of realizations to accurately reproduce a true facies distribution is examined with probability of misclassification. Probability of misclassification ($P_{misclass}$) examines how well facies realizations match expectations (Fig. 5.1A and Fig. 5.2C) given variable hard data data configurations, soft probability conditioning, and other parameters, where high misclassification values indicate the algorithm poorly reproduces the expectation.

This study calculates $P_{misclass}$ for suites of realizations with common parameters and data scenarios in the following way:

$$P_{misclass} = \frac{1}{n}\sum_{i=1}^{n}\left(1 - \frac{c}{r}\right) \qquad (Eq. 5.2)$$

where *n* is a set of evaluated cell locations (i.e., excluding active hard data cells), *c* is the number of times the correct facies is simulated at a given cell, and r is the number of realizations in question. $P_{misclass}$ can be applied to each facies individually, or for all facies at once. When applied to all facies at once, *n* is all unknown locations, **u**, and when applied to one facies, *n* refers to the subset of **u** where that particular facies actually occurs in the true facies distribution.

Fidelity of realizations to soft data is examined with Root Mean Squares Error (RMSE). An expected value model, or e-type, is developed for each facies, where each cell location

records the simulated facies proportion at that cell across all realizations (Pyrcz and Deutsch, 2014). This aggregate of realizations is compared to the prior model of the soft data with RMSE:

$$RMSE = \sqrt{\frac{1}{n}\sum_{i=1}^{n}(o-p)^2} \qquad (Eq. 5.3)$$

where *n* is a set of evaluated cell locations, *o* is the facies e-type value at a given cell (the "observed" value), and *p* is the facies soft data value at a given cell (the "predicted" value). RMSE is collected for each facies individually, and higher values indicate the algorithm poorly reproduces soft data.

$P_{misclass}$ was calculated for each facies individually as well as all at once to assess facies architecture reproduction. RMSE was calculated for each facies individually to assess fidelity to probability volumes.

5.2 Part 2: 3-Dimensional Experiment Methods

The full outcrop model grid comprises over 2.6 million active cells. In order to rapidly test multiple modeling methods and parameter schemes a small sector gridspace of just 112,345 active cells was extracted (Fig 4.1). As compared to the full model, which was 430 x 457 x 1,111 untruncated cells (i,j,k), the sector model is only 51 x 51 x 274 untruncated cells (i,j,k). Furthermore, while the full model is approximately 2 km^2, the sector model is 343 m x 343 m, or 0.12 km^2 (See: 4.1.2 Stratigraphic Framework). The sector contains three measured sections (Logs 15, 16, and 17; see Fig. 3.2) at the junction between the strike-parallel Red Deer River exposures and dip-parallel Willow Creek Canyon exposures. Modeling workflows were set up to test the sensitivity of resulting realizations to: 1) outcrop-inferred versus experimentally fit variograms (Part 2a and 2b), 2) facies proportions (Part 2a and 2b), and 3) soft data weights (Part 2a), and 4) LTR (Part 2b). 3-D experiments expand general 1-D findings for SIS and COSIS to

PGS and nested TGS. Please note, for comparative purposes, the nested TGS model was not re-run in the smaller sector space; the simulated facies data were extracted directly from the larger model (Fig.4.8) (Durkin, 2016).

5.2.1 3-D Sedimentary Variography

Sedimentary environments typically exhibit high anisotropy between facies variability up- and down-section (vertically) and along bedding (horizontally). Tabular deposits that exhibit the same facies 10s to 1000s of meters laterally can change facies in less than a meter vertically. As such, experimental variograms were assessed for each facies in the model separately for vertical (along vertical well sections) and horizontal (along architectural model layers) regimes. In this way, vertical and horizontal facies spatial correlation were decoupled. Sparse data causes difficult experimental variogram fitting, especially in the horizontal direction (Fig. 5.5, 5.6). For fine-grained facies (F3-F6), models were not fit individually due to the low proportion of these facies but aggregated into a single indicator category. These facies are depositionally and architecturally similar, so grouping them is reasonable.

SIS and COSIS simulations were generated with outcrop-inferred variograms (Table 4.3) as well as traditional experimentally fit variograms (Table 5.7) (See: 4.2.4 Variography and Nested TGS Model).

Table 5.7: Part 2: 3-D Modeling Experimentally fit Variogram Parameters

Facies	Model	Horizontal Range (m)	Vertical Range (m)	Sill (σ^2 - Normalized)
Sandstone	Exponential	55	2.1	1
Breccia	Exponential	40	2.7	1
All Others	Exponential	45	2.1	1

For PGS simulations, given difficulty fitting experimental variogram models from the hard data, a variety of ranges were used to assess outcrop character reproduction, while keeping the outcrop-inferred variogram ranges in mind. The previous work nested TGS simulation only employed outcrop-inferred variography (Table 4.3).

5.2.2 Part 2a: SIS and COSIS Experiments

3-D SIS and COSIS simulations evaluate impact of 1) soft data weight, and 2) outcrop-inferred versus experimentally fit variograms. These simulations connect 1-D experiments to 3-D modeling and serve as a reference frame for PGS and nested TGS results. Hard data comprises three wellbores and soft data is confined to the sector model area. However, global facies proportions are derived from all measured section data, not just the three sector model wellbores (Table 5.3).

Simulations were performed using: 1) outcrop-inferred variogram ranges (Table 4.3) and 2) experimentally fit variogram ranges (Table 5.7), both using exponential models. For each of the two variogram sets, one SIS simulation was run in addition to five COSIS simulations with B_i values: 0.01, 0.25, 0.5, 0.75, and 0.99 (Fig. 5.7). Ten realizations were run for each of the twelve simulations. Realizations were examined for qualitative outcrop architecture reproduction.

5.2.3 Part 2b: PGS Experiments

PGS realizations evaluated modeling impacts of: 1) variography, and 2) LTRs. The primary objective of PGS simulation was to improve upon previous nested TGS modeling (Fig 4.8). The hypothesis was that adding outcrop facies transition statistics with LTRs would improve facies architecture reproduction.

Two different "best-effort," LTRs (LTR A and LTR B) were devised to test the impact of compromising on certain facies transitions (Fig. 5.8). LTRs were designed holistically based on

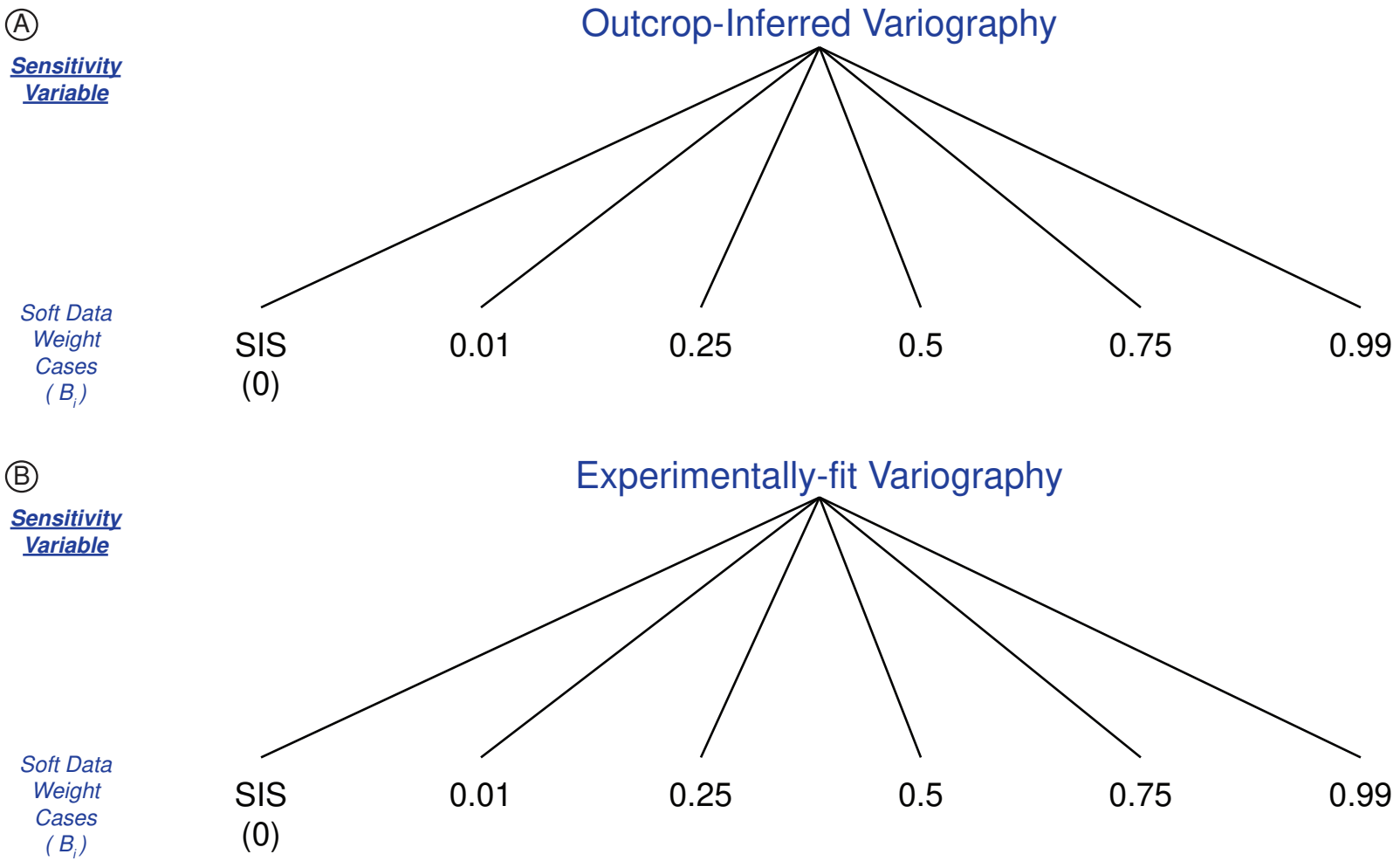

Figure 5.7: Part 2b: SIS & COSIS Test Tree. A) Outcrop-inferred variography tests SIS and five B_i values for COSIS. B) Experimentally-fit variography tests SIS and five B_i values for COSIS. Each of the twelve simulations was run for ten realizations.

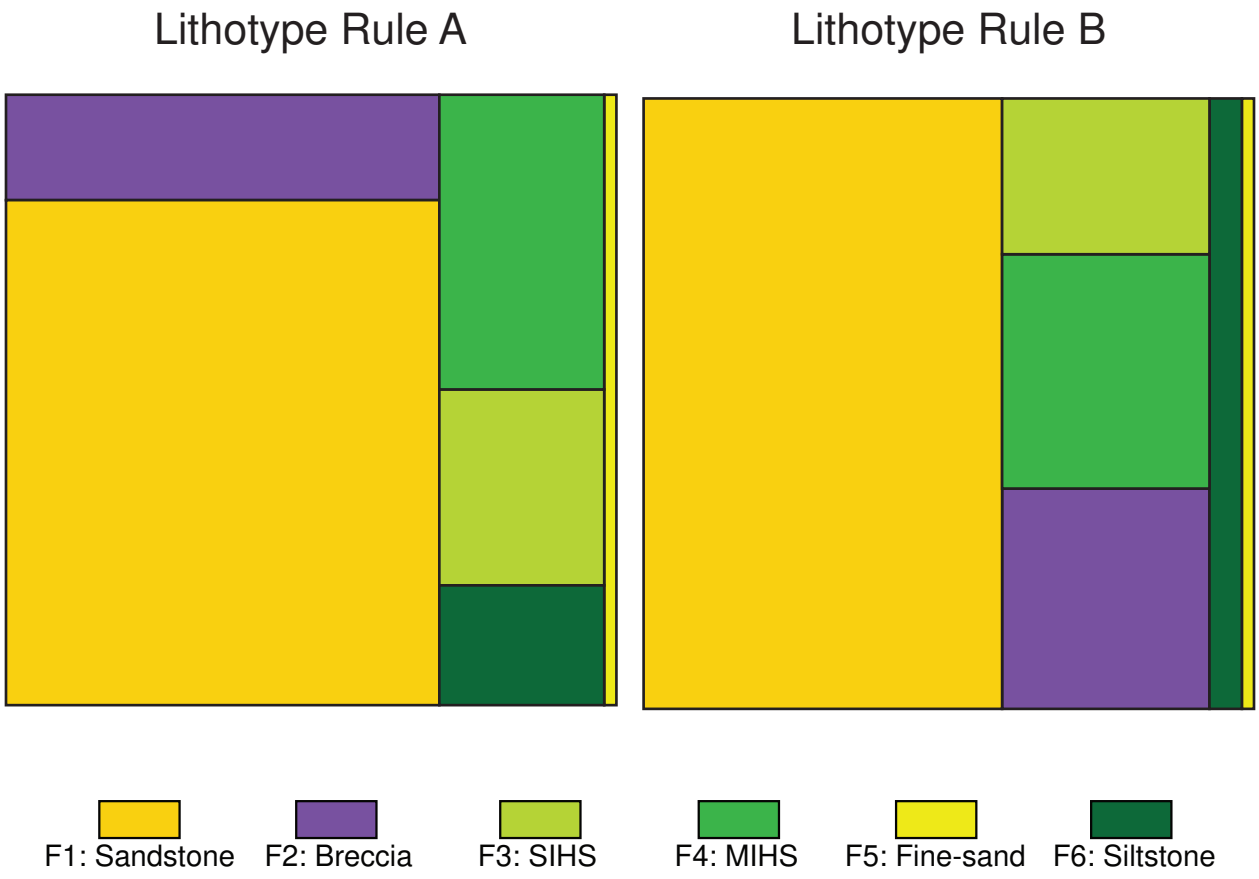

Figure 5.8: For PGS, complex facies-transition relationships must be simplified into Lithotype Rules (LTR) that enforce order of occurrence and transition between facies (e.g. in LTR A, Breccia must lie adjacent to Sand or MIHS). These LTR examples are symbolic of the mean probability of each facies' probability volume and correspondingly the true measured facies proportions.

transition probabilities (Fig. 4.3, 4.4; Table 4.1, 4.2). It is possible for each facies to outcrop next to any other with the exception of breccia and fine sandstone, which were not recorded adjacent to one another in the field. However, as 2-axis LTRs can only honor so many facies transitions, certain transitions were prioritized over others. When high transition probabilities were mutual between facies, that joint transition was prioritized. For example, sandstone transitions frequently to both MIHS and breccia, and both MIHS and breccia transitions frequently to sandstone (Fig. 4.3, 4.4; Table 4.1, 4.2). These mutual transitions were prioritized in the LTRs. Conversely, fine sandstone and siltstone exhibit relatively equitable transition rates to other facies, but other facies are unlikely to transition to fine sandstone or siltstone. As a result, transitions both to and from fine sandstone and siltstone were de-prioritized. On a relative basis, LTR A emphasizes sandstone-siltstone transitions at the expense of breccia transitions. On a relative basis, LTR B emphasizes breccia transitions at the expense of siltstone-sandstone transition, and completely de-prioritizes fine sandstone transitions.

Total results comprise 29 different parameter and data configurations of 4-10 realizations each. Several variogram regimes were tested, and because the sector model is 3-D, horizontal and vertical variogram ranges were tested separately. Horizontal variogram ranges were evaluated from 0 to 200 m at 50-m intervals. Vertical variogram ranges were evaluated from 0.3 to 1.2 m at 0.3-m intervals. Different variogram configurations were evaluated for both LTR A and LTR B (Fig. 5.9). Realizations were examined for qualitative outcrop facies architecture reproduction. Note that PGS, as implemented in Isatis (Geovariances, 2016), takes the input facies probability soft data and treats it as reliable local proportion information for use in simulations. As a result, this local proportion information, in aggregate, acts effectively as global facies proportion inputs. A consequence of using probabilities as proportions is that soft

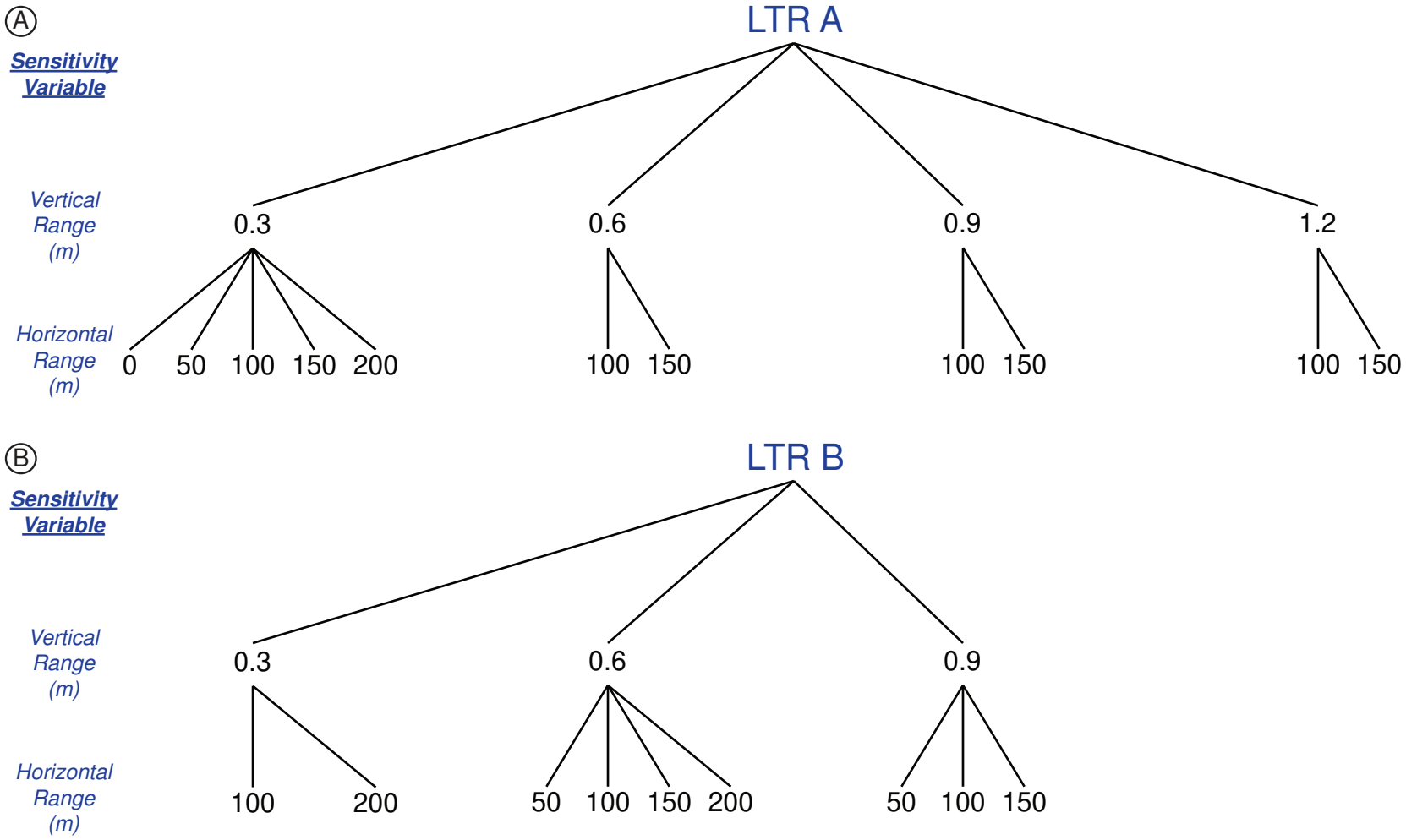

Figure 5.9: Part 2b: PGS Test Tree. A) LTR A tests four vertical variogram ranges at two to five horizontal variogram ranges. B) LTR B tests three vertical variogram ranges at two to four horizontal variogram ranges.

data weight cannot be changed as part of the algorithm workflow. If soft data is not perfectly reliable, it cannot be weighted as a parameter like B_i, but must be adjusted prior to modeling. Therefore, facies input proportions for these PGS experiments are equivalent to the average of the sector volume probabilities. These values are comparable to the facies proportions of the well logs (Table 5.3).

5.2.4 Assessing Facies Architecture Reproduction from 3-D Experiments

Facies architecture reproduction is difficult to summarize quantitatively. $P_{misclass}$ is limited in its ability to assess architecture reproduction because it is restricted to known, "true," hard data. Jackknife (Efron, 1982; Davis, 1987) and other related resampling procedures that can be measured with $P_{misclass}$: 1) only assess realization deviation from the sample mean and variance, and 2) cannot evaluate geologic essence in a holistic or gradational way. Realization data away from wellbores remains difficult to certify. If soft data is a strongly representative of facies architecture, RMSE from soft data can measure fidelity to that essence in a gradational way, but this may be risky given the inherent ambiguity in soft data. Multiple-point density function analysis of outcrop data versus realizations may prove useful, but there are inherent uncertainties relating 2-D and 1-D field data to 3-D realizations (Boisvert et al., 2007, 2010). This study employs a graphical method that compares discrepancies in the hard data-soft data relationship at each cell for both input well data and realizations. The assumption being that if input data and realizations produce similar discrepancies, facies architecture is better reproduced.

Consider the outcrop hard data. For a given facies, cells are sorted by probability and binned. Then, hard data facies likelihood is calculated for each bin. Probability bins are plotted on the x-axis and facies likelihood is plotted on the y-axis (Fig. 5.10). In other words, for cells in facies probability bin, x, the actual hard data facies percentage is y. Ideally, facies likelihood

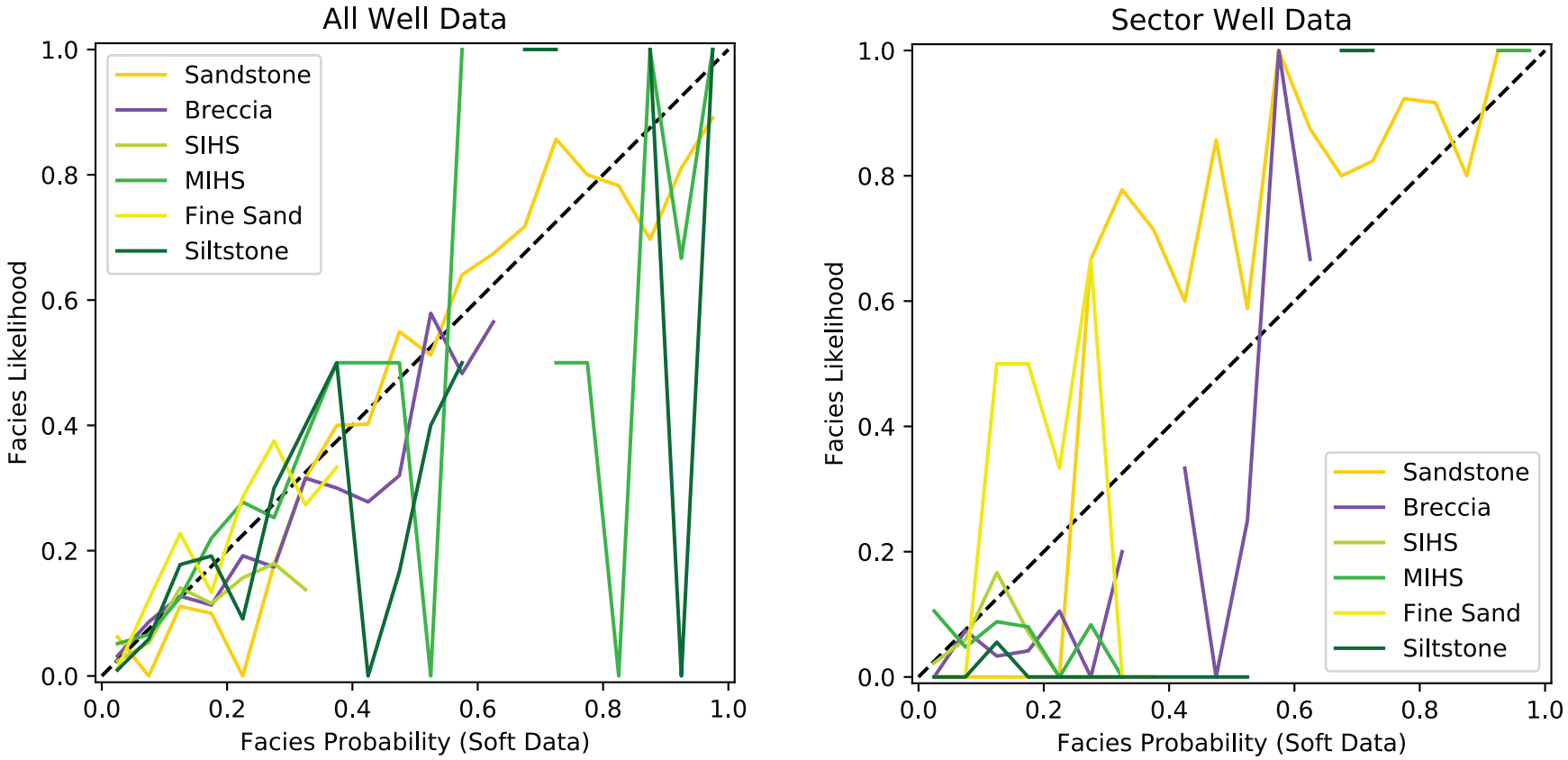

Figure 5.10: For well data, binned facies soft data probability is plotted on the x-axis and co-located binned hard data facies percentages are plotted on the y-axis. For cells with facies soft data probability range, y, the actual hard data percentage for that facies at those cells is y.

would be the same as probability and would plot on the 1:1 line. In this sense, these plots are a rough graphical proxy for *B*, where excursions from the 1:1 line show the discrepancies between hard and soft data. The assumption is that these discrepancies are meaningful facies architecture signals and that reproducing them is desirable. These facies likelihood vs. probability plots can also be generated for realizations. If the realization plots tracks the well plots, then the architectural signal in the hard data is successfully transmitted to the realization.

5.3 Hard Data Sparsity Context for Experiments

It is important to contextualize the relative data sparsity of the various experimental and modeling frameworks in this study, especially as compared to real-world petroleum industry data sets. Excepting unconditional models, which have no hard data, the 1-D outcrop-data experiments (Part 1b) have a minimum of 1 hard data cell per 31 cells in the entire grid, or 3.2% hard data. In the original full model (Durkin, 2016), there are 1297 hard data cells in a ~2.5 million cell volume, or 0.05% hard data. The sector model (Part 2) has 201 hard data cells in 112,345 cell volume, or 0.18% hard data. The 1-D experiments are not only simpler than the 3-D models, they have much more data; this is an important caveat to their respective performance.

Durkin's 35 measured sections are spread over an area of roughly 2 km^2, or ~494 acres, which yields an average well-spacing of ~15 acres. This is relatively dense, but even modern onshore oil and gas fields have been drilled at tighter spacing (e.g., 6-8 acres), especially when reservoir heterogeneity is high (Clark et al., 1944; Miall, 1988; Tucker et al., 1998; Pranter and Sommer, 2011). These experiments and models are fine-scale, but still relevant to industry practice.

CHAPTER 6: RESULTS WITH INTERPRETATIONS

Results are presented in the same fashion as the preceding methods section and annotated by part. 1-D synthetic and outcrop-data experiments (Part 1) are reviewed first, followed by 3-D sector comparative algorithm work (Part 2). Interpretations are included immediately following results to drive home their important aspects, as each part is a related, but stand-alone experimental set. The following discussion section then synthesizes the part interpretations with respect to their broader ramifications. For the purposes of this work, low-proportion facies are less than 20%, moderate-proportion facies are 20-50% and high-proportion facies are greater than 50%.

6.1 Part 1: 1-Dimensional Results

6.1.1 Part 1a: Synthetic 2-Facies Results

The pure SIS control run of 100 realizations with SK is considered first (Fig. 6.1A). All 100 realizations are visualized at once to capture the full spectrum of individual outcomes as well as their aggregate character in concert; cell number is indicated on the y-axis and realization number is indicated on the x-axis. No structure or architecture is discernable, but, in aggregate, the facies percentages are correctly reproduced and $P_{misclass}$ is relatively low (0.34).

In total, COSIS results, comprise 44 simulation scenarios of 100 realizations for a total of 4,440 model runs (Appendix). Selected SK and OK realizations highlight B values: 0.3, 0.6, 0.98 and -0.6, or weakly informative, moderately informative, strongly informative, and moderately incorrectly informative soft data, respectively (Fig. 6.1B-E, 6.2). All realizations are visualized at once in the same manner as the SIS control run.

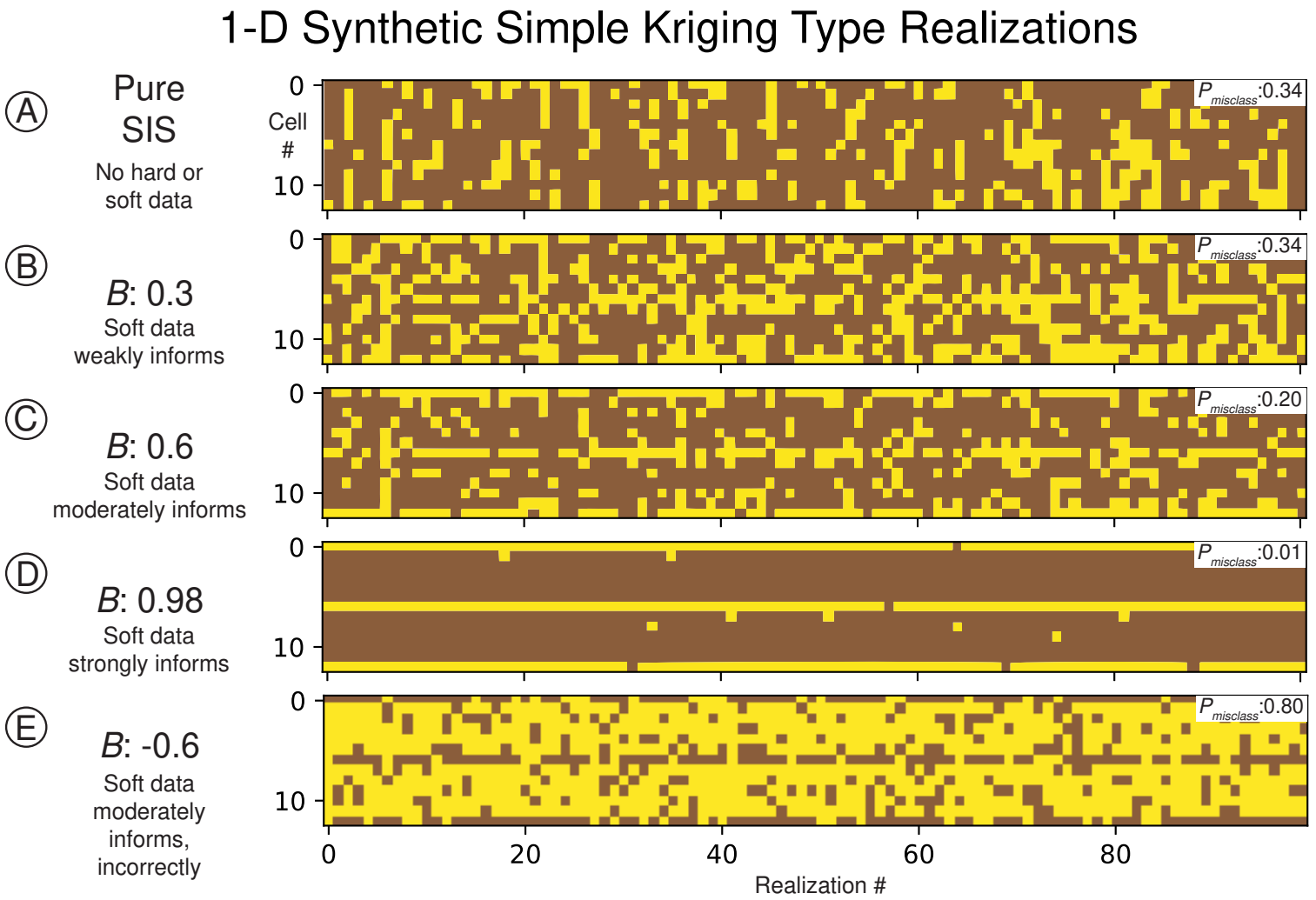

Figure 6.1: Selected 1-D 2-Facies Synthetic Experiment SK realizations. A) Pure SIS control run, B) $B = 0.3$; weakly informative soft data, C) $B = 0.6$; moderately informative soft data, D) $B = 0.98$; strongly informative soft data, and E) $B = -0.6$ moderately incorrectly informative soft data. All realizations are visualized at once. Lower B values produce realizations with less fidelity to outcrop, given higher misclassification with respect to the true facies distribution.

1-D Synthetic Ordinary Kriging Type Realizations

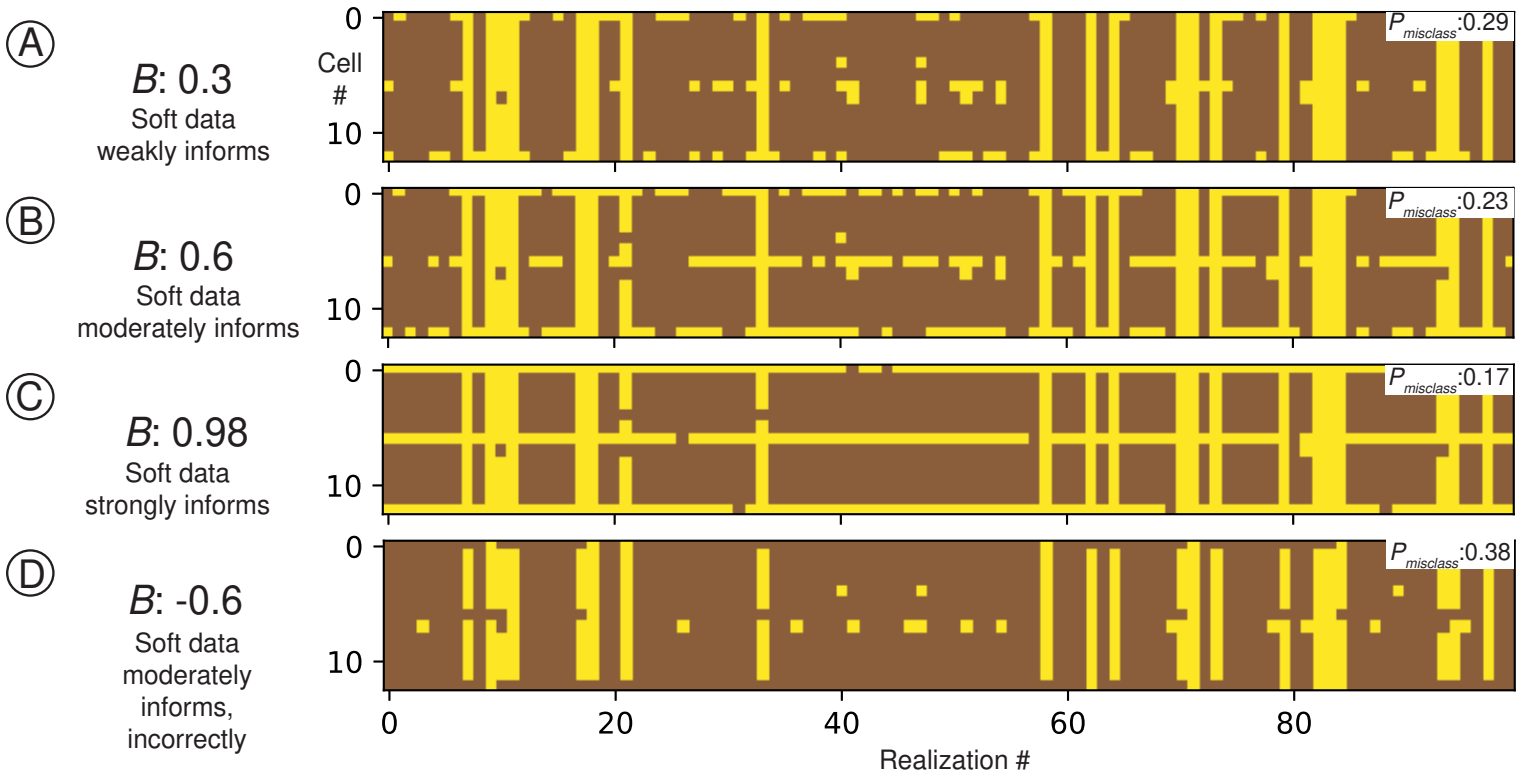

Figure 6.2: Selected 1-D 2-Facies Synthetic Experiment OK realizations. A) B = 0.3; weakly informative soft data, B) B = 0.6; moderately informative soft data, C) B = 0.98; strongly informative soft data, and D) B = -0.6 moderately incorrectly informative soft data. All realizations are visualized at once. Lower B values produce realizations with less fidelity to outcrop, given higher misclassification with respect to the true facies distribution.

Qualitatively, SK realizations in the same scenario distribute facies error more evenly throughout each realization and the aggregate appears more homogenous. OK realizations in the same scenario often drastically overrepresent one facies or another; realizations exhibit starkly different character from one to the next. When the soft data is made less reliable (i.e., B is reduced) the true facies distribution pattern becomes decreasingly discernable in the aggregate of realizations. When the soft data is made more distinct, but incorrect, (i.e., B is greater magnitude but negative) the facies anti-distribution becomes increasingly discernable in the aggregate of realizations. That is, true facies distribution sand cells are simulated as shale, and shale cells are simulated as sand. This reversal is much more obvious with SK than OK.

Quantitative inspection of $P_{misclass}$ as a function of sand probability and corresponding B value, confirms qualitative observations (Fig. 6.3). When B is close to 1 (i.e., facies probabilities are distinct and correct), $P_{misclass}$ is low. As B approaches 0 (i.e, facies probabilities are indistinct), $P_{misclass}$ increases. As B approaches -1 (i.e., facies probabilities are distinct and incorrect) $P_{misclass}$ grows even higher. SK COSIS is vastly more sensitive to changes in facies probability than OK. When B is high and positive, SK outperforms OK. However, OK appears to drastically outperform SK in all other cases, even when B is strongly negative. SK SIS, which is completely insensitive to soft data, plots at the same $P_{misclass}$ as OK COSIS with near-perfectly indistinct soft data.

6.1.2 Part 1a: Synthetic 2-Facies Interpretations

In this experiment, soft data is trusted completely and thus weighted fully ($B_i \approx 1$), but the actual soft data reliability (B) varies with each scenario. The result is that soft data reliability is inversely related with $P_{misclass}$ (Fig. 6.3). In other words, when soft data is uninformative or incorrect, facies misclassification is high and the true facies distribution is not reproduced. This

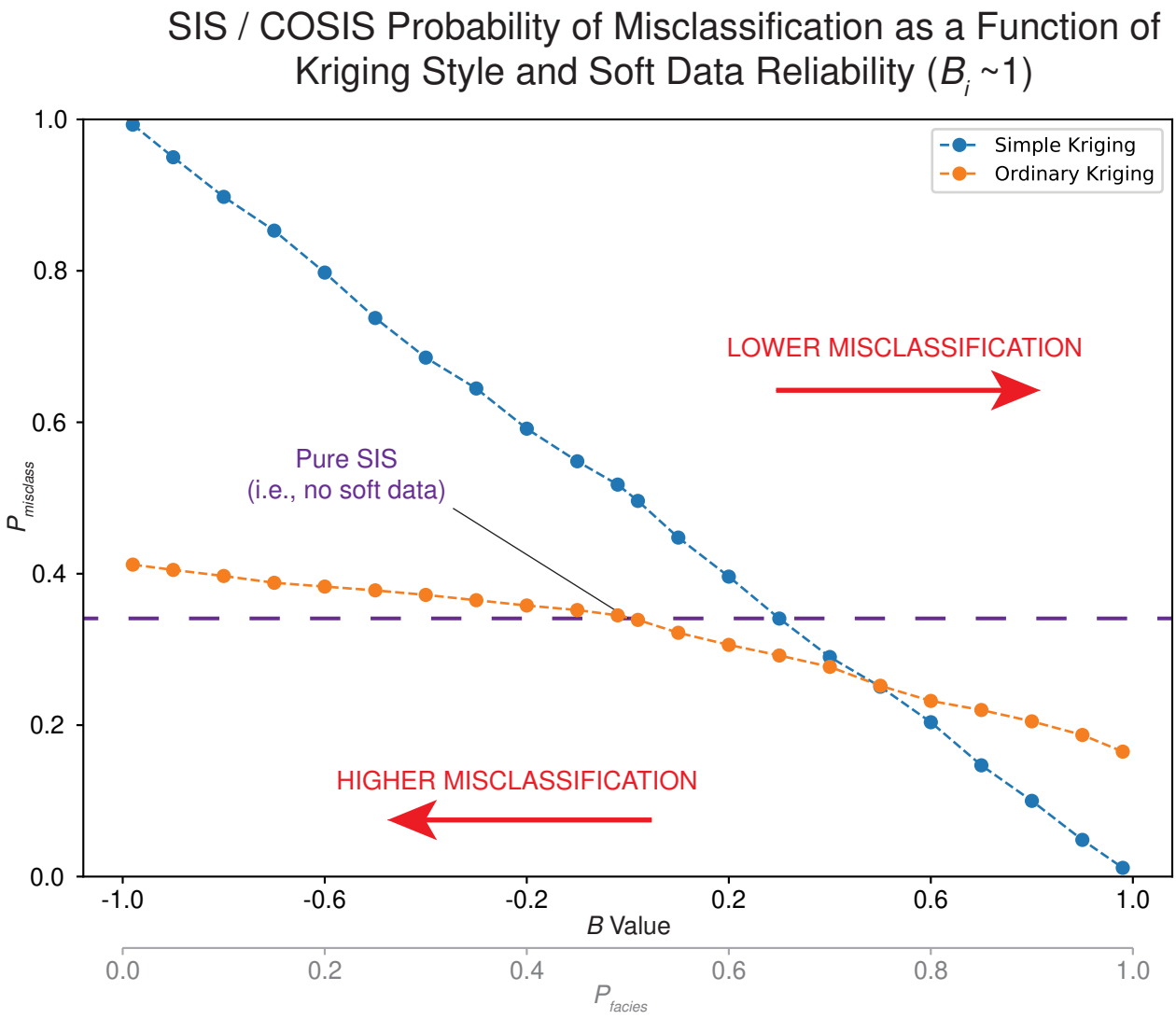

Figure 6.3: For a B_i = ~ 1.0 (i.e., fully trusting the information content of soft probabilities) decreasing soft data reliability is linearly correlated to the probability of misclassification of sand. Conceptually, this relates back to seismic resolvability of thin beds. Whether a given facies is high-proportion or not, if it is not distinct in the soft data, it will be of little aid in guiding modeling. Simple Kriging appears to be a better predictor of facies than Ordinary Kriging when soft data is reliable (i.e. facies are highly distinct), but is a weaker predictor of facies when soft data is less reliable.

implies that, irrespective of facies proportion, if facies are not distinct in the soft data, then soft data will be of little aid in guiding modeling. Conceptually, this relates back to seismic resolvability of thin beds (Widess, 1973; Zeng, 2009). While well log hard data may indicate interbedded thin sands and shales and provide strong reservoir proportion controls, seismic-derived soft data may not distinguish the two facies. Indistinct thin beds yield low-reliability soft data, which is of limited modeling utility. SK appears to be a better predictor of facies than OK when facies are highly distinct, but is a weaker predictor of facies when soft data is indistinct or incorrect (Fig. 6.3).

As OK is less responsive to soft data than SK generally (See: 2B.2 Kriging), it could be expected that SK would benefit from more reliable soft data as compared to OK. However, it was unexpected that the corollary would be true: that OK would perform markedly better with unreliable soft data. This is even more unexpected in light of the fact that so many of the OK realizations are qualitatively unacceptable (i.e., 100% sand or shale) (Fig. 6.3). However, given that OK de-emphasizes soft data, it follows that OK will perform relatively better when soft data is weakly informative or incorrect. Model inputs of $B_i \approx 1$ over-weights soft data in the vast majority of cases; OK corrects this inadvertently. COSIS with SK is theoretical best practice for facies indicator simulation (i.e., as opposed to COSIS with OK). When B values are low, however, incorporating soft data with SK appears to be counterproductive. This is further highlighted by the fact that pure SIS, which does not consider soft data at all, also outperforms SK when B is below 0.3, on the basis of $P_{misclass}$. It is important to consider that accuracy in these cases only occurs when assessed over multiple realizations. Ranking realizations or excising problematic ones could significantly change modeling takeaways and interpretations

(e.g., removing all OK models with ~100% sand or shale). Ultimately, if soft data is unreliable, COSIS with SK may not be advantageous.

6.1.3 Part 1b: 3-Facies Outcrop-Data Results

The two search ellipses tested produce indiscernible results. Therefore, all results shown and discussed herein were generated with the unrestricted all-data search ellipse and SK (Fig. 5.4). Results are framed in terms of difference from the experimentally fit variogram range (i.e., the longest-range parameter set) (Fig. 5.4). This is a reasonable starting point from which to compare other 3-facies 1-D results: the variogram ranges are fit from the hard data directly (Table 5.4, Fig. 5.6). An example type configuration presents the following information: hard data percentage, *B* value, Log 24 true facies distribution, the hard data input, ten realizations, Log 24 soft data, the realization e-type, a $P_{misclass}$ graph for all facies, and an RMSE table (Fig. 6.4). This type configuration exhibits modeling outcomes given: 1) minimal hard data input, 2) a calibrated *B* value for soft data weight input, 3) variography experimentally fit directly from outcrop hard data, and 4) an unrestricted search ellipse. The type configuration is compared to other configurations with the same hard data scenarios for context. Hard data percentage is varied to produce different $P_{misclass}$ results with soft data weights: $B_i \approx 0.3$ (Fig. 6.5) and $B_i = 0.75$ (Fig. 6.6). Soft data weight (B_i) is varied to produce different RMSE results with hard data percentages: ~3% (Fig. 6.7) and ~25% (Fig. 6.8). Additionally, summary figures were generated for all 6,552 hard data and parameter configurations (Appendix).

Hard data impacts are summarized with plots of $P_{misclass}$ as a function of hard data percentage given a common: a) search ellipse and b) soft data weight (B_i). Hard data plot groups are provided for: 1) the experimentally modeled range (Fig. 6.9), 2) roughly half the

Type Configuration: 3.23 % Hard Data, B_i: 0.3, *All-data Search Ellipse, SK
Ranges: Sand = 2.1 m (7 cells), Breccia = 2.7 m (9 cells), Fine-grained = 2.1 m (7 cells); 100 realizations

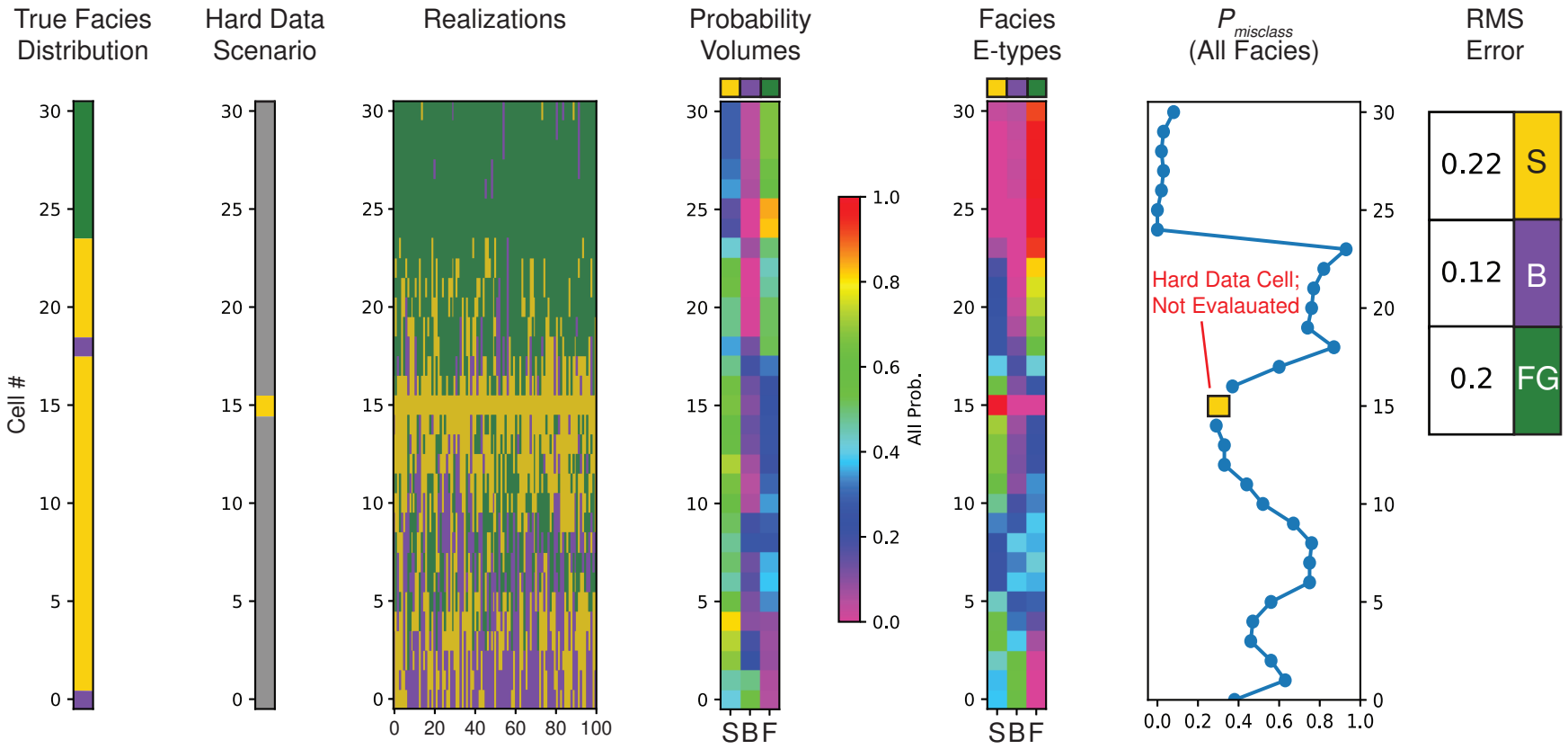

Figure 6.4: Part 1b: 3-Facies Outcrop-Data Results - Type Configuration Realizations and Summary Charts. For dozens of parameterizations of each hard data scenario, hundreds of SIS realizations were automated with SGeMS. RMSE data was collected by comparing an E-Type for each facies to the probability volume, and $P_{misclass}$ was calculated from the true facies distribution. Each is a proxy for realization fidelity to soft and hard data, respectively. **0.3* soft data weights are detailed in Table 5.6.

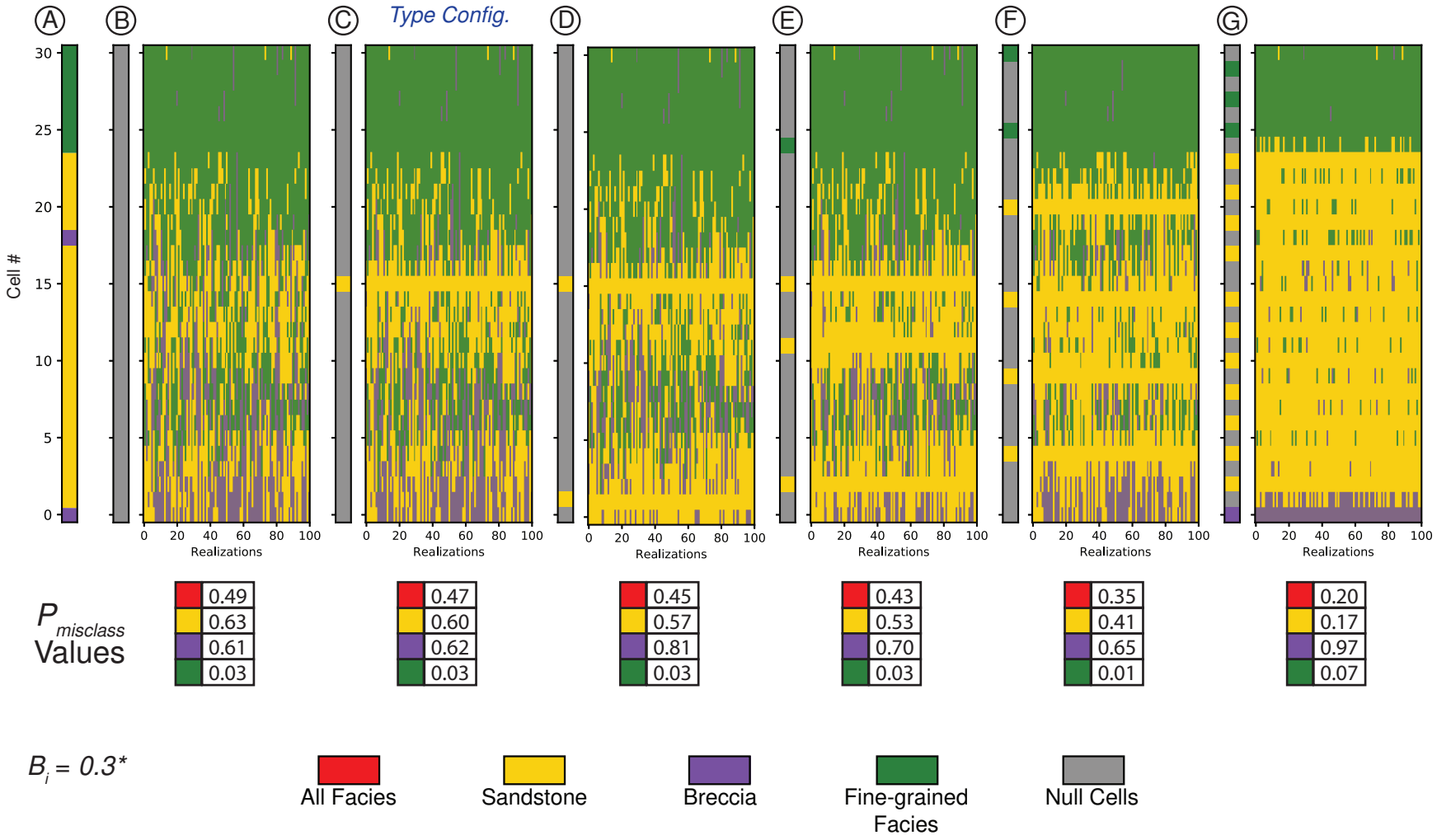

Figure 6.5: Part 1b: 3-Facies Outcrop-Data Results - Example realizations and $P_{misclass}$ for experimentally-fit variography, the unrestricted search ellipse, and soft data weight, B_i, of *0.3** given varying hard data % with SK. A) True facies distribution. B - G) Hard data scenario and COSIS realizations for hard data %: ≈ 0, 3, 6, 13, 25, and 50, respectively, where C is the type configuration from Fig. 6.4. These example realizations are also represented in associated plotted points in Fig. 6.9D. **0.3* soft data weights are detailed in Table 5.6.

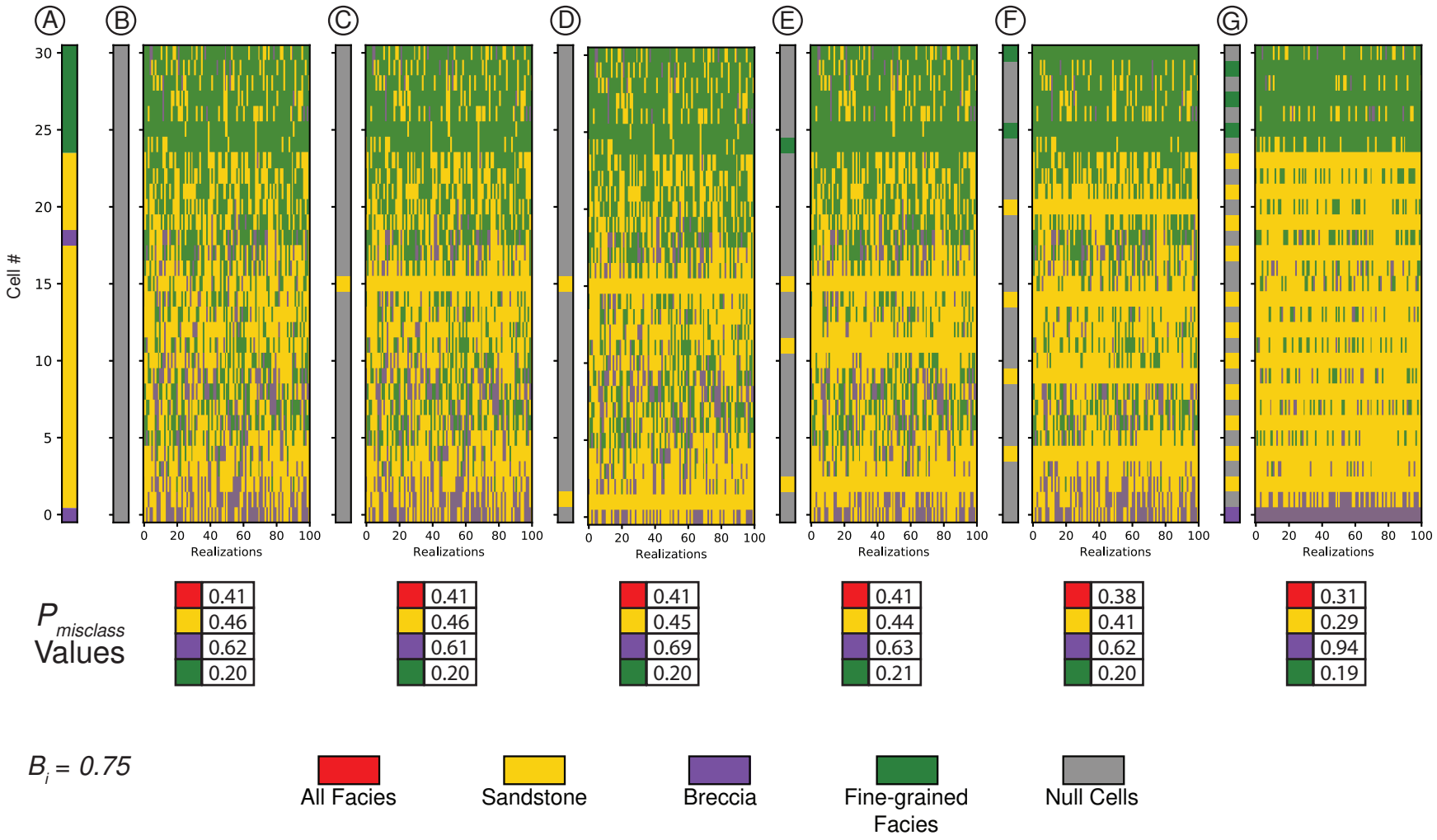

Figure 6.6: Part 1b: 3-Facies Outcrop-Data Results - Example realizations and $P_{misclass}$ for experimentally-fit variography, the unrestricted search ellipse, and soft data weight, B_i, of *0.75* given varying hard data % with SK. A) True facies distribution. B - G) Hard data scenario and COSIS realizations for hard data %: ≈ 0, 3, 6, 13, 25, and 50, respectively. These example realizations are also represented in associated plotted points in Fig. 6.9F.

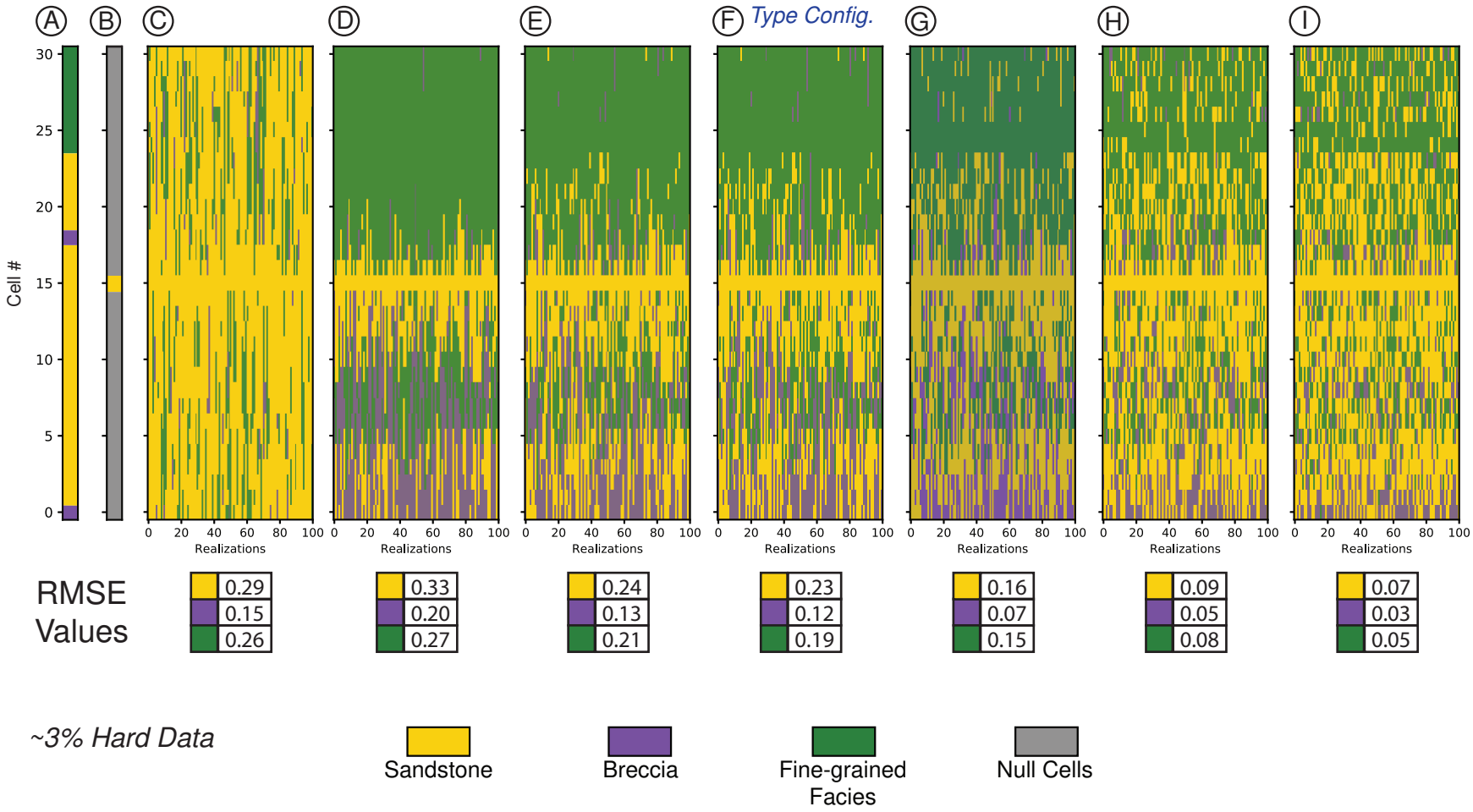

Figure 6.7: Part 1b: 3-Facies Outcrop-Data Results - Example realizations and RMSE for experimentally-fit variography, ~3% hard data, and the unrestricted search ellipse given varying soft data weight, B_i with SK. Only one hard data % scenario is shown for each soft data weight. A) True facies distribution. B) Hard data scenario. C) SIS realizations. D - I) COSIS realizations for soft data weights: 0.01, 0.25, *0.3**, 0.5, 0.75, and 0.99, respectively, where F is the type configuration from Fig. 6.4. These example realizations are also represented in associated plotted points in Fig. 6.10B. **0.3* soft data weights are detailed in Table 5.6.

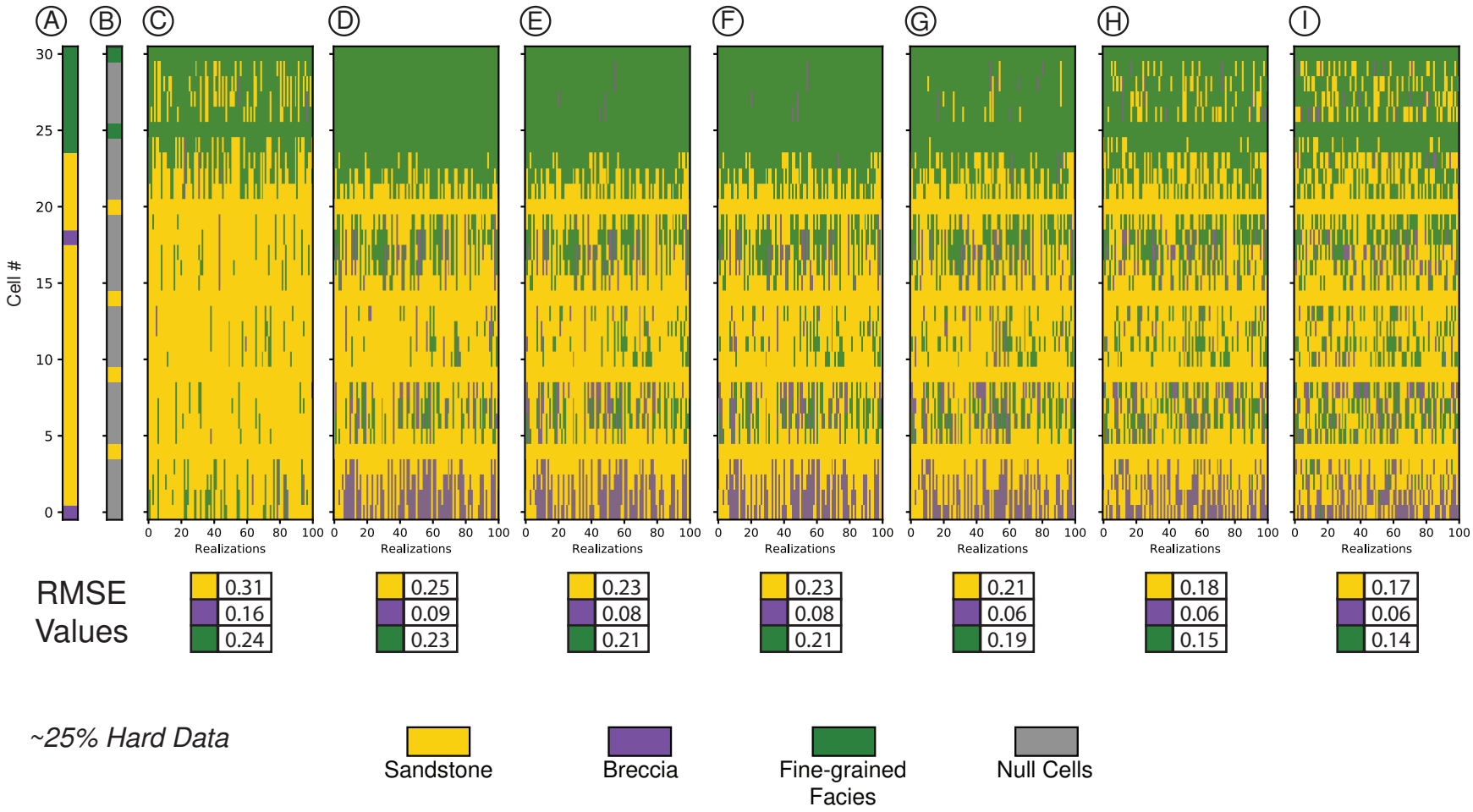

Figure 6.8: Part 1b: 3-Facies Outcrop-Data Results - Example realizations and RMSE for experimentally-fit variography, ~25% hard data, and the unrestricted search ellipse given varying soft data weight, B_i with SK. Only one hard data % scenario is shown for each soft data weight. A) True facies distribution. B) Hard data scenario. C) SIS realizations. D - I) COSIS realizations for soft data weights: 0.01, 0.25, *0.3**, 0.5, 0.75, and 0.99, respectively. These example realizations are also represented in associated plotted points in Fig. 6.12E. **0.3* soft data weights are detailed in Table 5.6.

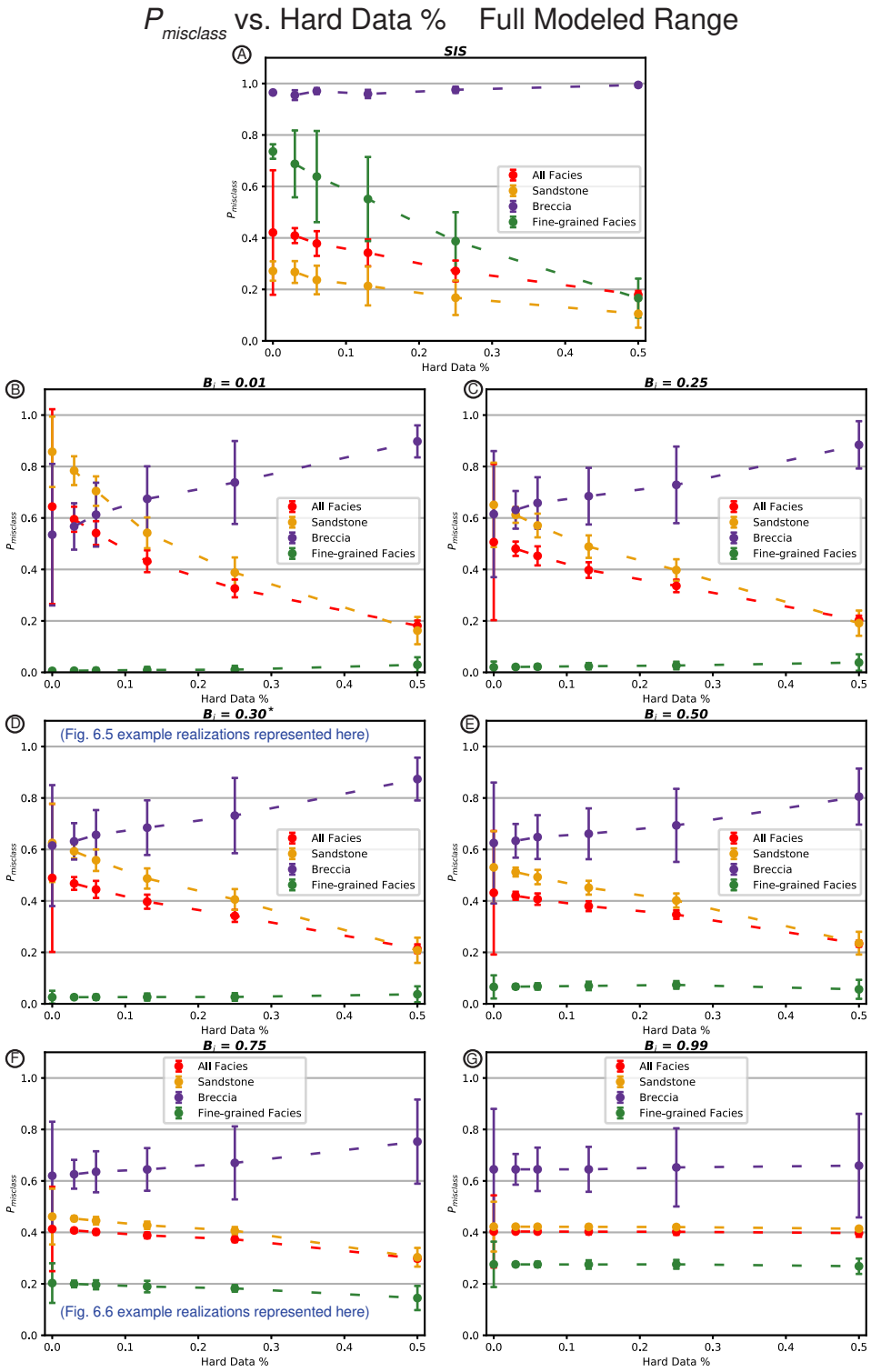

Figure 6.9: Part 1b: 3-Facies Outcrop-Data Results - Experimentally fit $P_{misclass}$ vs. Hard Data %. Variography is fit experimentally from outcrop hard data and SK is used. Sandstone, breccia and fine-grained ranges are 2.1, 2.7, and 2.1 m respectively (7, 9, and 7 cells). Search ellipse encompasses all data. A) SIS results. B - G) COSIS results where B_i = 0.01, 0.25, 0.3*, 0.5, 0.75, and 0.99, respectively. **0.3* soft data weights are detailed in Table 5.6.

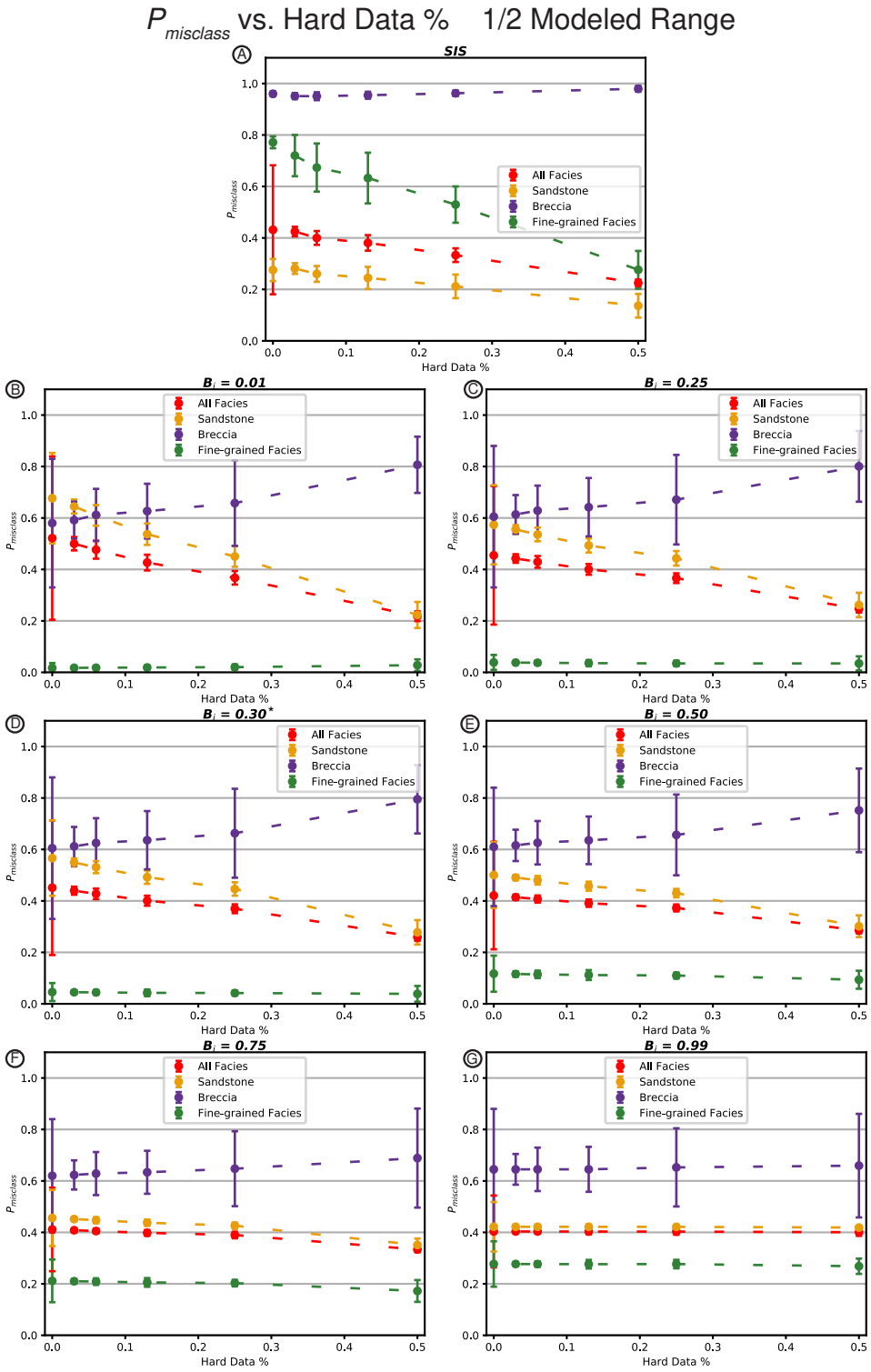

Figure 6.10: Part 1b: 3-Facies Outcrop-Data Results - "1/2 Range" $P_{misclass}$ vs. Hard Data %. Variography is half the experimentally fit range. Sandstone, breccia and fine-grained ranges are 1.2, 1.5, and 1.2 m respectively (4, 5, and 4 cells). SK is used and search ellipse encompasses all data. A) SIS results. B - G) COSIS results where B_i = 0.01, 0.25, 0.3*, 0.5, 0.75, and 0.99, respectively. **0.3* soft data weights are detailed in Table 5.6.

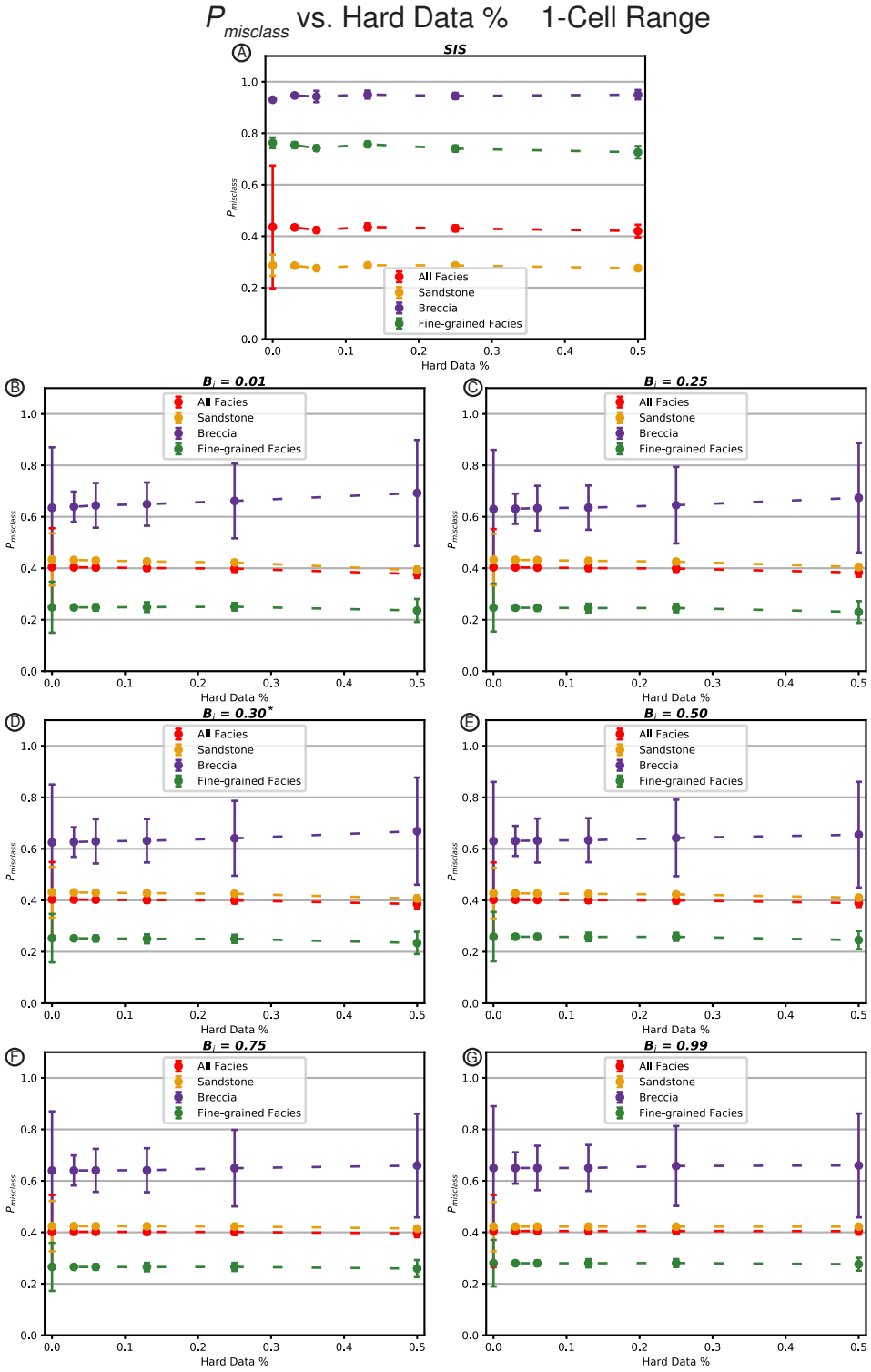

Figure 6.11: Part 1b: 3-Facies Outcrop-Data Results - "1-cell Range" $P_{misclass}$ vs. Hard Data %. Sandstone, breccia and fine-grained ranges are all 0.3 m (1 cell). SK is used and search ellipse encompasses all data. A) SIS results. B - G) COSIS results where B_i = 0.01, 0.25, 0.3*, 0.5, 0.75, and 0.99, respectively. **0.3* soft data weights are detailed in Table 5.6.

experimentally modeled range (Fig. 6.10), and 3) range of one cell (0.3 m thick) (Fig 6.11). Soft data impacts are summarized in plots of RMSE as a function of soft data weight given a common: a) search ellipse and b) hard data percentage. Soft data plot groups are provided for: 1) the experimentally modeled range (Fig. 6.12), 2) roughly half the experimentally modeled range (Fig. 6.13), and 3) range of one cell (0.3 m thick) (Fig 6.14).

Consider the hard data results for experimentally fit variography (Fig. 6.9). For SIS (Fig. 6.7A), as hard data percentage increases, $P_{misclass}$ steadily decreases, except for low-proportion breccia, which stays unchanged. For COSIS, the overall trend is similar, except that $P_{misclass}$ of low-proportion breccia increases at higher hard data percentage and $P_{misclass}$ of fine-gained facies remain relatively unchanged (Fig. 6.9B-G). For sandstone and the system as a whole, increasing soft data weight reduces $P_{misclass}$ for low and moderate hard data percentage, but increases $P_{misclass}$ at high hard data percentage (e.g., compare Fig. 6.9B and G). For breccia, increasing soft data weight has minimal impact at low hard data percentage, but reduces $P_{misclass}$ for moderate and high hard data percentage (e.g., compare Fig. 6.9B and G). For fine-grained facies, increasing soft data weight increases $P_{misclass}$ for all hard data percentage. At higher soft data weight, realizations are less sensitive to increasing hard data percentage.

Consider the soft data results for experimentally fit variography (Fig. 6.12). Increasing soft data weight reduces RMSE for all COSIS cases. For low soft data weight, initial increase in hard data percentage reduces RMSE (e.g,. compare Fig. 6.12B and 6.12D), but as higher hard data percentage levels, RMSE increases, and the beneficial impact of increasing soft data weight is diminished (e.g., compare Fig. 6.12B and 6.12F). For moderate and high soft data weight, the dynamic is simpler: increasing hard data percentage increases RMSE (e.g., compare Fig. 6.12B

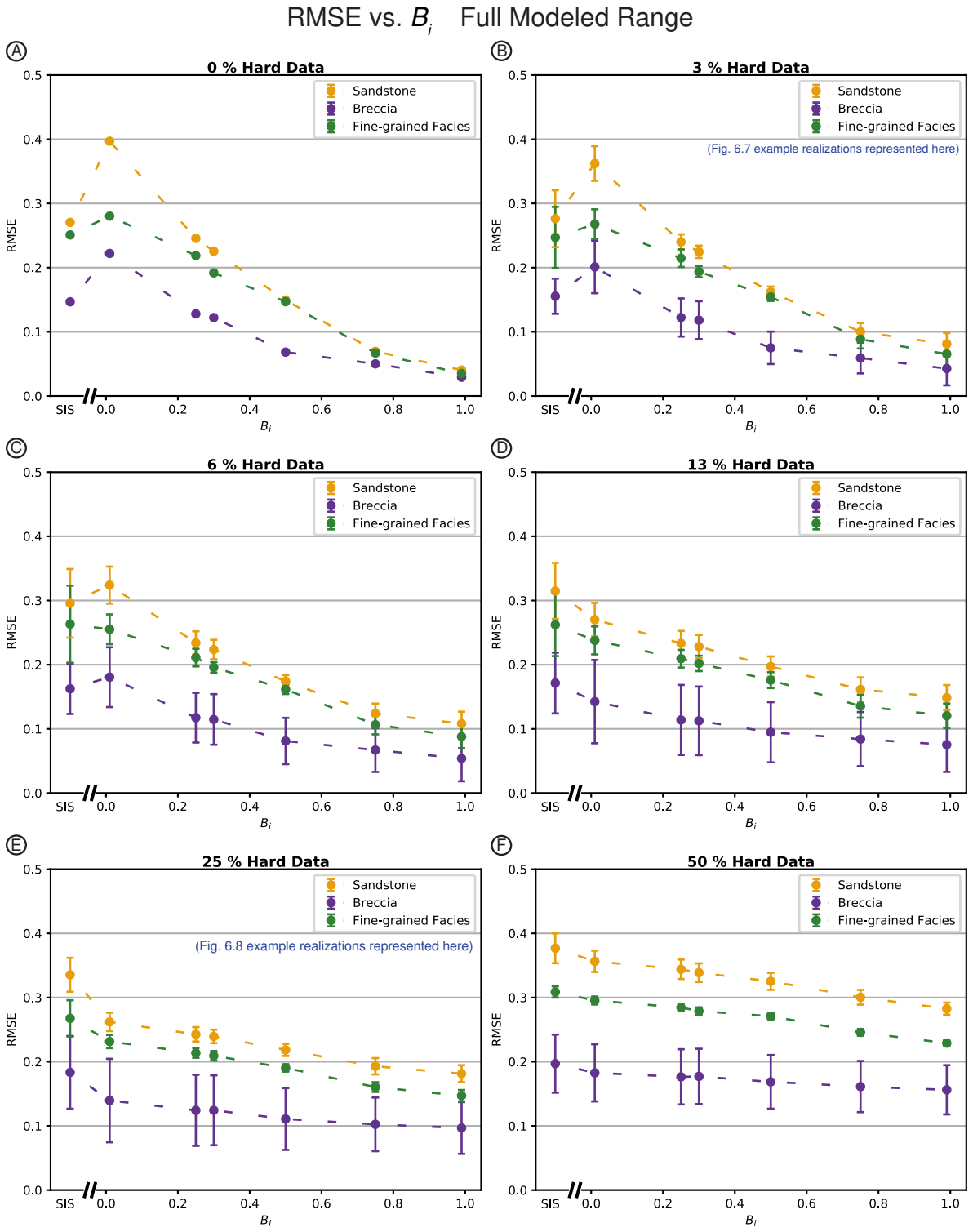

Figure 6.12: Part 1b: 3-Facies Outcrop-Data Results - Experimentally fit RMSE vs. B_i. Variography is fit experimentally from outcrop hard data. Sandstone, breccia and fine-grained ranges are 2.1, 2.7, and 2.1 m respectively (7, 9, and 7 cells). SK is used and search ellipse encompasses all data. A - F) Results where hard data % ≈ 0, 3, 6, 13, 25, and 50, respectively.

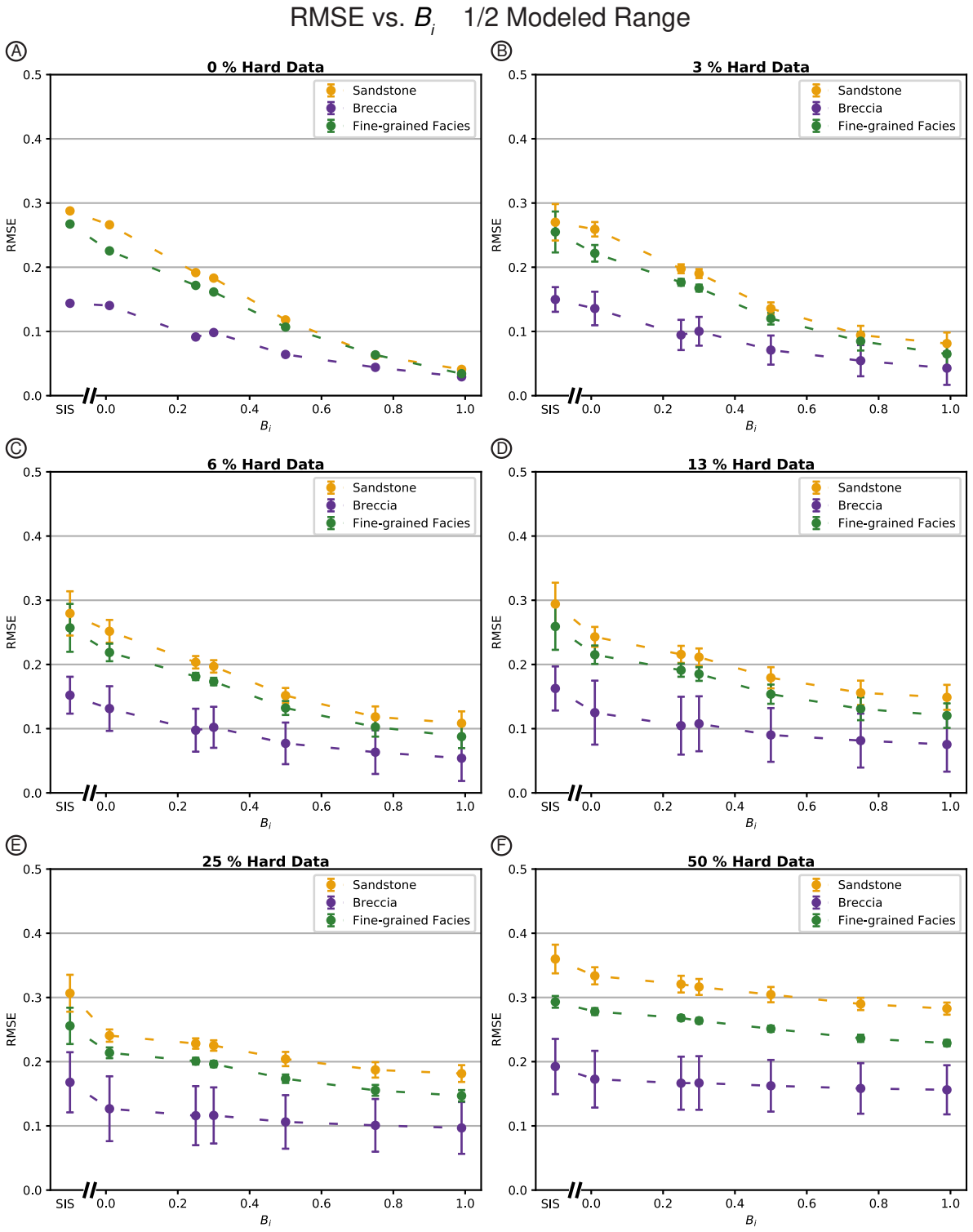

Figure 6.13: Part 1b: 3-Facies Outcrop-Data Results - "1/2 Range" RMSE vs. B_i. Variography is half the experimentally fit range. Sandstone, breccia and fine-grained ranges are 1.2, 1.5, and 1.2 m respectively (4, 5, and 4 cells) SK is used and search ellipse encompasses all data. A - F) Results where hard data % ≈ 0, 3, 6, 13, 25, and 50, respectively.

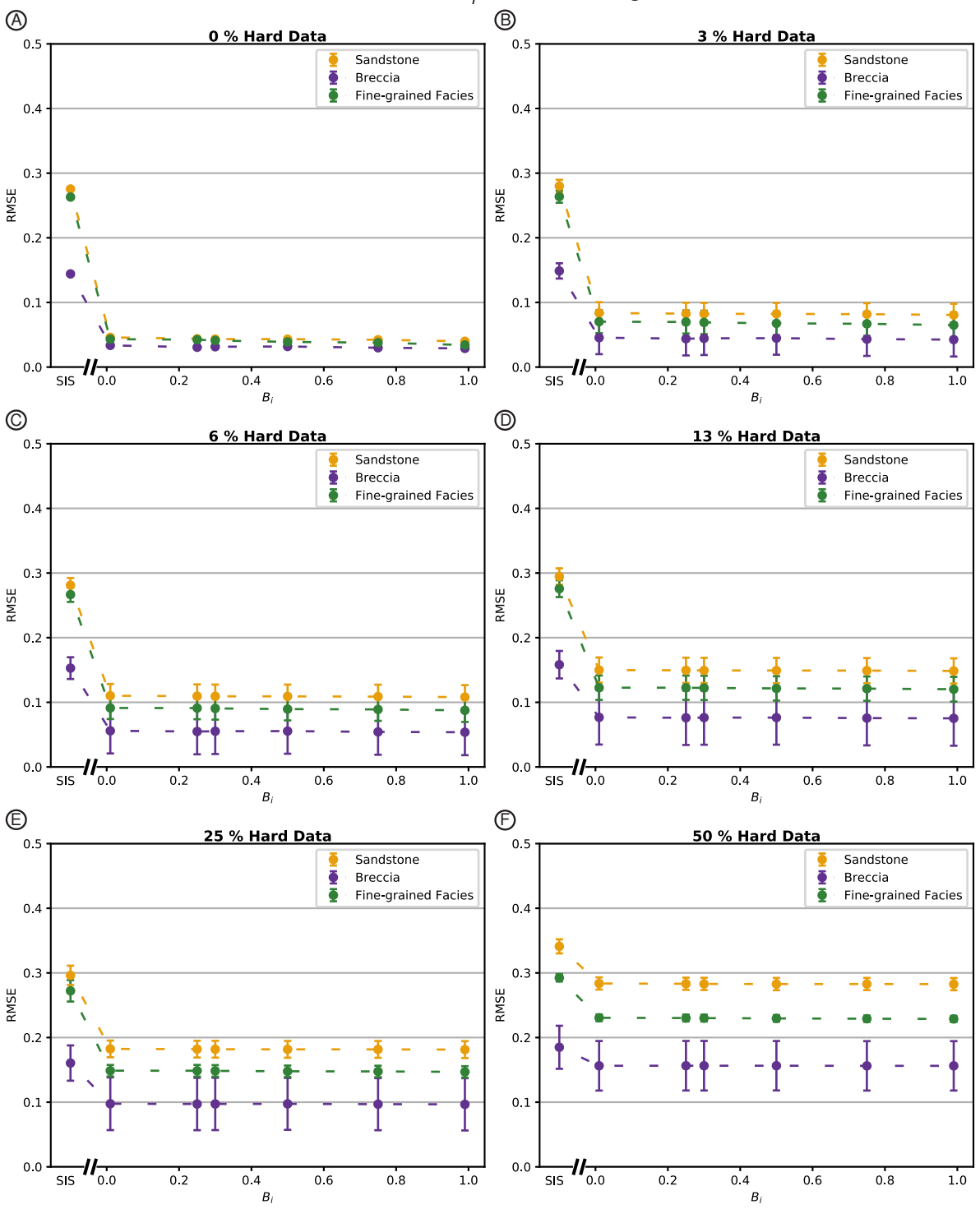

Figure 6.14: Part 1b: 3-Facies Outcrop-Data Results - "1-cell Range" RMSE vs. B_i. Sandstone, breccia and fine-grained ranges are all 0.3 m (1 cell). SK is used and search ellipse encompasses all data. A - F) Results where hard data % ≈ 0, 3, 6, 13, 25, and 50, respectively.

and 6.12F). SIS outperforms COSIS when hard data percentage and soft data weight are both low.

Altering variogram range does impact realizations. Relative to experimentally fit results, reducing variogram range flattens $P_{misclass}$ trends with increasing hard data percentage (e.g., compare Fig. 6.9D, 6.10D, and 6.11D) Increasing hard data percentage at half range exhibits similar properties to full experimentally fit range: $P_{misclass}$ decreases, albeit less so, except for breccia, where it increases (compare Fig. 6.10 and Fig.6.11). When range is reduced to 0.3 m, $P_{misclass}$ curves are nearly flat for all soft data weights, although the experimentally fit range trends are perceptible (Fig. 6.11). Shorter ranges cause all realizations to behave more like they have relatively higher soft data weight. Relative to experimentally fit results, shortening variogram range reduces RMSE for COSIS cases even more dramatically with increasing soft data weight (e.g., compare Fig. 6.12B, 6.13B, and 6.14B). Shorter ranges also improve COSIS realizations with lower soft data weight over pure SIS ones (e.g., compare Fig. 6.12B, 6.13B, and 6.14B). At 0.3 m range, COSIS trends are essentially flat (Fig. 6.14). Corroborating $P_{misclass}$ trends, shorter ranges cause all realizations to behave more like realizations with high soft data weight.

6.1.4 Part 1b: 3-Facies Outcrop-Data Interpretations

For the experimentally fit variography cases $P_{misclass}$ decreases with increasing hard data, both for sandstone and all facies as a whole (Fig. 6.9). This is expected: more information should produce better results. Greater soft data weight (i.e., higher B_i input values) reduces $P_{misclass}$ when hard data is scarce, but greater weight with high hard data percentage is counterproductive (Fig. 6.9). This is also expected: hard data and soft data are only somewhat

congruous, with B ~0.3 (Table 5.6). The soft data is globally accurate to the hard data, but not locally.

The different behavior in fine-grained facies and breccia is instructive. Moderate-proportion fine-grained facies (~23%) are clustered in a single occurrence at the top of the section (Fig. 5.2). This strong architectural signal appears to be self-reinforcing, with strong reproduction in most cases (Fig. 6.4, 6.5, 6.6, and 6.9). This is a positive sign that facies architecture can be reproduced under certain modeling conditions. In contrast, however, low-proportion breccia (~6%), is poorly simulated in all cases, and suffers especially with high hard data percentage (Fig. 6.4, 6.5, 6.6, and 6.9). In these situations, higher-proportion facies cells reinforce each other during kriging and have a greater chance of simulating themselves in the "rare" breccia locations. Consistent architecture reproduction for low-proportion facies architecture reproduction is very unlikely.

RMSE trends are congruous with $P_{misclass}$ trends. At lower and moderate hard data percentage, increasing soft data weight (B_i values) works in concert with the increased hard data to reduce RMSE (e.g., Fig. 6.12A-C). At higher hard data percentage, more cells are populated such that they do not match soft data and RMSE increases (e.g., Fig. 6.12D-F). Arbitrarily increasing soft data weight can reduce RMSE somewhat, but does not counteract this impact entirely. Soft data is a secondary consideration for COSIS, so this outcome makes sense. Furthermore, increasing soft data weight above calibrated B values (Table 5.6) degrades the architectural signal of the fine-grained facies. This is clear from the aggregated example realizations, which grow noisier in appearance with higher soft data weight (e.g., compare Fig. 6.7F to Fig. 6.7G-I and 6.8F to 6.8G-I).

Search ellipse appears to have no impact on realizations. This makes sense for SK, as it works from residuals from the global mean and ensures the entire volume is truly stationary.

Reduced variogram range, however, has some impact. Hard data impact is relatively diminished with shorter variogram range and soft data impact is increased (e.g., compare Fig. 6.9 to Fig. 6.10 and 6.11). Fewer hard data points are significantly weighted with shorter ranges leaving soft data greater latitude to inform unknown cells. Therefore, range reduction increases the impact of soft data (e.g., compare Fig. 6.12 to Fig. 6.13 and 6.14).

6.2 Critical 1-D Findings for 3-D Modeling

1-D experiments (Part 1) highlight several challenges for SIS and COSIS facies architecture reproduction along with some useful observations. Given their related underlying processes, these findings apply broadly to other covariance-based methods as well.

The synthetic experiment (Part 1a) on soft data reliability demonstrates that low-reliability soft data is problematic for SIS and COSIS facies architecture reproduction. This is important for the 3-D models because the soft data reliability for the full model volume is low: the proportion-weighted average of the facies *B* values is only 0.22.

The outcrop-data experiment (Part 1b) reveals two different challenges. Most importantly, the outcrop-data experiment demonstrates that low-proportion facies suffer in all modeling cases. Neither input proportions nor facies architecture are reproduced. Second, arbitrarily high soft data weights can cause problems. For low hard data percentages, a high soft data weight improves outcomes for high-proportion facies and seemingly overall, but this occurs at the expense of moderate and especially low-proportion facies. This is important for 3-D models, which have multiple low-proportion facies and extremely low hard data percentages (See: 5.3 Hard Data Sparsity Context for Experiments). Also, the aggregate of realizations becomes

noisier as hard and soft data conflict more, which indicates that arbitrarily high soft data weight may cause problems for 3-D models as well.

On a positive note, moderate-proportion facies with a strong architectural signal were well-reproduced. This means successful facies architecture modeling is possible under certain conditions. Also, it is noteworthy that reducing variogram range increases the impact of soft data overall.

6.3 Part 2: 3-Dimensional Results

6.3.1 Part 2a: SIS and COSIS Results

Selected SIS and COSIS realizations, comprising two variogram regimes, and five soft data weight (B_i) cases, are examined for qualitative outcrop character reproduction. Results are encapsulated in cross-section slices and facies likelihood vs. probability plots.

Pure SIS, without a soft data constraint, provides a useful baseline for understanding algorithm behavior (Fig.6.15). Outcrop-inferred variography (Table 4.3), which has longer horizontal ranges and shorter vertical ranges compared to those of the experimentally fit variography (Table 5.7, Fig. 5.5, 5.6), produces thinner and more-laterally-continuous facies packages. Realizations with experimentally fit variograms are comparatively noisy; transitions between packages of varying thickness are more abrupt and frequent, appearing dislocated. Outcrop-inferred variography produces more geologically realistic realizations as illustrated by comparing Fig. 6.15 with the facies-painted Willow Creek cross-section in Fig. 3.3C.

COSIS realizations for each variogram regime produce similar results to those of SIS. Increasing soft data weight has no discernable effect at lower values, and at higher values produces moderately more noisy realizations for both variogram regimes (Fig. 6.16).

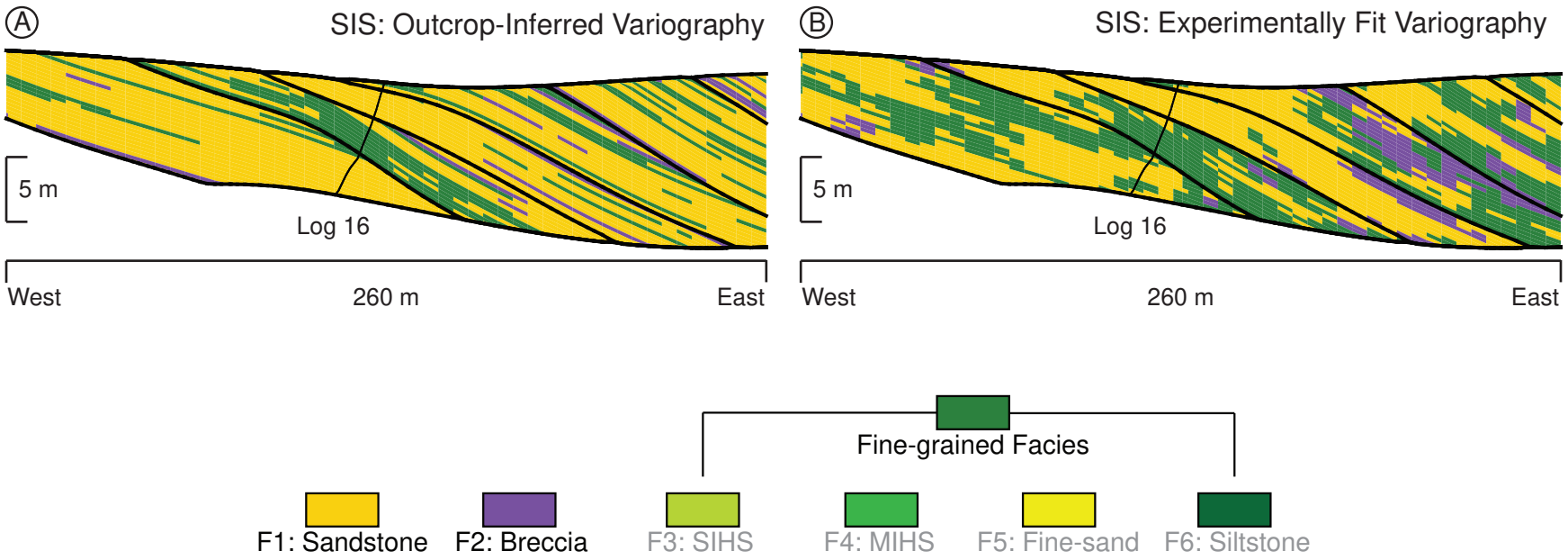

Figure 6.15: 3-D Sector Model Cross-Section Slice: SIS Variography Comparison. A) Outcrop-inferred variography (detailed in Table 4.3) is compared to B) experimentally fit variography (detailed in Table 5.7, Fig. 5.5, and Fig. 5.6).

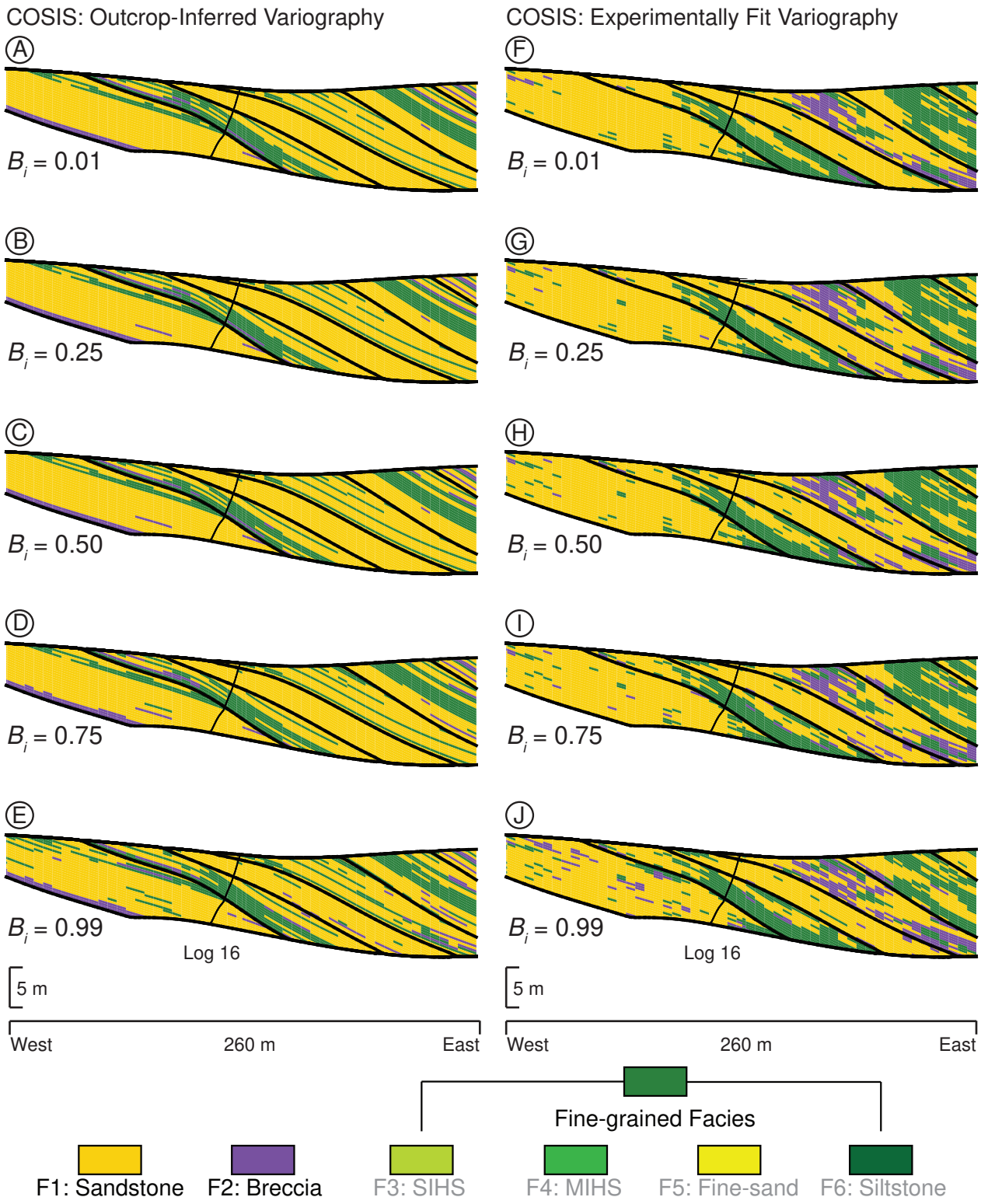

Figure 6.16: 3-D Sector Model Cross-Section Slice: COSIS Variography Comparison. A - E) Outcrop-inferred variography (detailed in Table 4.3) is compared to B - J) experimentally fit variography (detailed in Table 5.7, Fig. 5.5, and Fig. 5.6). Soft data weight is incremented from nearly 0 to nearly 1 at intervals of ~0.25 as a sensitivity variable.

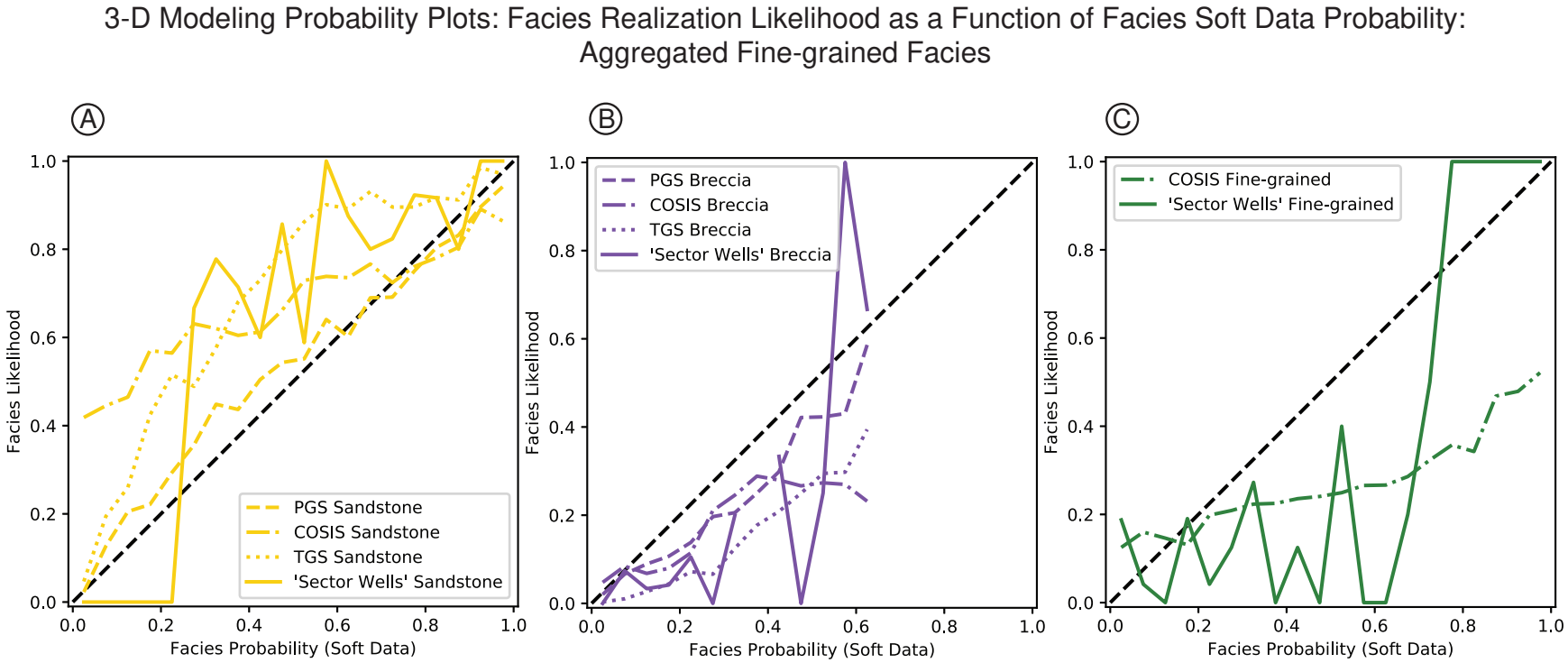

Figure 6.17: For selected realizations (COSIS in Fig. 6.16E, PGS in Fig. 6.20F, and TGS in Fig. 4.8), binned facies soft data probability is plotted on the x-axis and co-located binned realization facies percentages are plotted on the y-axis. For cells with facies soft data probability range, x, the actual realization percentage for that facies at those cells is y. A) Sandstone, B) breccia, and C) fine-grained facies are presented, where fine-grained facies are aggregated to assess and compare COSIS runs with PGS and nested TGS.

Additionally, facies likelihood vs. probability plots were generated for a selected COSIS realization (Fig. 6.16E) to assess facies architecture reproduction (Fig. 6.17). Sandstone in the realization tracks sandstone in the sector wells relatively poorly, with excessive over-representation at low probabilities and under-representation at high probabilities (Fig. 6.17A). Breccia and fine-grained facies track well at low probabilities, but the realization under-represents these facies at high probabilities (Fig. 6.17B and C).

6.3.2 Part 2a: SIS and COSIS Interpretations

There are two important takeaways from this qualitative analysis. Chiefly, outcrop-inferred variography produces more geologically realistic realizations than variography fit from the measured section data (e.g., compare Fig. 6.15 and 6.16 with Fig. 3.3). Strictly fitting variograms to sparse hard data in this study over-estimates short range heterogeneity and poorly reproduces outcrop architecture. This suggests geologic context and sedimentological expertise will improve variogram modeling over purely hard data-driven efforts.

Secondly, increasing soft data weight ($B_{i,}$) arbitrarily actually increases realization noise. Realization noise is a common problem with SIS and COSIS modeling (See: 2B.4 Sequential Indicator Simulation and Co-Sequential Indicator Simulation). This is most obvious when soft data weight is raised from 0.5 (Fig. 6.16C and H) to 0.75 (Fig.616D and I) and 0.99 (Fig. 6.16E and J). Effects are more pronounced for outcrop-inferred variogram (Fig. 6.16A-E) realizations than for experimentally fit variogram realizations (Fig. 6.16F-J), although experimentally fit realizations are noisier to begin with. Emphasizing the continuous variable soft data might seem like a good way to ensure smooth contiguous facies packages, but these test results suggest otherwise. Over-emphasizing soft data may cause the algorithm to discount surrounding simulated cells and populate unknown location with highest-probability facies instead, even if

offsetting cells are all one other facies type. Lower soft data weight would have prioritized variography and facies continuity over the exacting local reproduction of the soft data.

1-D Experiments quantitative findings have a direct link to these qualitative interpretations. Recall the 1-D outcrop-data experiment (Part 1b) (See: 6.2 Critical 1-D Findings for 3-D Modeling). First, shorter variogram ranges are associated with higher soft data impact. Second, for low- and moderate-proportion facies, arbitrarily high soft data weights are associated with poor input proportion reproduction and high $P_{misclass}$. 3-D realization noise, is likely a qualitative representation of two phenomenon. Finally, noisy architecture reproduction for aggregated 1-D 3-facies experiments (Part 1b) foreshadowed problems for 3-D realizations (See: 6.1.4 Part 1b: 3-Facies Outcrop-Data Interpretations).

In these 3-D models, experimentally fit variography is shorter-range than outcrop-inferred variography. This means experimentally fit variogram realizations will act as if they have relatively higher soft data weight, systemically reducing architectural reproduction and increasing noise. The impacts are noticeable for outcrop-inferred variography only when soft data is very overweight (Fig.6.16D and E), but the compounded effects cause a pervasive noise problem for experimentally fit variography (Fig.6.16F-J).

6.3.3 Part 2b: PGS Results

Selected PGS realizations, comprising four horizontal ranges, four vertical ranges, and two LTRs, are examined for qualitative outcrop character reproduction. Results are encapsulated in cross-section slices, plots of realization facies proportion as a function of selected input parameters, and facies likelihood vs. probability plots. Some realizations exhibit cells or cell clusters that are blank: the algorithm leaves certain cells unrealized if proportion data, variography, or the LTR conflict irreconcilably.

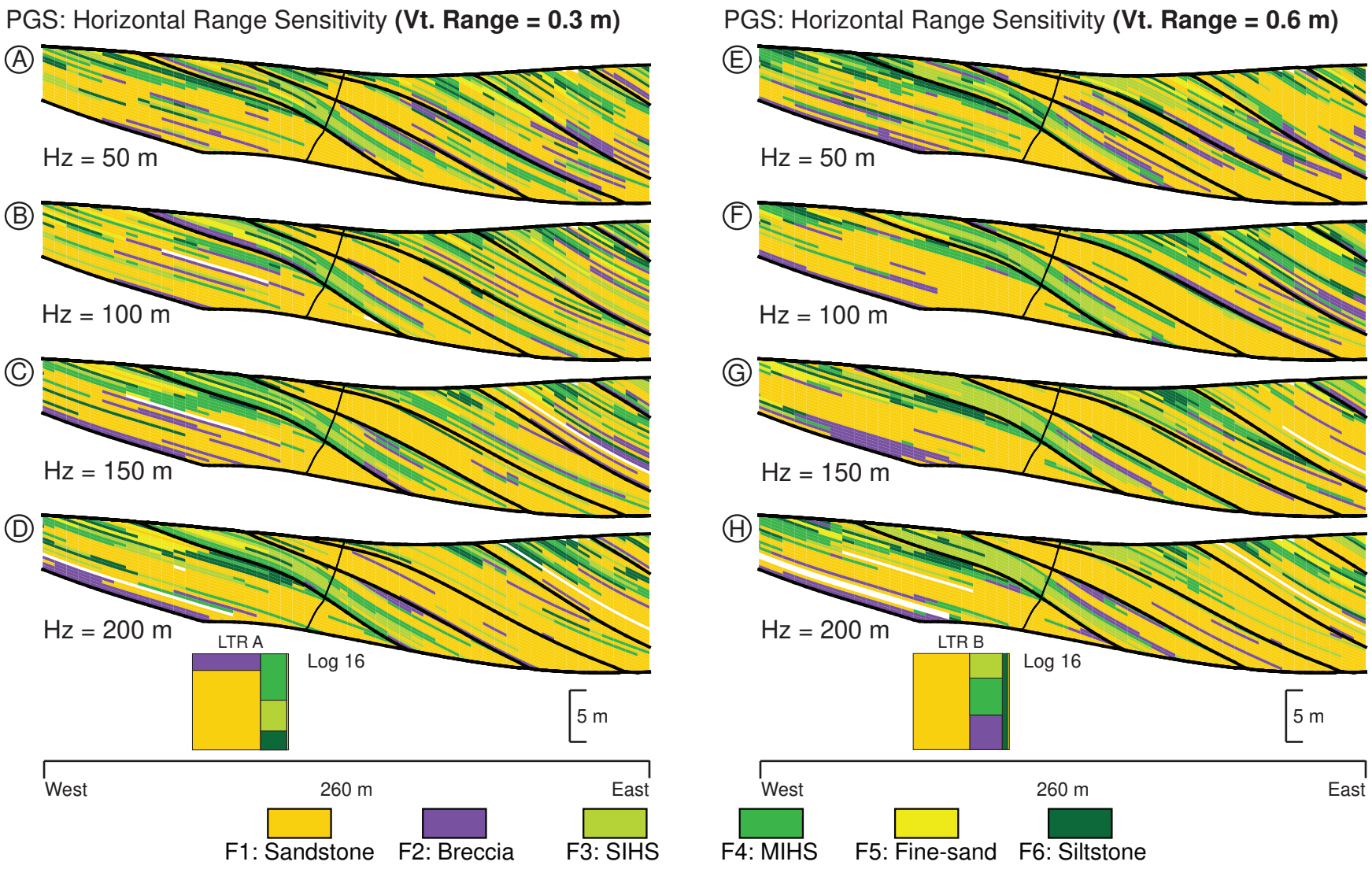

Figure 6.16: 3-D Sector Model Cross-Section Slice: PGS Horizontal Range Sensitivity. A. - D.) 0.3 m vertical range is compared to E. - H.) 0.6 m vertical range. Horizontal range is increased from 50 m to 200 m at 50-m intervals. Impact of different LTRs is likely low.

Increasing horizontal variogram range while holding the vertical variogram and LTR constant generates progressively thinner and more-laterally-continuous facies packages, but effects are less pronounced with larger vertical ranges (e.g., compare Fig. 6.18A - D and then, separately, Fig. 6.18E - H). LTR does not change this effect. Longer horizontal ranges also generate more blank cells (e.g., compare Fig. 6.18E and H). Increasing horizontal range increases sand proportion above the input proportion (Fig. 6.19A). Conversely, MIHS, breccia, and siltstone proportions are decreased (Fig. 6.19B). SIHS and fine sandstone proportions do not exhibit a clear pattern (Fig. 6.19B).

Increasing vertical variogram range generates progressively thicker and less-laterally-continuous facies packages, but effects are less pronounced with larger horizontal ranges (e.g., compare Fig. 6.20A-D and then, separately, Fig. 6.20.E-H). LTR also does not change this effect. At highest vertical ranges, noticeably more cells go unrealized (e.g., Fig. 6.20D and H). Increasing vertical range decreases realization sand proportion closer to input proportions (Fig. 6.21A). Conversely, MIHS, breccia, siltstone, and fine sandstone proportions are increased (Fig. 6.21B). SIHS proportions do not exhibit a clear pattern (Fig. 6.21B).

Changing LTR has only a small effect on realizations: for LTR B sandstone proportion appears to increase slightly, and beds are thicker and more-laterally-continuous relative to LTR A realizations (e.g., compare Fig. 6.22A-C and then, separately, Fig. 6.22D-F). In aggregate, LTR B generates more sandstone on average, but barely so, and well within standard deviation of LTR A realizations (Fig. 6.23A). This corresponding reduction in other facies is also vanishingly small (Fig. 6.23B).

Additionally, facies likelihood vs. probability plots were generated for a selected PGS realization (Fig. 6.20F) to assess facies architecture reproduction (Fig. 6.24). Overall, the PGS

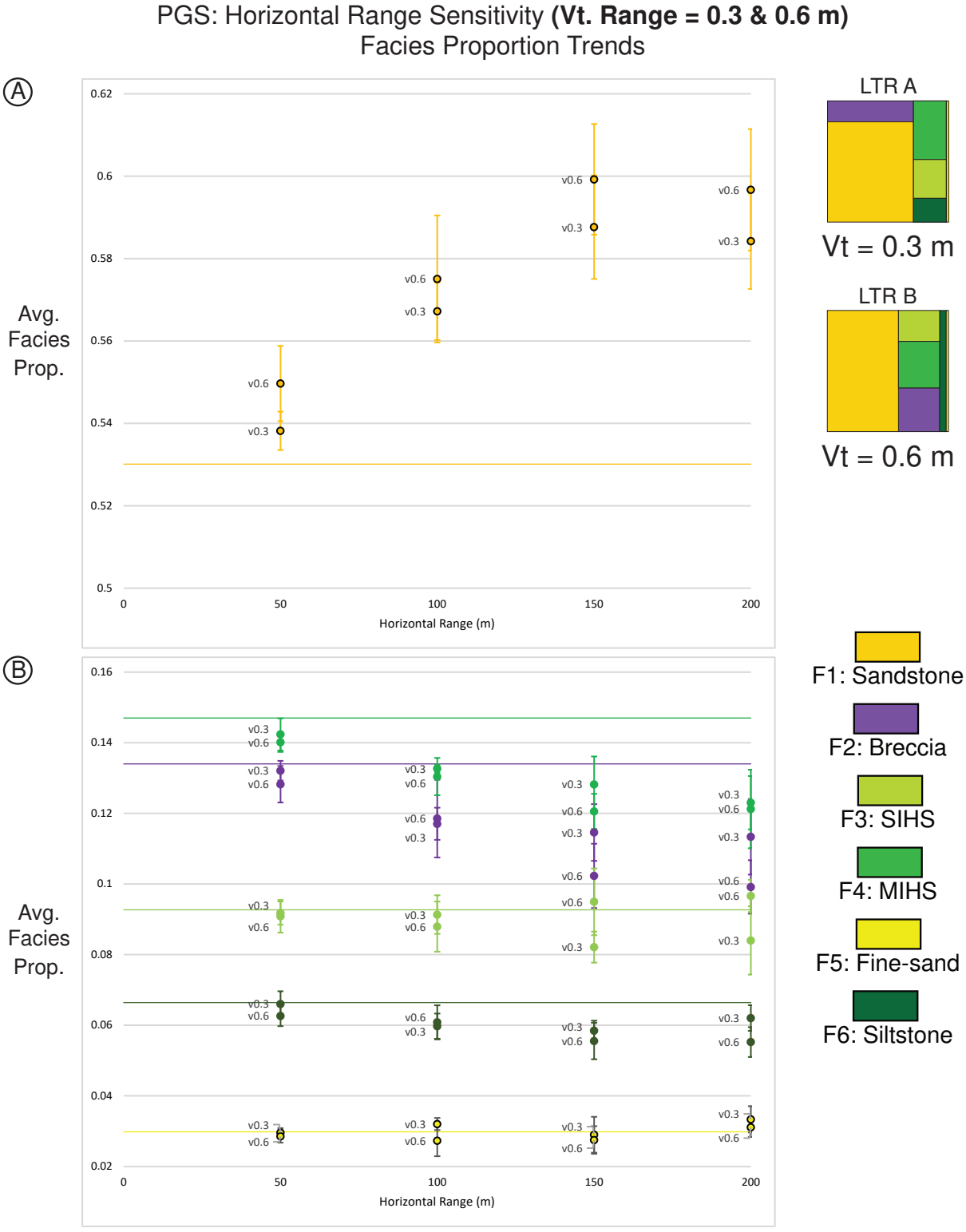

Figure 6.19: 3-D Sector Model Cross-Section Slice: PGS Horizontal Range Sensitivity Facies Proportion Trends. Realization facies proportion averages and standard deviations are plotted against horizontal range for A) sandstone and B) all other facies. Horizontal colored lines indicate facies input proportions.

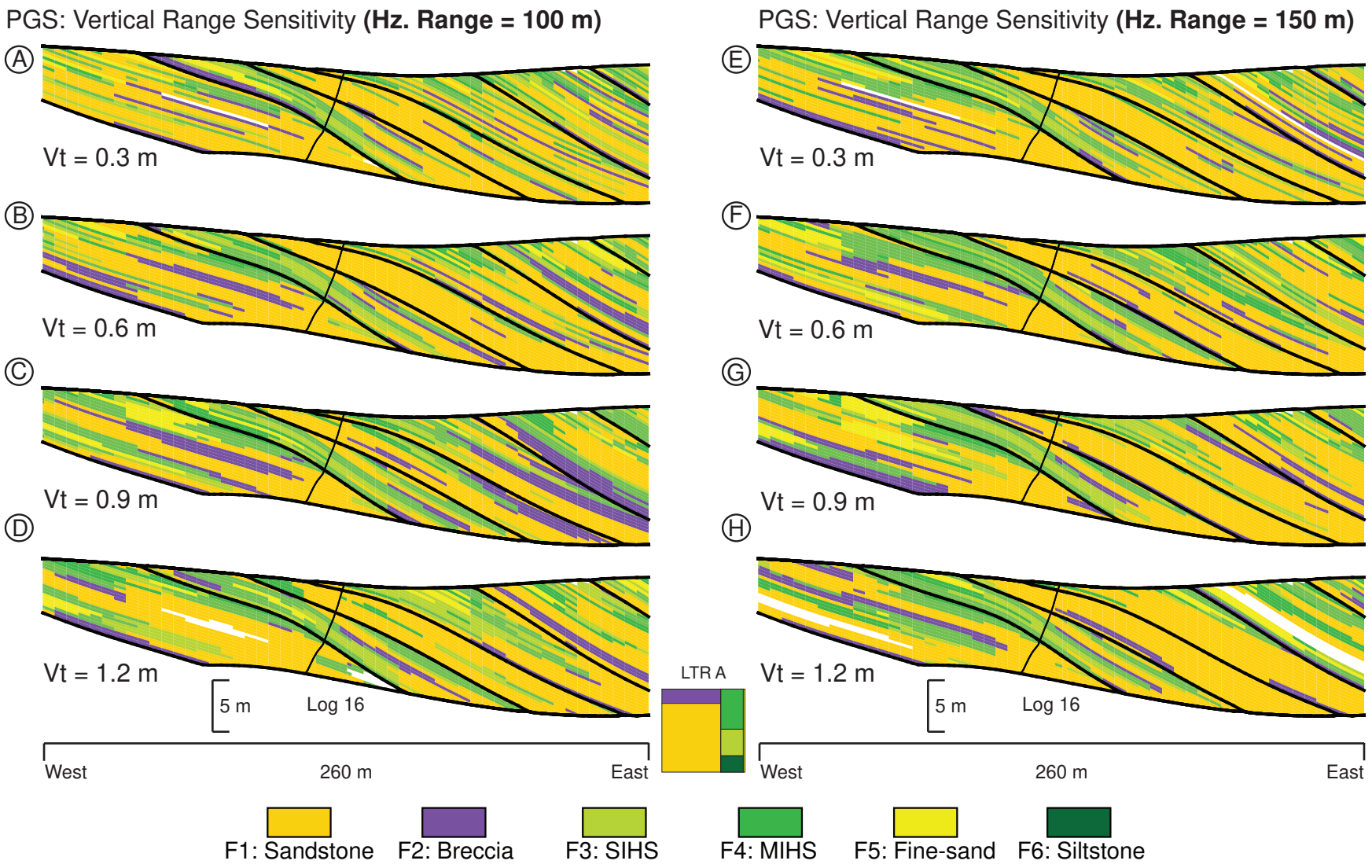

Figure 6.18: 3-D Sector Model Cross-Section Slice: PGS Vertical Range Sensitivity. A. - D.) 100 m horizontal range is compared to E. - H.) 150 m horizontal range. Vertical range is increased from 0.3 m to 1.2 m at 0.3-m intervals for horizontal ranges of 100 m and 150 m. All realizations use LTR A.

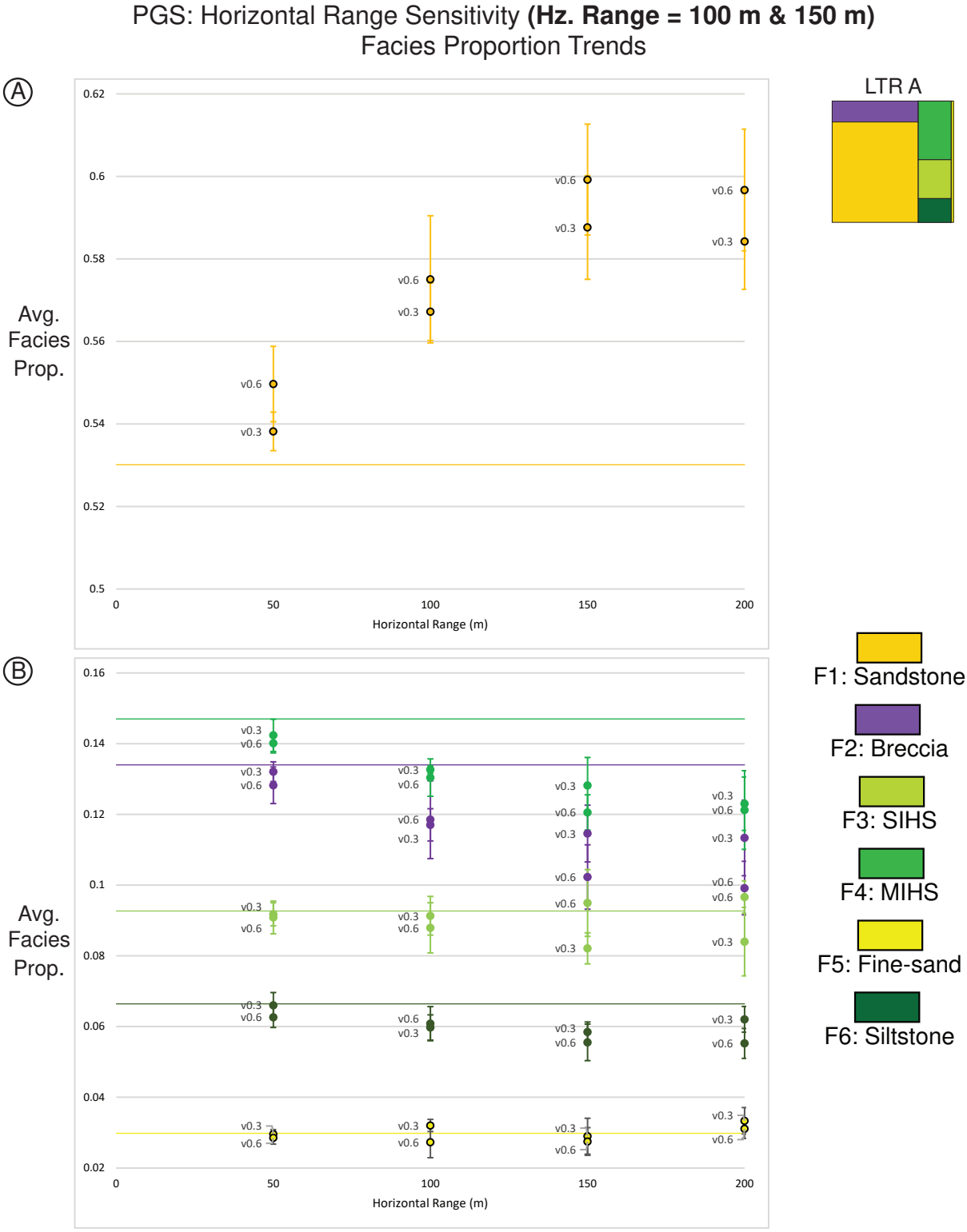

Figure 6.21: 3-D Sector Model Cross-Section Slice: PGS Vertical Range Sensitivity Facies Proportion Trends. Realization facies proportion averages and standard deviations are plotted against vertical range for A) sandstone and B) all other facies. Horizontal colored lines indicate facies input proportions.

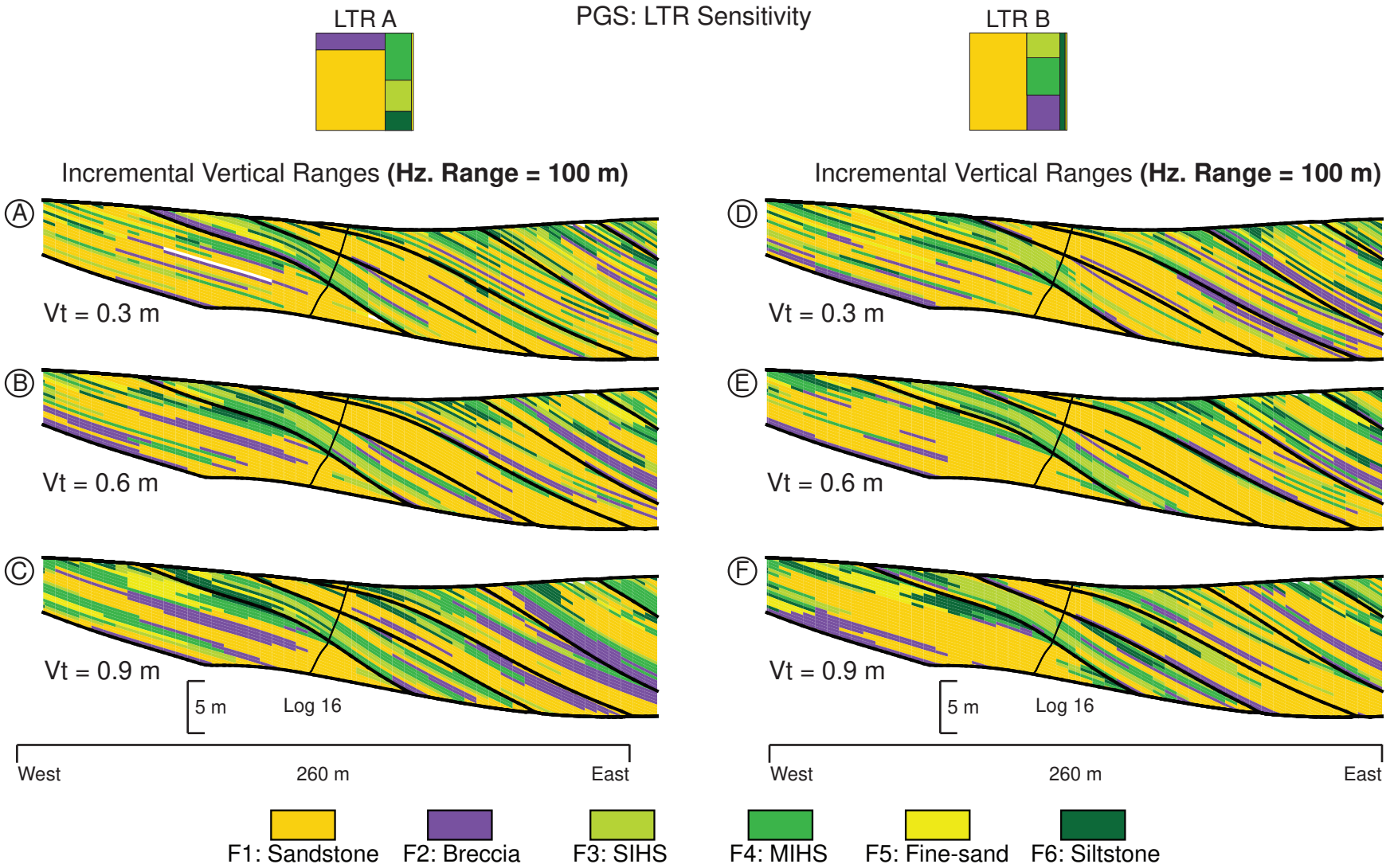

Figure 6.22: 3-D Sector Model Cross-Section Slice: PGS LTR Sensitivity. A - C) LTR A is compared to D - F) LTR B. Vertical range is increased from 0.3 m to 0.9 m at 0.3-m intervals for horizontal ranges of 100 m and 150 m. All realizations use 100 m horizontal range.

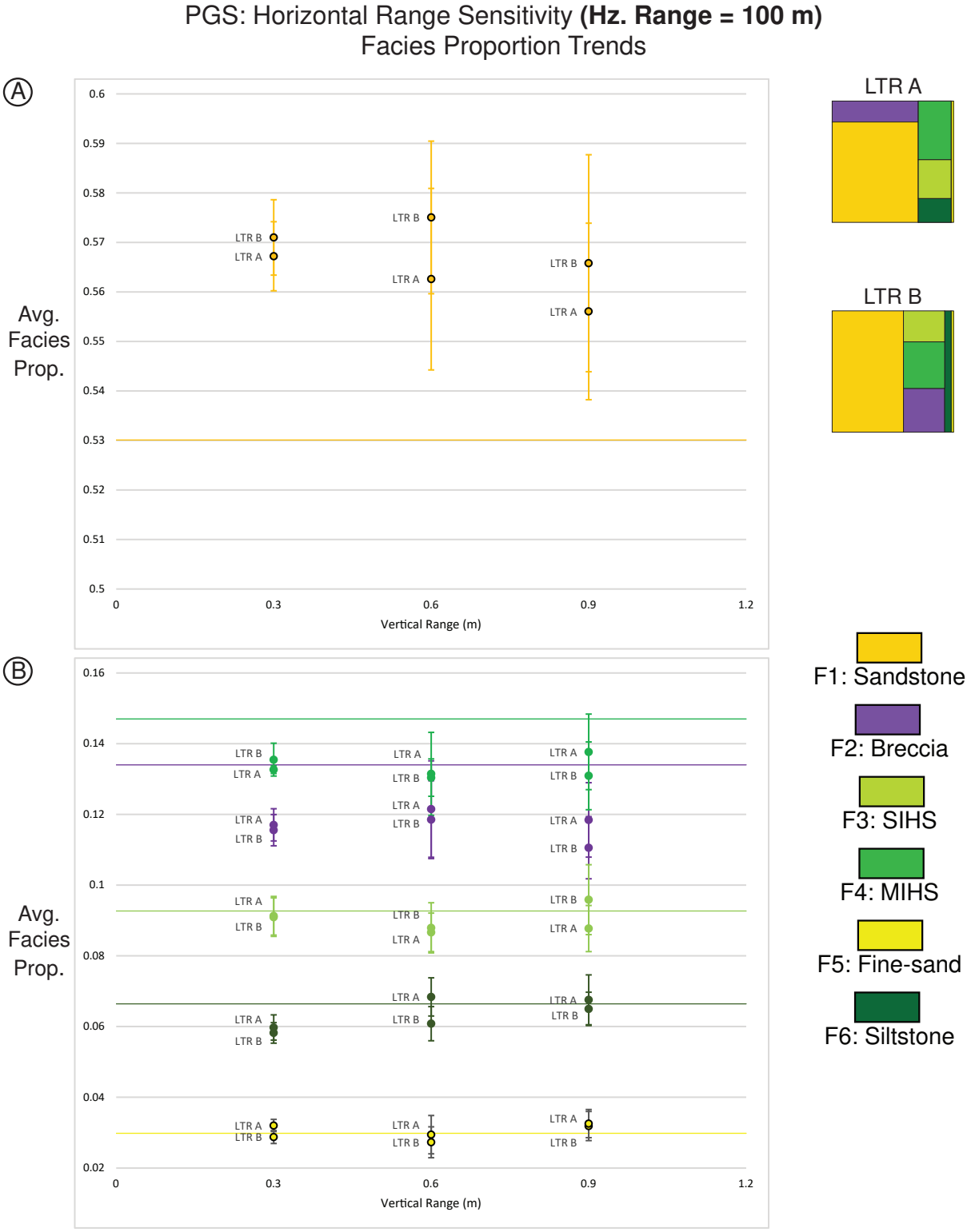

Figure 6.23: 3-D Sector Model Cross-Section Slice: PGS Vertical LTR Sensitivity Facies Proportion Trends. Realization facies proportion averages and standard deviations are plotted against vertical range for A) sandstone and B) all other facies. Horizontal colored bars indicate facies input proportions.

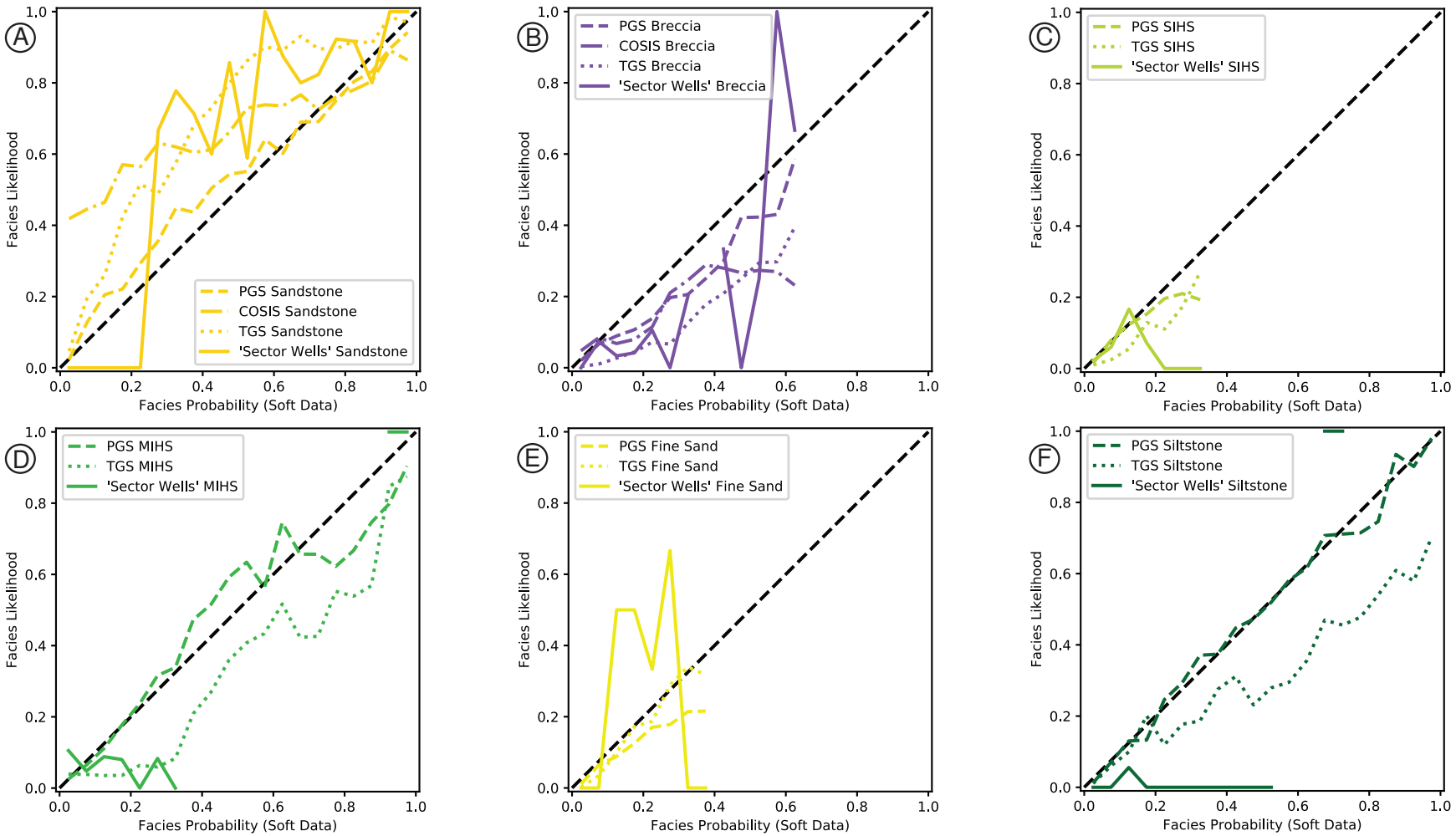

Figure 6.24: For selected realizations (COSIS in Fig. 6.16E, PGS in Fig. 6.20F, and TGS in Fig. 4.8), binned facies soft data probability is plotted on the x-axis and co-located binned realization facies percentages are plotted on the y-axis. For cells with facies soft data probability range, x, the actual realization percentage for that facies at those cells is y. Sandstone, breccia, SIHS, MIHS, fine sandstone, and siltstone are presented (A - F, respectively) to assess PGS and nested TGS runs.

realization follows the 1:1 line better than it tracks the sector wells. For sandstone, the realization over-represents sandstone at lower probabilities and under-represents at higher probabilities (Fig. 6.24A). For breccia, the realization tracks the sector wells at lower probabilities and under-represents breccia at moderate probabilities (Fig. 6.24B). For SIHS, the realization tracks the sector wells at the lowest probabilities and over-represents above 0.2 probability (Fig. 6.24C). For MIHS, the realization over-represents at all probabilities (Fig. 6.24D). For fine sandstone, the realization under-represents at all probabilities (Fig. 6.24E). For siltstone, the realization over-represents at all probabilities (Fig. 6.24F).

6.3.4 Part 2b: PGS Interpretations

Changes to variography and LTR have relatively minor impact on algorithm behavior, and most impacts appear to result from conflicts between data types. However, knowledge of these changes may aid modelers who: 1) choose to incorporate outcrop data iteratively or holistically instead of strictly a priori and 2) need to address data conflicts in a PGS workflow. Horizontal variography, is discussed first, followed by vertical variography, and LTR construction.

For the horizontal regime, it is expected that longer variogram ranges create more-laterally-continuous packages (Fig. 6.18). However, the increase in unrealized cells requires some explanation. Unrealized cells indicate discrepancies between input data and algorithm parameters. It is possible that longer-range structures are more difficult to fit into a given space and will cause more conflicts with other inputs and parameters. This is likely due, in part, to a proportion discrepancy between the sector model well data and probability volumes (i.e., a soft data reliability problem). The sector well data have a much higher sandstone proportion than the probability volumes and correspondingly lower proportions of other facies than the probability volumes. In contrast, the probability volumes, which are consistently stationary throughout the

model (i.e., globally accurate, but not locally), show average facies probabilities in line with average of all wellbores. Long horizontal ranges, especially when paired with short vertical ranges, have less flexibility to satisfy proportion objectives.

High-proportion facies (e.g., sandstone) gain proportion even more at higher horizontal ranges, while lower-proportion facies lose proportion (Fig. 6.19A vs. B). Longer-range structures appear more likely to truncate to high-proportion facies, thus over-representing that high-proportion facies in realizations. Necessarily, this over-representation comes at the expense of other lower-proportion facies. The fact that SIHS does not exhibit a clear proportion trend may be due to the fact that it is architecturally ambiguous (Fig. 6.19B). SIHS sits astride the coarse and fine-grained facies divide and is architecturally associated with both the upper and lower portions of an LAP. Fine sandstone does not exhibit a proportion trend because its proportion is too low to exhibit any signal (Fig. 6.19B). Its placement is completely dominated by other facies.

For the vertical regime, when vertical ranges are short and beds are thin, they must truncate so as to form more-laterally-continuous beds (Fig. 6.20). For long horizontal ranges, this may cause more unrealized cell problems. For short horizontal ranges, discrepancies are less likely, although the impact is mild overall. Conversely, when vertical ranges are long and beds are thicker, truncations need not reach out as far in the horizontal plane. The algorithm has more flexibility to reconcile its inputs and parameters. Again, this effect is mild, and possibly reverses if the vertical range becomes too high.

High-proportion facies (e.g., sandstone) lose proportion with increasing vertical ranges and lower-proportion facies gain proportion (Fig. 6.21A vs. B). This is also due to the fact that the algorithm is given greater flexibility to satisfy its many criteria. Given the high anisotropy

between horizontal and vertical range behavior in Horseshoe Canyon deposits, an increase in vertical range lends more flexibility to the algorithm to satisfy the input data and parameters.

LTR appears to have a limited impact on realizations (Fig. 6.22). However, the difference between these particular LTRs are minor: both were designed with the outcrop transition statistics in mind (See: 5.2.3 Part 2b: PGS Experiments). A significantly different LTR might have produced a more noticeable effect on realizations. An explanation for marginally higher and more-continuous sandstone content in LTR B realizations is that sandstone has fewer permissible transitions: specifically, sandstone cannot transition to siltstone and vice versa (Fig. 6.23). This diminishes heterogeneity of sandstone, the highest-proportion facies. As a result, realizations become marginally more homogenous and sandstone, the highest-proportion facies, is increasingly over-represented.

PGS qualitative outcomes suffer somewhat from low-reliability soft data, especially when anisotropy of variograms increases. Given the highly anisotropic nature of sedimentary deposits, the reservoir modeler may not be able to avoid this problem and can only work to mitigate it by reducing discrepancy between soft and hard data. This relates back to the quantitative findings of the 1-D experiments in the sense that low-reliability soft data was problematic for SIS / COSIS architecture reproduction (See: 6.2 Critical 1-D Findings for 3-D Modeling).

6.3.5 Part 2 Interpretations: Comparing COSIS and PGS to Nested TGS

Nested TGS outperforms both COSIS and PGS realizations with respect to facies architecture reproduction on the basis of qualitative inspection of realization cross-section slices (Fig. 6.25). Bedding is highly elongate with smooth transitions. Realizations are relatively noise-free and facies grow increasingly fine-grained up-section. Most telling of all: breccias are

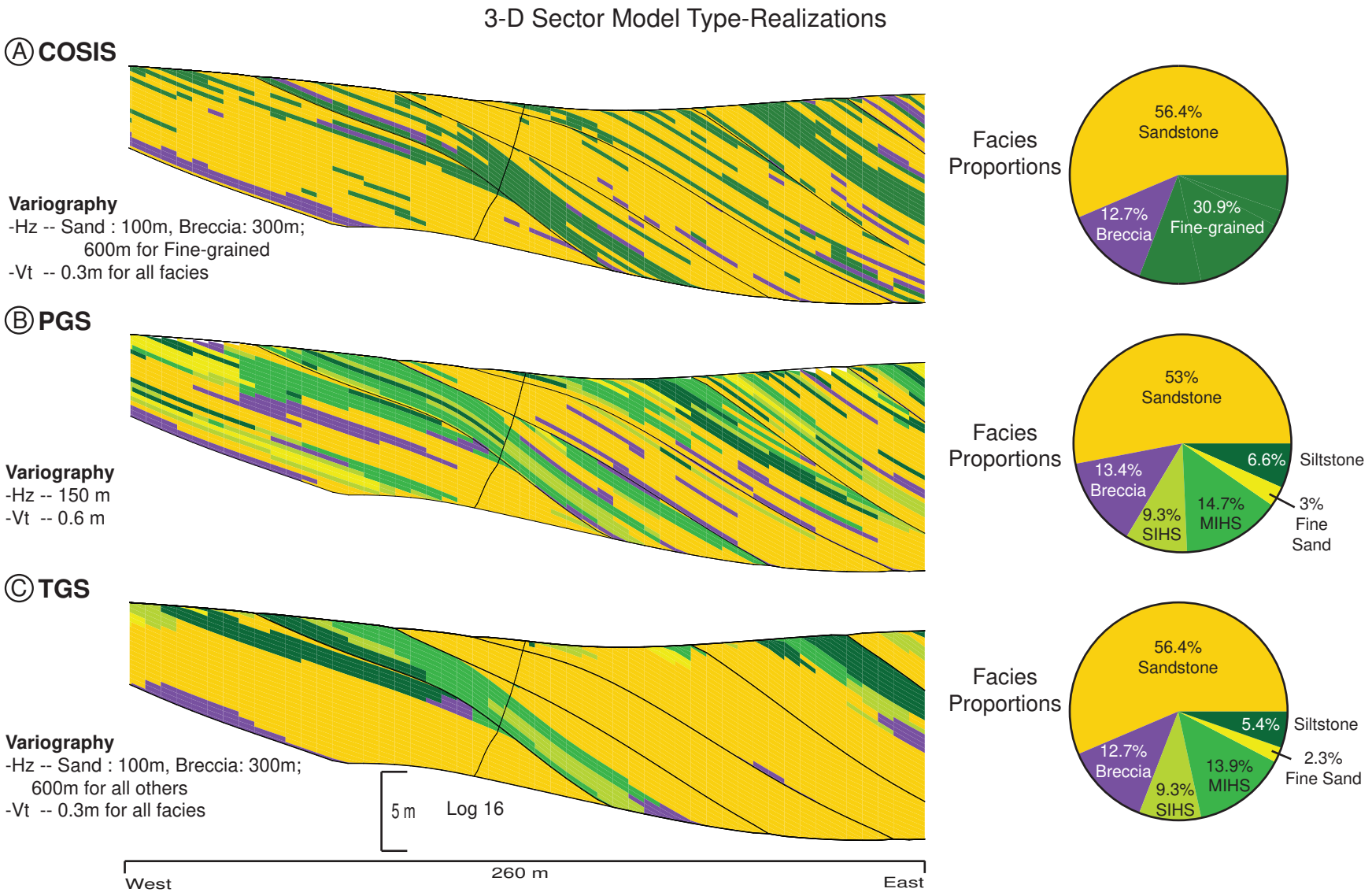

Figure 6.25: Characteristic 3-D sector model type-realizations for A) COSIS (Fig. 6.16E), B) PGS (Fig. 6.20F), and C) nested TGS (Fig. 4.8). Qualitative facies architecture reproduction is summarized in these type realizations.

very common at LAP bases but may be simulated as minor erosional surfaces anywhere within a package. Further still, these breccias are not scattered noise, but discrete bedforms. These are key qualitative pieces of the outcrop architecture.

Plots of facies likelihood vs. probability for selected realizations (6.16E for COSIS and 6.20F for PGS) also show that nested TGS reproduces facies architecture best. Nested TGS tracks sector well data better than COSIS (Fig. 6.17) and PGS (Fig. 6.24), but not perfectly. Tracking is strongest in the sandstone, breccia, and MIHS plots, which are the highest-proportion facies (Fig. 6.24A, B, and D, respectively). The poor tracking by other lower-proportion facies is likely, in part, due to their lower sample count; their statistics are ambiguous. COSIS performs poorly despite aggregation of fine-grained facies. PGS, as expected, adheres strongly to soft data because the algorithm implementation is biased to full confidence in soft data.

Superior performance of nested modeling is likely due to the fact that facies relative proportions are increased dramatically when they are modeled one by one (Table 6.1).

Table 6.1: Nested TGS Facies Proportions vs. Relative Proportions at Time of Modeling

	True Proportions		Relative Proportions	
Facies	**Facies**	**"Else"**	**Facies**	**"Else"**
Sandstone	0.56	0.44	0.56	0.44
Breccia	0.13	0.31	0.29	0.71
SIHS	0.09	0.22	0.30	0.70
MIHS	0.14	0.08	0.64	0.36
Fine Sandstone	0.02	0.05	0.30	0.70
Siltstone	0.05	-	-	-

The displacement of low-proportion facies by high-proportion facies is diminished with a nested workflow. However, all algorithms over-represent sandstone at low probability, whereas sector wells show no sandstone below 20% probability (Fig. 6.17 and 6.24). Sandstone is over-represented specifically where fine-grained facies should reside. The architectural signal of the most important facies in the outcrop is systemically degraded in this fashion.

CHAPTER 7: DISCUSSION

The original objective of this study was to improve upon prior modeling efforts searching for robust ways to incorporate outcrop statistics into geostatistical models such that those models would better reproduce facies architecture in realizations. Ultimately, those statistics must be incorporated into models as hard data, soft data, or an algorithm parameter (e.g., informing variography or facies order). 1-D experiments (Part 1) shed light on the certain problems incorporating that data and impacts on architecture reproduction. 3-D sector models (Part 2) shed light on algorithm performance generally with respect to facies architecture.

7.1 1-D Experiment Discussion

Synthetic 1-D modeling demonstrates that incorporating soft data may actually inhibit facies architecture reproduction instead of guiding it when that soft data is only weakly informative. This is of particular interest because *B* values from field data are often low, which means weakly informative soft data is the norm (Yao, 2002; Moysey et al., 2003). Outcrop-data 1-D modeling demonstrates low-proportion facies are difficult to simulate in their architecturally correct positions, even in a relatively simple architectural setting (e.g., upwards-fining LAPs with breccias interspersed). In fact, higher-proportion facies are prioritized at the expense of low-proportion facies. This especially undesirable given the fact that lower-proportion facies comprise the architectural heterogeneity of interest. Simply increasing soft data weight is no solution; arbitrarily high soft data weights improve architecture reproduction for high-proportion facies, but, again, at the expense of moderate- and low-proportion facies.

Both of these findings apply to the 3-D modeling effort. The soft data reliability for the full model volume is marginally worse than the 1-D experiment: the proportion-weighted

average of the facies *B* values is 0.22. Furthermore, there is not just one facies with low proportion; five of the six facies have a proportion less than 15% (Table 5.3). While it is true these problems were only demonstrated here with SIS and COSIS, they are also instructive for PGS and nested TGS due to similar underlying processes.

7.2 3-D Experiment Discussion

While sensitivity testing of algorithm parameters (e.g., variogram range, LTR composition) gives indications on how to approach certain problems (e.g. anisotropy and low-reliability soft data), the most important difference for facies architecture reproduction is algorithm selection.

COSIS nominally offers greater control of the spatial correlation of each facies through full IK. However, even in a simplified 3-facies setup, outcrop character reproduction was mediocre and simulated bedding was very noisy. PGS offers less explicit control over spatial correlation, but builds a more statistically-complex model by incorporating transition probabilities and facies ordering. Realizations reproduce outcrop character somewhat better than COSIS, but bedding is still relatively noisy. Furthermore, conflicting inputs and parameters often cause unrealized cells. It is possible that the simplifications required by PGS to use facies transition statistics and set variogram ranges also mean PGS is not well-suited to reproduce outcrop character with this level of complexity. Both algorithms have trouble with low-reliability soft data and fail to honor low-proportion facies.

Nested TGS, the control case from previous work (Durkin, 2016), offers explicit control over spatial correlation of each facies and more variogram options than COSIS. Facies transitions are user-specified insomuch as they are dependent on nesting order. For this algorithm, outcrop character reproduction is strongest and bedding transitions are smoothest; it is

qualitatively the best performer based on inspection of realization cross-section slices. Facies likelihood vs. probability plots also indicate nested TGS realizations better track soft data discrepancy plots of the well data. Nested modeling holds the key to this success by increasing relative-proportions of low-proportion facies and thus counteracting the low-proportion-displacive effects found in covariance-based methods.

7.3 Implications for Subsurface Modeling

Both COSIS and PGS prove underwhelming for the bed-scale architecture reproduction needs of this study. Nested TGS poses a "workflow" solution to this particular problem. COSIS, a relatively simple method, leaves much to be desired when it comes to facies architecture reproduction. PGS, a more complex and difficult method to implement, performs somewhat better. However, it presents stability issues if input data and parameters are incongruous causing unrealized pixels. Nested TGS combines strong spatial correlation control with smooth variography and, most importantly, empowers the modeler to address the problem of disparate facies proportions directly. Given that petroleum industry data is typically sparse (See: 5.3 Hard Data Sparsity Context for Experiments) and / or ambiguous, no method is ideal, but each is workable for certain applications. However, more important than method selection, the modeler should strive to: 1) organize their facies and facies associations to avoid low-proportions whenever practical and 2) make their soft data as reliable as possible. Doing these things will improve outcomes more than anything else.

Nesting is powerful because it can be applied to any data set and any method. The modeler should not think of nesting so much as a binary modeling step, but as an approach to data organization that is by modeling objectives. Many nesting paradigms could be envisioned (e.g. interpretive facies importance, petrophysical similarity, architectural or facies association,

or most-equivalent proportions). Knowing that low-proportion facies are problematic, the modeler can employ a nesting scheme that considers the difference in proportions at each nesting step. This study does not reveal an optimization strategy that could elevate this workflow design to a generalized paradigm for nested modeling. Depending on the modeling objectives and the vagaries of a given dataset, different priorities will require different, possibly tailored, solutions, each with their own set of compromises.

7.4 Modeling Decisions and Impact on Predicting Fluid Flow

Flow simulations were not performed to test architectural ramifications of displaced fine-grained rock, but these impacts can be inferred for the Horseshoe Canyon Formation. Fine-grained facies (F3-F6) are low-permeability, baffle and barrier facies as compared to sandstone (F1), which is a high-permeability reservoir facies. Realizations displace baffle and barrier rock and replace it with reservoir rock. Fine-grained facies concentrate at the tops of LAPs, thus LAP tops will be excessively permeable. On a relative basis, fluid will flow more easily from one LAP into another. The architectural impact of the fine-grained facies, and by extension, the entire LAP framework, is systemically reduced. The models will be systemically more homogenous than the outcrop and therefore more permeable at the geobody-scale. This is unfortunate, as one of the global objectives of this study was to examine bed-scale heterogeneities as they pertain to reservoir applications. Without flow simulation testing, however, the severity of the problem is unclear.

CHAPTER 8: CONCLUSIONS

Geostatistical models are a powerful tool to study petroleum reservoir uncertainty (Keogh et al., 2007). Sparse subsurface data often necessitates the use outcrop analog data to inform key parameters (Dubrule and Damsleth, 2001; Pyrcz and Deutsch, 2014). Bed-scale heterogeneity can impact reservoir fluid flow (Deschamps et al., 2012; Martinius et al., 2017; Meirovitz et al., 2021), and while quantitative outcrop data is increasingly available (Pringle et al., 2004; Bellian et al., 2005; Enge et al., 2007; Pranter et al., 2007; Deschamps et al., 2012; Purkis et al., 2012), incorporating it into models is not straightforward (Ma, 2009). Detailed outcrop statistics of fluvial point bar deposits of the Horseshoe Canyon Formation outcropping southern Alberta (Durkin et al., 2015) were previously used to build probability volumes to incorporate outcrop facies architecture in nested TGS geostatistical models and qualitatively reproduce intra-point bar architecture in realizations (Durkin, 2016).

The overarching goal of this study was to expand on that preceding work. 1-D experiments (Part 1) were devised to explore limitations of covariance-based models with simple synthetic (Part 1a) and outcrop-data cases (Part 1b) with particular focus on issues of soft data reliability, soft data weight, and low-proportion facies. 3-D sector models (Part 2) test SIS / COSIS (Part 2a) and PGS (Part 2b) realizations, and compare them to nested TGS realizations. 1-D experimental findings inform the interpretations of various problems encountered in sector modeling.

Despite integration of outcrop statistics, covariance-based geostatistical methods struggle to reproduce intra-point bar facies architecture. Myriad minor problems can add up to a fatal result, but two particular problems stand out as both severe and pervasive. One: when there is a

weak statistical relationship between hard data and soft data (i.e., the soft data is low-reliability), incorporating that soft data may not only be low-utility, it may make realizations worse. Two: as a rule, low-proportion facies are poorly reproduced with respect to both target proportion and facies architecture. This is unfortunate because the low-proportion facies generally comprise the heterogeneity of interest; their poor reproduction diminishes the whole value of the modeling effort. Nested modeling partially mitigates low-proportion effects, but this comes at the cost of a complex workflow that requires many tailored modeling decisions.

CHAPTER 9: FUTURE WORK

Future work breaks into three categories: 1) low-reliability soft data and low-proportion modeling, 2) nested modeling, and 3) sensitivity analysis for outcrop soft data incorporation. Several low-reliability soft data and low-proportion modeling questions of varying scope remain. Whether COSIS with OK performs consistently better with respect to facies architecture in low-reliability soft data cases is a specific question. Generalized performance thresholds and guidelines for low-reliability soft data and low-proportions should be investigated along with more exhaustive inspection of a possible empirical relationship between facies proportions and soft data reliability as they relate to facies architecture reproduction error. Nested modeling performance gains should be tested more comprehensively on ground-truth 3-D volumes with COSIS, TGS, and PGS against non-nested workflows. Low-proportion thresholds and architectural complexity are sensitivity variables that may be used to establish when the extra effort of nested modeling is worthwhile. Finally, future work could continue investigations into how best to incorporate outcrop statistics. Incorporating trend information into VPC-derived soft data may help increase soft data reliability (i.e., improve the local accuracy of those volumes). Transition probabilities, as they are mathematically linked to variography, may be able to serve a more generalized role for algorithms other than PGS, possibly with soft data conditioning. Summary statistics for architecture reproduction remain elusive: $P_{misclass}$ is probably too simple a metric. Multiple point density functions should be investigated further for utility in checking covariance-based models against their input data.

REFERENCES

Ainsworth, R. B., B. K. Vakarelov, C. Lee, J. A. MacEachern, A. E. Montgomery, L. P. Ricci, and S. E. Dashtgard, 2015, Architecture and Evolution of A Regressive, Tide-Influenced Marginal Marine Succession, Drumheller, Alberta, Canada: Journal of Sedimentary Research, v. 85, no. 6, p. 596–625, doi:10.2110/jsr.2015.33.

Ainsworth, R. B., and R. G. Walker, 1994, Control of estuarine valley-fill deposition by fluctuations of relative sea-level, Cretaceous Bearpaw–Horseshoe Canyon transition, Drumheller, Alberta, Canada, *in* P. A. Scholle, ed., Incised-Valley Systems: Origin and Sedimentary Sequences: SEPM, Special Publication 51: p. 159–174.

Alabert, F., 1987, The practice of fast conditional simulations through the LU decomposition of the covariance matrix: Mathematical Geology, v. 19, no. 5, p. 369–386, doi:10.1007/BF00897191.

Allen, J. R. L., 1970, Studies in fluviatile sedimentation; a comparison of fining-upwards cyclothems, with special reference to coarse-member composition and interpretation: Journal of Sedimentary Research, v. 40, no. 1, p. 298–323, doi:10.1306/74d71f32-2b21-11d7-8648000102c1865d.

Almeida, A. S., and A. G. Journel, 1994, Joint simulation of multiple variables with a Markov-type coregionalization model: Mathematical Geology, v. 26, no. 5, p. 565–588, doi:10.1007/BF02089242.

Armstrong, M., A. Galli, H. Beucher, G. Loc'h, D. Renard, B. Doligez, R. Eschard, and F. Geffroy, 2011, Plurigaussian Simulations in Geosciences: Berlin, Heidelberg, Springer Berlin Heidelberg, 176 p., doi:10.1007/978-3-642-19607-2.

Bellian, J. A., C. Kerans, and D. C. Jennette, 2005, Digital Outcrop Models: Applications of Terrestrial Scanning Lidar Technology in Stratigraphic Modeling: Journal of Sedimentary Research, v. 75, no. 2, p. 166–176, doi:10.2110/jsr.2005.013.

Beucher, H., and D. Renard, 2016, Truncated Gaussian and derived methods: Comptes Rendus Geoscience, v. 348, no. 7, p. 510–519, doi:10.1016/j.crte.2015.10.004.

Boisvert, J. B., M. J. Pyrcz, and C. V. Deutsch, 2007, Multiple-Point Statistics for Training Image Selection: Natural Resources Research, v. 16, no. 4, p. 313–321, doi:10.1007/s11053-008-9058-9.

Boisvert, J. B., M. J. Pyrcz, and C. V. Deutsch, 2010, Multiple point metrics to assess categorical variable models: Natural Resources Research, v. 19, no. 3, p. 165–175, doi:10.1007/s11053-010-9120-2.

Brice, J. C., 1974, Evolution of meander loops: Bulletin of the Geological Society of America, v. 85, no. 4, p. 581–586, doi:10.1130/0016-7606(1974)85<581:EOML>2.0.CO;2.

Burgess, P. M., 2016, Identifying Ordered Strata: Evidence, Methods, and Meaning: Journal of Sedimentary Research, v. 86, no. 3, p. 148–167, doi:10.2110/jsr.2016.10.

Caers, J., and T. Zhang, 2004, Multiple-point geostatistics: A quantative vehicle for integrating geologic analogs into multiple reservoir models: Integration of outcrop and modern analogs in reservoir modeling: AAPG Memoir 80, p. 383–394, doi:10.1897/09-013.1.

Clark, S. K., C. W. Tomlinson, and J. S. Royds, 1944, Well Spacing--Its Effect on Recoveries and Profits: AAPG Bulletin, v. 28, no. 2, p. 231–256, doi:10.1306/3d933648-16b1-11d7-8645000102c1865d.

Colombera, L., N. P. Mountney, and W. D. McCaffrey, 2013, A quantitative approach to fluvial facies models: Methods and example results: Sedimentology, v. 60, no. 6, p. 1526–1558,

doi:10.1111/sed.12050.

Davis, B. M., 1987, Uses and abuses of cross-validation in geostatistics: Mathematical Geology, v. 19, no. 3, p. 241–248, doi:10.1007/BF00897749.

Deschamps, R., N. Guy, C. Preux, and O. Lerat, 2012, Analysis of Heavy Oil Recovery by Thermal EOR in a Meander Belt: From Geological to Reservoir Modeling: Oil & Gas Science and Technology – Revue d'IFP Energies nouvelles, v. 67, no. 6, p. 999–1018, doi:10.2516/ogst/2012015.

Deutsch, C. V., 2006a, A sequential indicator simulation program for categorical variables with point and block data: BlockSIS: Computers and Geosciences, v. 32, no. 10, p. 1669–1681, doi:10.1016/j.cageo.2006.03.005.

Deutsch, C. V., 2006b, What in the reservoir is geostatistics good for? Journal of Canadian Petroleum Technology, v. 45, no. 4, p. 14–20, doi:10.2118/06-04-DAS.

Deutsch, C. V., and A. G. Journel, 1998, GSLIB. Geostatistical Software Library and User's Guide: New York, Oxford University Press, 369 p.

Deveugle, P. E. K., M. D. Jackson, G. J. Hampson, J. Stewart, M. D. Clough, T. Ehighebolo, M. E. Farrell, C. S. Calvert, and J. K. Miller, 2014, A comparative study of reservoir modeling techniques and their impact on predicted performance of fluvial-dominated deltaic reservoirs: AAPG Bulletin, v. 98, no. 4, p. 729–763, doi:10.1306/08281313035.

Doyen, P. M., D. E. Psaila, and S. Strandenes, 1994, Bayesian Sequential Indicator Simulation of Channel Sands From 3-D Seismic Data in The Oseberg Field, Norwegian North Sea, *in* Proceedings of SPE Annual Technical Conference and Exhibition: Society of Petroleum Engineers, p. 197–211, doi:10.2523/28382-MS.

Dubrule, O., 2017, Indicator Variogram Models: Do We Have Much Choice? Mathematical

Geosciences, v. 49, no. 4, p. 441–465, doi:10.1007/s11004-017-9678-x.

Dubrule, O., and E. Damsleth, 2001, Achievements and challenges in petroleum geostatistics: Petroleum Geoscience, v. 7, no. S, p. S1–S7, doi:10.1144/petgeo.7.S.S1.

Durkin, P. R., 2016, The Evolution of Fluvial Meander Belts and Their Product in the Rock Record: Ph.D. Thesis, p. 245, doi:10.11575/PRISM/28141.

Durkin, P. R., S. M. Hubbard, R. L. Boyd, and D. A. Leckie, 2015, Stratigraphic Expression of Intra-Point-Bar Erosion and Rotation: Journal of Sedimentary Research, doi:10.2110/jsr.2015.78.

Eberth, D. A., D. R. Braman, and J. D. Greenough, 2012, A revised stratigraphy and depositional history for the Horseshoe Canyon Formation (Upper Cretaceous), southern Alberta plains: Canadian Journal of Earth Sciences, v. 49, no. 9, p. 1053–1086, doi:10.1139/e2012-035.

Efron, B., 1982, The Jackknife, the Bootstrap and Other Resampling Plans: doi:10.1137/1.9781611970319.

Eisbacher, G. H., M. A. Carrigy, and R. B. Campbell, 1974, Paleodrainage pattern and late-orogenic basins of the Canadian cordillera, *in* W. R. Dickinson, ed., Plate Tectonics and Sedimentation: SEPM, Special Publication 22: p. 143–166.

Emery, X., 2007, Simulation of geological domains using the plurigaussian model: New developments and computer programs: Computers and Geosciences, doi:10.1016/j.cageo.2007.01.006.

Enge, H. D., S. J. Buckley, A. Rotevatn, and J. A. Howell, 2007, From outcrop to reservoir simulation model: Workflow and procedures: Geosphere, v. 3, no. 6, p. 469, doi:10.1130/GES00099.1.

Ethier, V. G., 1975, Application of Markov analysis to the Banff Formation (Mississippian),

Alberta: Journal of the International Association for Mathematical Geology, v. 7, no. 1, p. 47–61, doi:10.1007/BF02080633.

Galli, A., H. Beucher, G. Le Loc'h, B. Doligez, and H. Group, 1994, The Pros and Cons of the Truncated Gaussian Method, *in* Geostatistical Simulations: p. 217–233, doi:10.1007/978-94-015-8267-4_18.

Goovaerts, P., 1994, Comparative performance of indicator algorithms for modeling conditional probability distribution functions: Mathematical Geology, v. 26, no. 3, p. 389–411, doi:10.1007/BF02089230.

Goovaerts, P., 1997, Geostatistics for Natural Resources Evaluation: New York, Oxford University Press, 483 p.

Gringarten, E., and C. V. Deutsch, 2001, Teacher's aide: Variogram interpretation and modeling: Mathematical Geology, v. 33, no. 4, p. 507–534, doi:10.1023/A:1011093014141.

Guardino, F. B., and R. M. Srivastava, 1993, Multivariate geostatistics: beyond bivariate moments, *in* A. Soares, ed., Geostatistics Troia '92 v. 1: p. 133–144.

Hamblin, A. P., 2004, The Horseshoe Canyon Formation in southern Alberta: surface and subsurface stratigraphic architecture, sedimentology, and resource potential: Geological Survey of Canada, Bulletin 578, 180 p.

Hassanpour, M. M., M. J. Pyrcz, and C. V. Deutsch, 2013, Improved geostatistical models of inclined heterolithic strata for McMurray Formation, Alberta, Canada: AAPG Bulletin, v. 97, no. 7, p. 1209–1224, doi:10.1306/01021312054.

Howell, J. A., A. W. Martinius, and T. R. Good, 2014, The application of outcrop analogues in geological modelling: a review, present status and future outlook: Geological Society, London, Special Publications, v. 387, no. 1, p. 1–25, doi:10.1144/SP387.12.

Hua Zhu, and A. G. Journel, 1993, Formatting and integrating soft data: stochastic imaging via the Markov-Bayes algorithm: Geostatistics Troia '92. Vol. 1, p. 1–12, doi:10.1007/978-94-011-1739-5_1.

Isaaks, E. H., and R. M. Srivastava, 1989, An introduction to applied geostatistics: New York, Oxford University Press, 561 p.

Jackson, R. G., 1976, Depositional Model of Point Bars in the Lower Wabash River: SEPM Journal of Sedimentary Research, v. Vol. 46, p. 579–594, doi:10.1306/212F6FF5-2B24-11D7-8648000102C1865D.

Journel, A. G., 1999, Markov Models for Cross-Covariances: Mathematical Geology, v. 31, no. 8, p. 955–964, doi:10.1023/A:1007553013388.

Journel, A. G., and F. Alabert, 1989, Non-Gaussian data expansion in the Earth Sciences: Terra Nova, v. 1, no. 2, p. 123–134, doi:10.1111/j.1365-3121.1989.tb00344.x.

Journel, A. G., and E. H. Isaaks, 1984, Conditional Indicator Simulation: Application to a Saskatchewan uranium deposit: Journal of the International Association for Mathematical Geology, v. 16, no. 7, p. 685–718, doi:10.1007/BF01033030.

Keogh, K. J., A. W. Martinius, and R. Osland, 2007, The development of fluvial stochastic modelling in the Norwegian oil industry: A historical review, subsurface implementation and future directions: Sedimentary Geology, v. 202, no. 1–2, p. 249–268, doi:10.1016/j.sedgeo.2007.05.009.

Klise, K. A., G. S. Weissmann, S. A. McKenna, E. M. Nichols, J. D. Frechette, T. F. Wawrzyniec, and V. C. Tidwell, 2009, Exploring solute transport and streamline connectivity using lidar-based outcrop images and geostatistical representations of heterogeneity: Water Resources Research, v. 45, no. 5, doi:10.1029/2008WR007500.

Krige, D. G., 1951, A statistical approach to some basic mine valuation problems on the Witwatersrand: Journal of the Chemical, Metallurgical and Mining Society of South Africa, v. 52, no. 6, p. 119–139.

Kyriakidis, P. C., C. V. Deutsch, and M. L. Grant, 1999, Calculation of the normal scores variogram used for truncated Gaussian lithofacies simulation: Theory and FORTRAN code: Computers and Geosciences, v. 25, no. 2, p. 161–169, doi:10.1016/S0098-3004(98)00124-1.

Leckie, D. A., and D. G. Smith, 1992, Regional setting, evolution, and depositional cycles of the Western Canada Foreland Basin: Foreland basins and fold belts, p. 9–46, doi:10.1306/m55563c2.

Ma, Y. Z., 2009, Propensity and Probability in Depositional Facies Analysis and Modeling: Mathematical Geosciences, v. 41, no. 7, p. 737–760, doi:10.1007/s11004-009-9239-z.

Martinius, A. W., M. Fustic, D. L. Garner, B. V. J. Jablonski, R. S. Strobl, J. A. MacEachern, and S. E. Dashtgard, 2017, Reservoir characterization and multiscale heterogeneity modeling of inclined heterolithic strata for bitumen-production forecasting, McMurray Formation, Corner, Alberta, Canada: Marine and Petroleum Geology, v. 82, p. 336–361, doi:10.1016/j.marpetgeo.2017.02.003.

Matheron, G., 1963, Principles of geostatistics: Economic Geology, v. 58, no. 8, p. 1246–1266.

Matheron, G., 1973, The intrinsic random functions and their applications: Advances in Applied Probability, v. 5, p. 439–468, doi:10.1017/S0001867800039379.

Matheron, G., H. Beucher, C. de Fouquet, A. Galli, D. Guerillot, and C. Ravenne, 1987, Conditional simulation of the geometry of fluvio-deltaic reservoirs, *in* SPE annual technical conference and exhibition; , Reservoir engineering.: p. 591–599.

Meirovitz, C. D., L. Stright, S. M. Hubbard, and B. W. Romans, 2021, The influence of inter- and intra-channel architecture on deep-water turbidite reservoir performance: Petroleum Geoscience, v. 27, no. 2, p. petgeo2020-005, doi:10.1144/petgeo2020-005.

Miall, A. D., 1973, Markov chain analysis applied to an ancient alluvial plain succession: Sedimentology, v. 20, no. 3, p. 347–364, doi:10.1111/j.1365-3091.1973.tb01615.x.

Miall, A. D., 1988, Reservoir Heterogeneities in Fluvial Sandstones: Lesson From Outcrop Studies.: American Association of Petroleum Geologists Bulletin, v. 72, no. 6, p. 682–697, doi:10.1306/703c8f01-1707-11d7-8645000102c1865d.

Michaelsen, P., and R. A. Henderson, 2000, Facies relationships and cyclicity of high-latitude, Late Permian coal measures, Bowen Basin, Australia: International Journal of Coal Geology, v. 44, no. 1, p. 19–48, doi:10.1016/S0166-5162(99)00048-8.

Mirowski, P. W., D. M. Tetzlaff, R. C. Davies, D. S. McCormick, N. Williams, and C. Signer, 2009, Stationarity scores on training images for multipoint geostatistics: Mathematical Geosciences, v. 41, no. 4, p. 447–474, doi:10.1007/s11004-008-9194-0.

Moysey, S., J. Caers, R. Knight, and R. M. Allen-King, 2003, Stochastic estimation of facies using ground penetrating radar data: Stochastic Environmental Research and Risk Assessment, v. 17, no. 5, p. 306–318, doi:10.1007/s00477-003-0152-6.

Pranter, M. J., A. I. Ellison, R. D. Cole, and P. E. Patterson, 2007, Analysis and modeling of intermediate-scale reservoir heterogeneity based on a fluvial point-bar outcrop analog, Williams Fork Formation, Piceance Basin, Colorado: American Association of Petroleum Geologists Bulletin, v. 91, no. 7, p. 1025–1051, doi:10.1306/02010706102.

Pranter, M. J., and N. K. Sommer, 2011, Static connectivity of fluvial sandstones in a lower coastal-plain setting: An example from the Upper Cretaceous lower Williams Fork

Formation, Piceance Basin, Colorado: AAPG Bulletin, doi:10.1306/12091010008.

Pringle, J. K., A. R. Westerman, J. D. Clark, N. J. Drinkwater, and A. R. Gardiner, 2004, 3D high-resolution digital models of outcrop analogue study sites to constrain reservoir model uncertainty: An example from Alport Castles, Derbyshire, UK: Petroleum Geoscience, v. 10, no. 4, p. 343–352, doi:10.1144/1354-079303-617.

Purkis, S., B. Vlaswinkel, and N. Gracias, 2012, Vertical-to-lateral transitions among cretaceous carbonate facies-A means to 3-D framework construction via Markov analysis: Journal of Sedimentary Research, v. 82, no. 4, p. 232–243, doi:10.2110/jsr.2012.23.

Pyrcz, M. J., J. B. Boisvert, and C. V. Deutsch, 2008, A library of training images for fluvial and deepwater reservoirs and associated code: Computers and Geosciences, v. 34, no. 5, p. 542–560, doi:10.1016/j.cageo.2007.05.015.

Pyrcz, M. J., and C. V. Deutsch, 2014, Geostatistical reservoir modeling: New York, Oxford University Press, 433 p., doi:10.1016/S0098-3004(02)00101-2.

Rahmani, R. A., 1988, Estuarine tidal channel and nearshore sedimentation of a Late Cretaceous epicontinental sea, Drumheller, Alberta, Canada, *in* E. L. de Boer, A. van Gelder, and S. D. Nio, eds., Tide-Influenced Sedimentary Environments and Facies: Dordrecht, D. Reidel, p. 433–471.

Ravenne, C., A. Galli, B. Doligez, H. Beucher, and R. Eschard, 2002, Quantification of facies relationships via proportion curves, *in* Geostatistics Rio 2000: Springer Netherlands, p. 19–39.

Remy, N., A. Shtuka, B. Levy, and J. Caers, 2002, GsTL: The geostatistical template library in C + +: Computers and Geosciences, v. 28, no. 8, p. 971–979, doi:10.1016/S0098-3004(02)00021-3.

Russell, B. H., 1988, Introduction to Seismic Inversion Methods: Society of Exploration Geophysicists, doi:10.1190/1.9781560802303.

Schwarzacher, W., 1969, The use of Markov chains in the study of sedimentary cycles: Journal of the International Association for Mathematical Geology, v. 1, no. 1, p. 17–39, doi:10.1007/BF02047069.

Shepheard, W. W., and L. V. Hills, 1970, Depositional Environments Bearpaw-Horseshoe Canyon (Upper Cretaceous) Transition Zone Dumheler Badlands, Alberta: Bulletin of Canadian Petroleum Geology, v. 18, no. 2, p. 166–215.

Strebelle, S., 2002, Conditional simulation of complex geological structures using multiple-point statistics: Mathematical Geology, v. 34, no. 1, p. 1–21.

Stright, L., 2011, Multiscale Modeling of Deep-Water Channel Deposits: An Interdisciplinary Study Integrating Geostatistics, Geology and Geophysics - The Cretaceous Cerro Toro Formation, Southern Chile, the Eocene Ardath & Scripps Formations, Southern California, and the Ol: 190 p.

Stright, L., A. Bernhardt, A. Boucher, T. Mukerji, and R. Derksen, 2009, Revisiting the use of seismic attributes as soft data for subseismic facies prediction: Proportions versus probabilities: The Leading Edge, v. 28, no. 12, p. 1460–1468, doi:10.1190/1.3272701.

Thomas, R. G., D. G. Smith, J. M. Wood, J. Visser, E. A. Calverly-Range, and E. H. Koster, 1987, Inclined heterolithic stratification: terminology, description, interpretation and significance: Sedimentary Geology, v. 53, p. 123–179.

Tucker, K. E., P. M. Harris, and R. C. Nolen-Hoeksema, 1998, Geologic investigation of cross-well seismic response in a carbonate reservoir, McElroy Field, west Texas: AAPG Bulletin, v. 82, no. 8, p. 1463–1503, doi:10.1306/1d9bcaed-172d-11d7-8645000102c1865d.

Vakarelov, B. K., R. B. Ainsworth, and J. A. MacEachern, 2012, Recognition of wave-dominated, tide-influenced shoreline systems in the rock record: Variations from a microtidal shoreline model: Sedimentary Geology, v. 279, p. 23–41, doi:10.1016/j.sedgeo.2011.03.004.

Widess, M. B., 1973, HOW THIN IS A THIN BED? GEOPHYSICS, v. 38, no. 6, p. 1176–1180, doi:10.1190/1.1440403.

Xu, W., T. T. Tran, R. M. Srivastava, and A. G. Journel, 1992, Integrating Seismic Data in Reservoir Modeling: The Collocated Cokriging Alternative, *in* SPE Annual Technical Conference and Exhibition: doi:10.2118/24742-ms.

Yao, T., 2002, Integrating seismic data for lithofacies modeling: A comparison of sequential indicator simulation algorithms: Mathematical Geology, v. 34, no. 4, p. 387–403, doi:10.1023/A:1015026926992.

Yilmaz, Ö., 2001, Seismic Data Analysis: Society of Exploration Geophysicists, 2027 p., doi:10.1190/1.9781560801580.

Yin, Y., 2013, A New Stochastic Modeling of 3-D Mud Drapes Inside Point Bar Sands in Meandering River Deposits: Natural Resources Research, v. 22, no. 4, p. 311–320, doi:10.1007/s11053-013-9219-3.

Zeng, H., 2009, How thin is a thin bed? An alternative perspective: The Leading Edge, v. 28, no. 10, p. 1192–1197, doi:10.1190/1.3249773.

APPENDIX

Appendix: Code Outline

Two packages of code are described here. The first is for Part 1a (Synthetic 2-Facies Experiment) and the second for Part 1b (Outcrop-Data 3-Facies Experiments). Code is written in Python 2.7.12. Note that SGeMs internal scripting system requires Python 2 code; this was the major driver behind continue with Python 2 instead of transitioning to Python 3. When this project began, Python 2 was still supported, and many third-party libraries were still just transitioning to Python 3. Each package includes scripts, example input files, and Power Point file that describes run procedures and problems in some detail. Various other scripts were written to organize files or generate figures in this thesis, but these were essential to generating results.

Third- Party Libraries

matplotlib	2.2.2
numpy	1.14.2

Folder: Part1a_2Facies_Synthetic

- Folder “targets” – folder containing files to properly run plotter2022.py
- test_uncon.prj – SGeMs project file for soft data reliability tests
- Automated Soft Data Reliability Test Workflow.pptx – Explainer Power Point
- long_ordinary.par – example SGeMs model parameter file
- P0_working.csv – soft data input file for plotter2022.py
- plotter2022.py – chart and statistics script
- rlz_runner.py – SGeMs .py script to automate model generation
- sis.par – example SGeMs model parameter file

Folder: Part1b_3Facies_Outcrop

- 1d_vert_working.prj – SGeMs project file for 1D outcrop stats

- Automated 1D Stats Workflow.pptx – Explainer Power Point

- decimated_grid_0.03_15.gslib – example “mask” input file .gslib

- decimated_grid_0.03_15.npy – example “mask” input file .npy example

- gslib_npy_convert.py – file conversion script

- sgems_decimator.py – SGeMs .py script to automate model generation

- Simple_797_ADE_cosisim.par – example SGeMs model parameter file

- Simple_797_ADE_cosisim_B01_0.03_15.gslib – example output from sgems_decimator.py

- Simple_797_ADE_cosisim_B01_0.03_15.npy – example output converted to .npy

- vt_stats_plotter_2022.py – chart and statistics script

Appendix: Part 1a Positive *B* Results

Simple Kriging (*B*: 0.98)

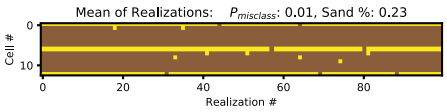

Ordinary Kriging (*B*: 0.98)

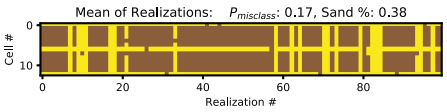

Simple Kriging (*B*: 0.9)

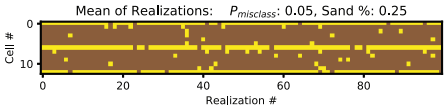

Ordinary Kriging (*B*: 0.9)

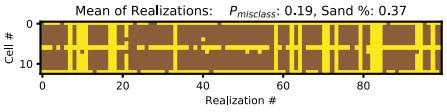

Simple Kriging (*B*: 0.8)

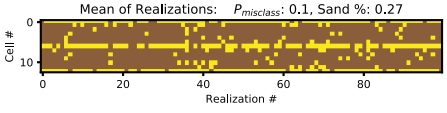

Ordinary Kriging (*B*: 0.8)

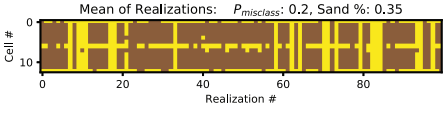

Simple Kriging (*B*: 0.7)

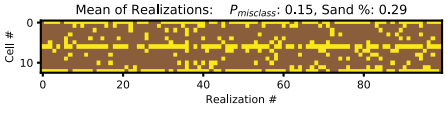

Ordinary Kriging (*B*: 0.7)

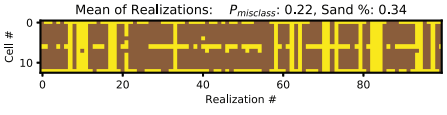

Simple Kriging (*B*: 0.6)

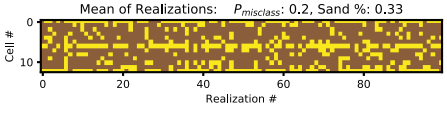

Ordinary Kriging (*B*: 0.6)

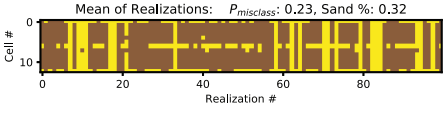

Simple Kriging (*B*: 0.5)

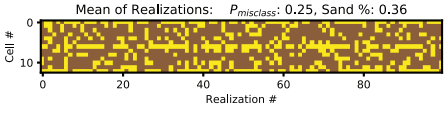

Ordinary Kriging (*B*: 0.5)

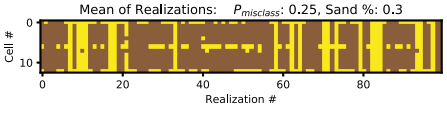

Simple Kriging (*B*: 0.4)

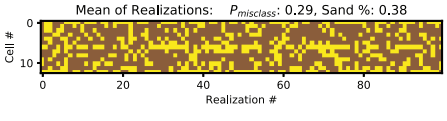

Ordinary Kriging (*B*: 0.4)

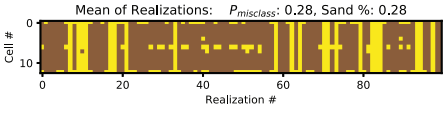

Simple Kriging (*B*: 0.3)

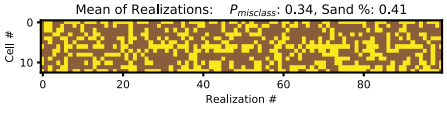

Ordinary Kriging (*B*: 0.3)

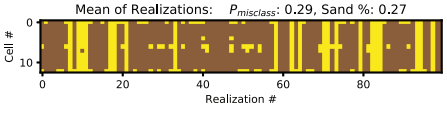

Simple Kriging (*B*: 0.2)

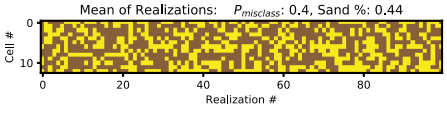

Ordinary Kriging (*B*: 0.2)

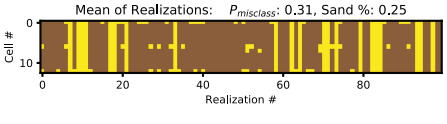

Simple Kriging (*B*: 0.1)

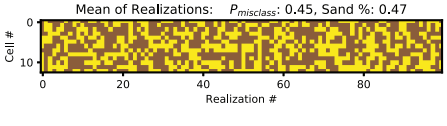

Ordinary Kriging (*B*: 0.1)

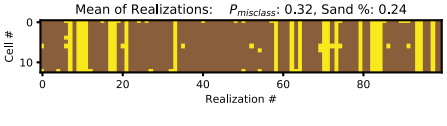

Simple Kriging (*B*: 0.02)

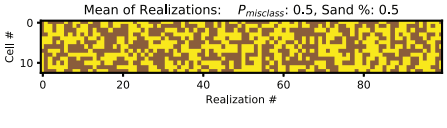

Ordinary Kriging (*B*: 0.02)

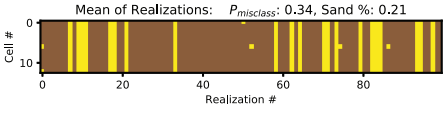

Appendix: Part 1a Negative *B* Results

Simple Kriging (*B*: -0.02)

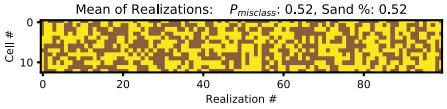

Ordinary Kriging (*B*: -0.02)

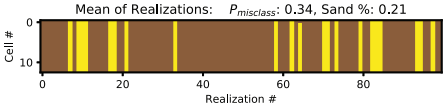

Simple Kriging (*B*: -0.1)

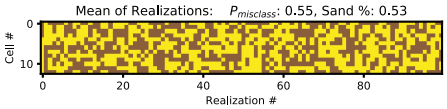

Ordinary Kriging (*B*: -0.1)

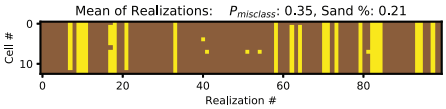

Simple Kriging (*B*: -0.2)

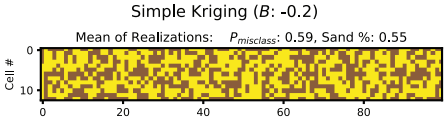

Ordinary Kriging (*B*: -0.2)

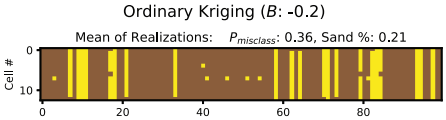

Simple Kriging (*B*: -0.3)

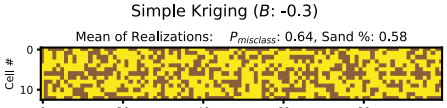

Ordinary Kriging (*B*: -0.3)

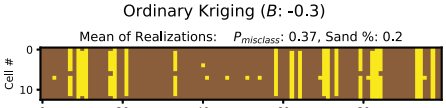

Simple Kriging (*B*: -0.4)

Ordinary Kriging (*B*: -0.4)

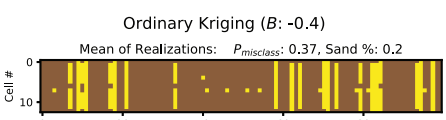

Simple Kriging (*B*: -0.5)

Ordinary Kriging (*B*: -0.5)

Simple Kriging (*B*: -0.6)

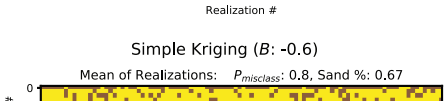

Ordinary Kriging (*B*: -0.6)

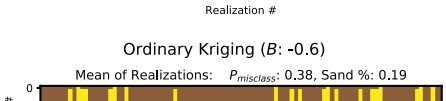

Simple Kriging (*B*: -0.7)

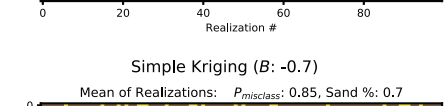

Ordinary Kriging (*B*: -0.7)

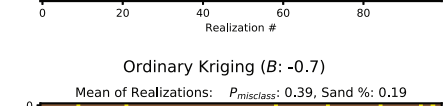

Simple Kriging (*B*: -0.8)

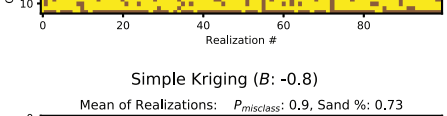

Ordinary Kriging (*B*: -0.8)

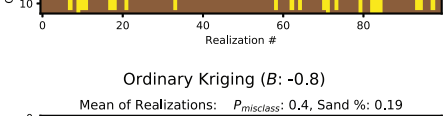

Simple Kriging (*B*: -0.9)

Ordinary Kriging (*B*: -0.9)

Simple Kriging (*B*: -0.98)

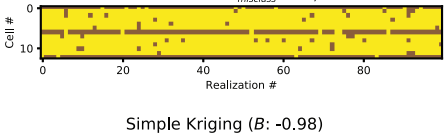

Ordinary Kriging (*B*: -0.98)

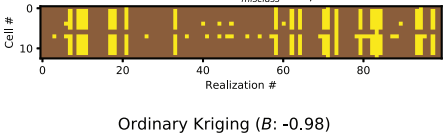

Appendix: Part 1b COSIS Summary Figure Example

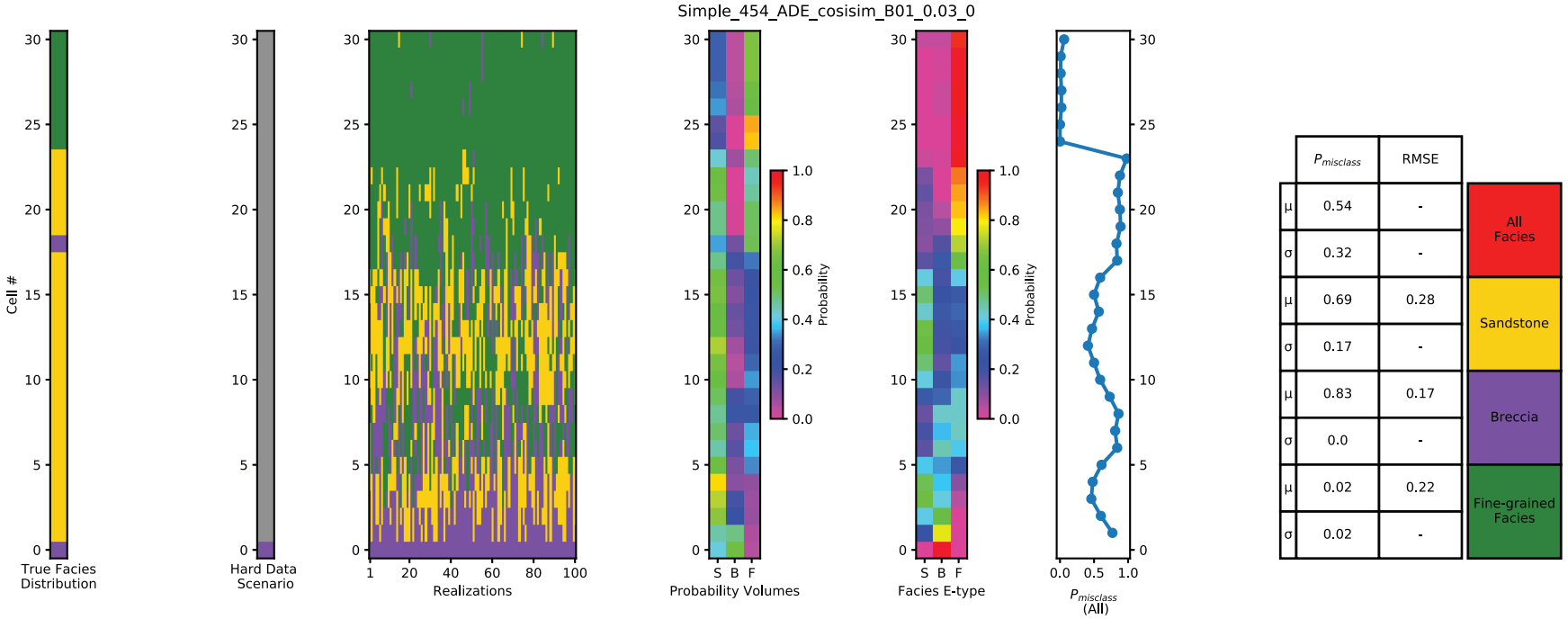

Example of COSIS summary figure: Simple_454_ADE_cosisim_B01_0.03_0.svg. File names carry all relevant attributes in order. "Simple" indicates SK. "454" indicates variogram ranges for sandstone, breccia, and fine-grained facies, respectively. "ADE" indicates all-data search ellipse. "COSIS" indicates agorithm type. "B01" indicates B_i value. "0.03" indicates hard data percentage. The trailing "0" indicates the hard data scenario number.

Appendix: Part 1b SISIM Summary Figure Example

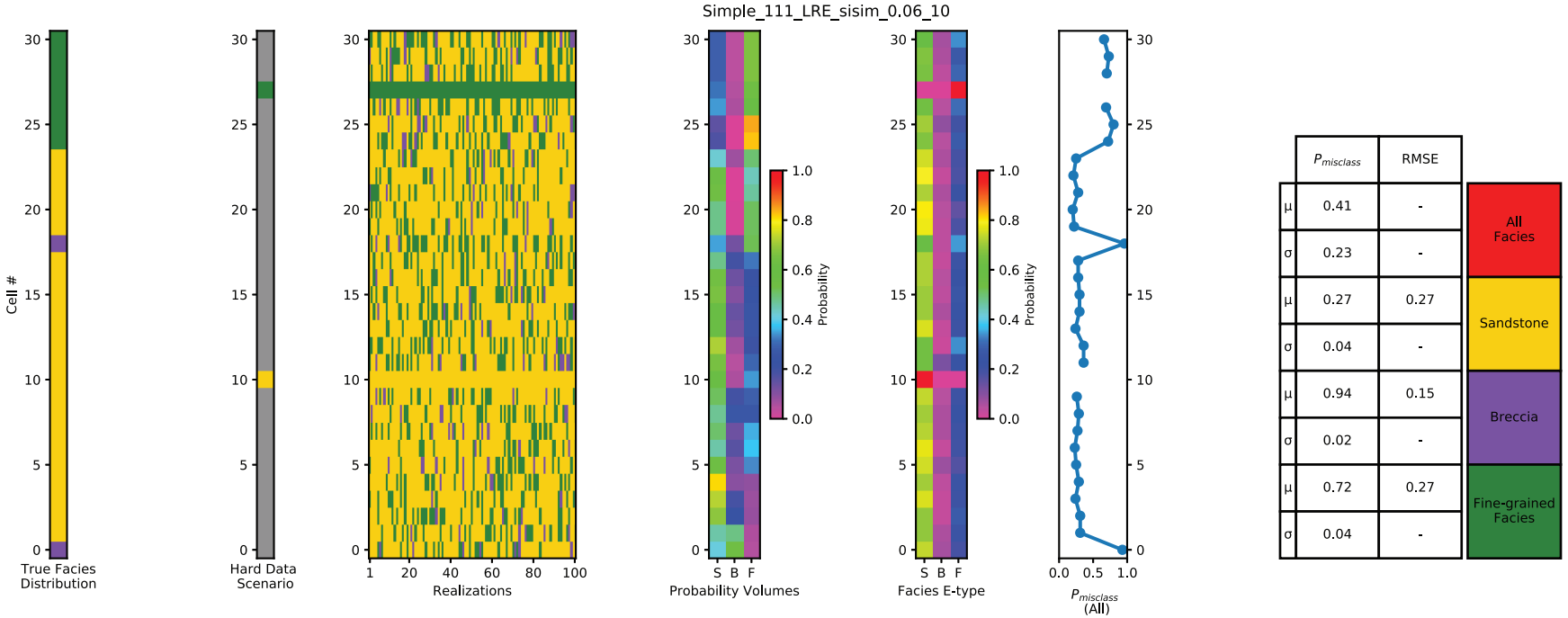

Example of SIS summary figure: Simple_111_LRE_sisim_0.03_0.svg. File names carry all relevant attributes in order. "Simple" indicates SK. "111" indicates variogram ranges for sandstone, breccia, and fine-grained facies, respectively. "LRE" indicates all-data search ellipse. "COSIS" indicates agorithm type. For SIS, B_i value is ommitted. "0.06" indicates hard data percentage. The trailing "10" indicates the hard data scenario number.

Appendix: Part 1b Full Results File Tree

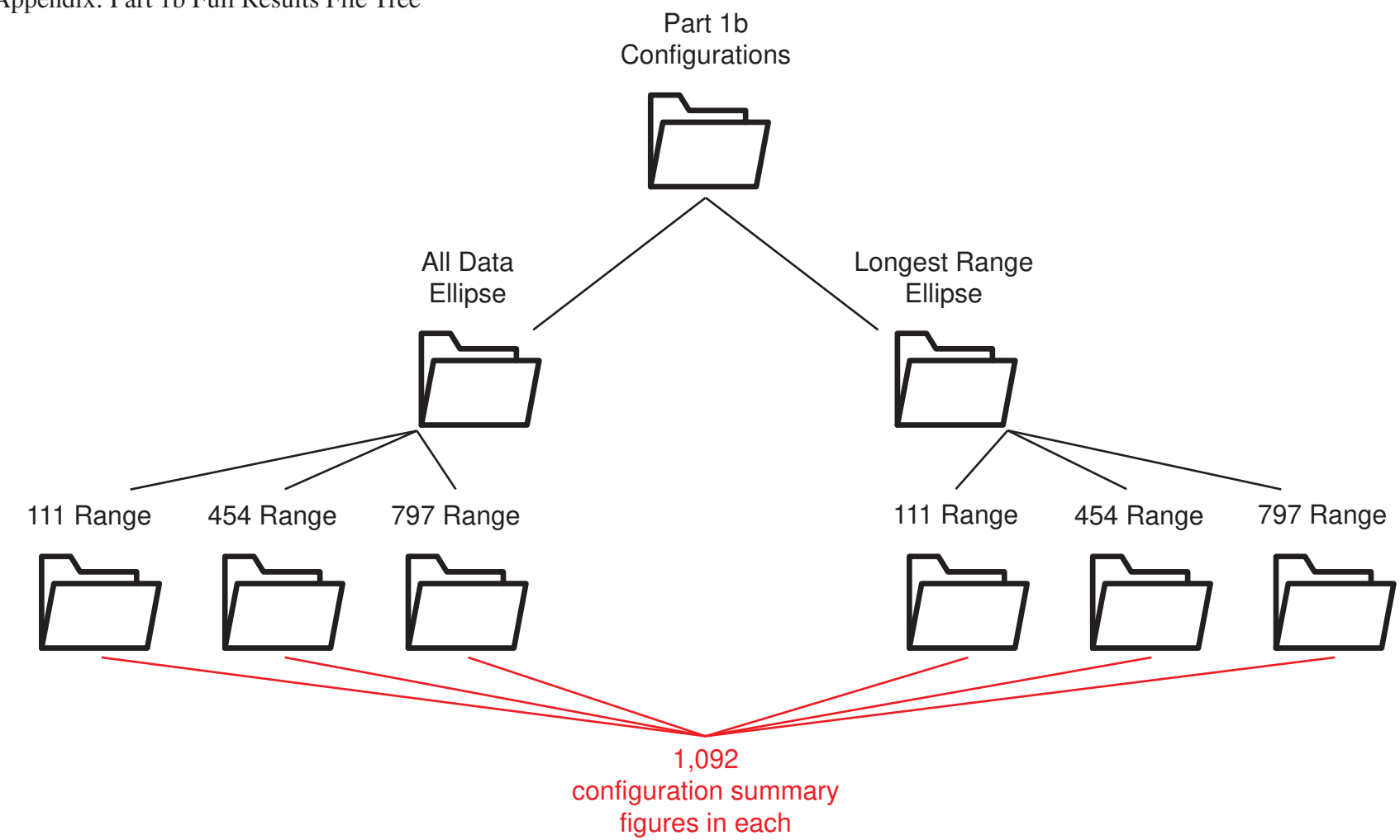

All 6,552 Part 1b Outcrop-Data 3-Facies Experiments are contained in this file structure. As filenames contain all relevant parameter information, the .svg files are not organized beyond the search ellipse and variogram range levels.